INSTITUTE OF PHYSICS PUBLISHING REPORTS ON PROGRESS IN PHYSICS

Rep. Prog. Phys. **67** (2004) 1233–1314 PII: S0034-4885(04)93704-9

# Superionics: crystal structures and conduction processes

**Stephen Hull**

The ISIS Facility, Rutherford Appleton Laboratory, Chilton, Didcot, Oxon, OX11 0QX, UK

Received 16 February 2004
Published 14 June 2004
Online at stacks.iop.org/RoPP/67/1233
doi:10.1088/0034-4885/67/7/R05

## Abstract

Superionic conductors are compounds that exhibit exceptionally high values of ionic conductivity within the solid state. Indeed, their conductivities often reach values of the order of $1\ \Omega^{-1}\ \mathrm{cm}^{-1}$, which are comparable to those observed in the molten state. Following Faraday's first observation of high ionic conductivity within the solids $\beta$-$PbF_2$ and $Ag_2S$ in 1836, a fundamental understanding of the nature of the superionic state has provided one of the major challenges in the field of condensed matter science. However, experimental and theoretical approaches to their study are often made difficult by the extensive dynamic structural disorder which characterizes superionic conduction and the inapplicability of many of the commonly used approximations in solid state physics. Nevertheless, a clearer picture of the nature of the superionic state at the ionic level has emerged within the past few decades. Many different techniques have contributed to these advances, but the most significant insights have been provided by neutron scattering experiments and molecular dynamics simulations. This review will summarize the state of current knowledge concerning the crystal structures and conduction processes of superionic conductors, beginning with a comparison of the behaviour of two of the most widely studied binary compounds, AgI and $\beta$-$PbF_2$. Each can be considered a parent of two larger families of highly conducting compounds which are related by either chemical or structural means. These include perovskite-structured oxides and $Li^+$ containing spinel-structured compounds, which have important commercial applications in fuel cells and lightweight batteries, respectively. In parallel with these discussions, the relative importance of factors such as bonding character and the properties of the mobile and immobile ions (charge, size, polarizability, etc) in promoting the extensive lattice disorder which characterizes superionic behaviour will be assessed and the possibilities for predicting *a priori* which compounds will display high ionic conductivity discussed.

(Some figures in this article are in colour only in the electronic version)

## Contents

Page

1. Introduction 1236
2. Two superionic compounds: AgI and $PbF_2$ 1237
    - 2.1. Silver iodide: AgI 1237
    - 2.2. Factors promoting superionic behaviour 1240
    - 2.3. Lead fluoride: $\beta$-$PbF_2$ 1241
    - 2.4. Type-I and type-II superionic transitions 1244
    - 2.5. High pressure studies 1245
3. $\alpha$-AgI: chemical and structural derivatives 1248
    - 3.1. The family of $Ag^+$ and $Cu^+$ halide superionics 1248
    - 3.2. The preferred cation sites in $\alpha$-CuI 1250
    - 3.3. The role of the immobile sublattice 1252
    - 3.4. Ion–ion correlations: the $Ag^+$ chalcogenides 1253
    - 3.5. Stabilizing the $\alpha$-AgI phase at ambient temperature 1255
    - 3.6. The room temperature superionic: $RbAg_4I_5$ 1257
    - 3.7. The role of dopant cations: $Ag_2MI_4$, $Ag_3MI_5$ and $Ag_4MI_6$ compounds 1258
    - 3.8. The $\alpha$-AgI and perovskite structures: $Ag_3SI$ 1261
    - 3.9. Perovskite-structured superionics: $MPbF_3$ compounds 1262
    - 3.10. Distortions of the cubic perovskite structure: halide perovskites 1265
    - 3.11. Superionicity in the lower mantle: $MgSiO_3$ 1266
    - 3.12. Selection criteria for high conductivity perovskites: $BaCeO_3$ and $LaGaO_3$ 1267
    - 3.13. Anion-deficient perovskites: $Ba_2In_2O_5$ and $MBi_3O_{5.5}$ 1268
    - 3.14. Perovskite intergrowth structures: the Bi*Me*VOx compounds 1269
    - 3.15. *B*-site deficient perovskites: tysonite-structured $LaF_3$ 1271
    - 3.16. *A*-site deficient perovskites: $La_{2/3}TiO_3$, $La_{1/3}NbO_3$ and $WO_3$ 1272
    - 3.17. Double perovskites: cryolite-structured $Na_3AlF_6$ 1274
4. $\beta$-$PbF_2$: chemical and structural derivatives 1275
    - 4.1. The concentration of Frenkel defects 1276
    - 4.2. The role of cation polarizability 1278
    - 4.3. Ternary layered fluorite: $PbSnF_4$ 1278
    - 4.4. Cuboctahedral defects: $(K_{1-x}Bi_x)F_{1+2x}$ and $(Rb_{1-x}Bi_x)F_{1+2x}$ 1280
    - 4.5. Non-stoichiometric fluorites 1281
    - 4.6. Anion-excess fluorite: $(Ca_{1-x}Y_x)F_{2+x}$ 1282
    - 4.7. Anion-deficient fluorite: $(Zr_{1-x}Y_x)O_{2-x/2}$ 1285
    - 4.8. Pyrochlore-structured superionics: $Zr_2M_2O_7$ compounds 1288
    - 4.9. Heavily defective fluorite: $Bi_2O_3$ 1290
    - 4.10. Oxide fluorites: superionicity in $UO_2$ 1291
    - 4.11. The effect of ionic size: anti-fluorite $Li_2O$ 1293
    - 4.12. The ‘paddle-wheel’ and ‘percolation’ mechanisms in $\alpha$-$Li_2SO_4$ 1294
    - 4.13. Spinel-structured superionics: $Li_2MCl_4$ compounds 1295
    - 4.14. Lithium battery applications: $Li_xMn_2O_4$ 1297

4.15. Superionics based on an hcp sublattice: the LISICONs 1298
4.16. The tetragonal-packed sublattice: $Li_4SiO_4$ and $Li_4GeO_4$ 1298
5. Summary and conclusions 1300
Acknowledgments 1301
References 1302

## 1. Introduction

Sodium chloride, NaCl, is a typical example of a 'normal' ionic solid. At ambient temperature, nominally pure NaCl has an ionic conductivity $\sigma_{\mathrm{i}}$ less than $\sim 10^{-8}\,\Omega^{-1}\,\mathrm{cm}^{-1}$, the finite value being primarily due to the presence of extrinsic defects associated with cation impurities (see, e.g. [1]). As illustrated in figure 1, $\sigma_{\mathrm{i}}$ increases with temperature above ~500 K as ionic transport becomes dominated by an increasing concentration of intrinsic, thermally activated Schottky defects, reaching a value of $\sim 10^{-5}\,\Omega^{-1}\,\mathrm{cm}^{-1}$ immediately below the melting point of 1074 K. On melting, $\sigma_{\mathrm{i}}$ increases abruptly by around five orders of magnitude, to a value $\approx 3\,\Omega^{-1}\,\mathrm{cm}^{-1}$ [2].

The first reports of compounds that possess exceptionally high ('liquid-like') values of ionic conductivity within the solid state were given by Faraday in the first half of the 19th century. In the case of the '*fluoride of lead*', the extraordinary nature of this behaviour is clear from the original text [3]:

> 'When a piece of that substance, which had been fused and cooled, was introduced into the circuit of a voltaic battery, it stopped the current. Being heated, it acquired conducting powers before it was visibly red hot in daylight. . ..'

$\beta$-PbF$_2$ is just one example of a collection of highly conducting solids, which subsequently become known as 'superionic' or 'fast-ionic' conductors. As shown in figure 1, there is a continuous and rapid increase in the ionic conductivity of $\beta$-PbF$_2$ with temperature. However, $\sigma_{\mathrm{i}}$ levels off above ~700 K at a value of $\approx 4\,\Omega^{-1}\,\mathrm{cm}^{-1}$ and, remarkably, shows no measurable change on melting at 1158 K [4–6]. The behaviour of another widely studied superionic compound, AgI, is rather different. At 420 K it undergoes an abrupt increase in $\sigma_{\mathrm{i}}$ of over three orders of magnitude associated with a solid → solid phase transition (see figure 1). In the high temperature superionic phase (labelled $\alpha$-AgI) $\sigma_{\mathrm{i}}$ is again very high ($\sigma_{\mathrm{i}} \approx 2\,\Omega^{-1}\,\mathrm{cm}^{-1}$), increases only slowly with temperature and actually decreases by ~10% on melting at 829 K [7].

The next section of this review will provide a more detailed description of both AgI and $\beta$-PbF$_2$, including a comparison of their behaviour, followed by two sections giving a discussion of the properties of many other highly conducting compounds. The primary aim here is to summarize the current state of knowledge concerning the crystal structures of the various superionic compounds and the associated thermally induced lattice disorder that underlies the high macroscopic ionic conductivity. A comprehensive survey of the entire literature relating to superionic conductors would be a mammoth undertaking more appropriate to a dedicated textbook than a review in *Reports on Progress in Physics*. Inevitably, the descriptions will be rather general in nature and restricted to systems in which the ionic migration occurs in three dimensions throughout the bulk of the material[1].

Previous reviews of this subject have categorized the known superionic conductors according to their technological function [23], the nature of the transition to the highly conducting state (abrupt or continuous) [24], their constituent chemical species [25] or crystal structures [26]. The rather haphazard scheme suggested by the Contents list of this review has been devised to highlight the similarities, rather than differences, between the various compounds. This provides a convenient approach when assessing the relative importance of the crystal structure and the properties of the ions themselves (size, charge, polarizability, etc)

---

[1] As a consequence, a number of interesting systems in which the ionic motion is restricted to essentially isolated one-dimensional channels or two-dimensional planes will be ignored. These include hollandite-structured oxides [8, 9] and the $\beta$-aluminas [10, 11], respectively. Similarly, there will be only limited discussion of inhomogeneous materials (such as nanometre-scale planar heterostructures [12, 13]), nano-structured materials [14, 15] or materials in which the crystallinity is low (including polymer electrolytes [16–19]) or absent (such as superionic glasses [20–22]).

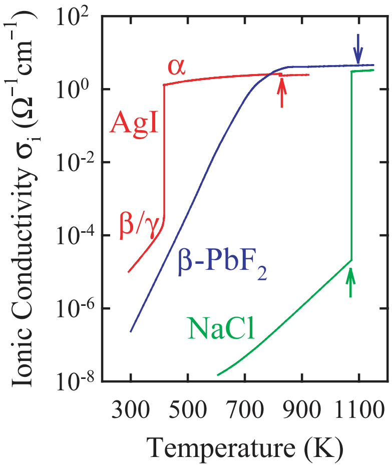

**Figure 1.** The variation of the ionic conductivities of NaCl, $\beta$-PbF$_2$ and AgI with temperature. The vertical arrows denote the melting points of each compound (schematic compilation using data reported in [1, 2], [4–6] and [7], respectively).

in promoting high ionic conductivity and, in the process, provides clues to the wider question of why some compounds (such as AgI and PbF$_2$) display superionic behaviour and others (such as NaCl) do not. Of course, superionic conductors are not merely scientific curiosities and such issues are central to the quest to identify new highly conducting solids for rapidly expanding technological applications within lightweight solid state batteries, high power fuel cells and fast-response gas sensors. These 'applied' aspects of superionic compounds have been the subject of many review articles (for recent examples, see [27–30], [31–34], [35, 36], respectively) and will not, therefore, be discussed in any detail here.

## 2. Two superionic compounds: AgI and PbF$_2$

Textbooks in solid state chemistry and physics invariably include a section describing superionic compounds using one, or both, of the compounds AgI and $\beta$-PbF$_2$ as 'typical' examples. Whilst their impressive high temperature ionic conductivities are well documented, a widely accepted picture of their crystal structures within the superionic state has only emerged within the last ten years or so.

### *2.1. Silver iodide: AgI*

Silver iodide, AgI, usually exists as a mixture of the $\beta$ and $\gamma$ phases under ambient conditions, which possess the hexagonal wurtzite ($P\bar{6}_3mc$ [37]) and cubic zincblende ($F\bar{4}3m$ [38]) crystal structures, respectively. As illustrated in figure 1, AgI undergoes an abrupt superionic transition at 420 K [7]. Within the superionic $\alpha$ phase the ionic conductivity is predominantly due to the motion of Ag$^+$, the electronic component $\sigma_e$ being $\sim 10^7$ times lower [39].

The earliest description of the disordered arrangement of ions within superionic $\alpha$-AgI was provided by powder diffraction studies using x-ray radiation [40]. The I$^-$ were found to adopt a body-centred cubic (bcc) arrangement (space group $Im\bar{3}m$). This anion sublattice contains a number of interstices available as sites for the Ag$^+$, labelled according to the anion co-ordination of a cation placed at their centre. Specifically, there are 6 octahedral (*oct*), 12 tetrahedral (*tet*)

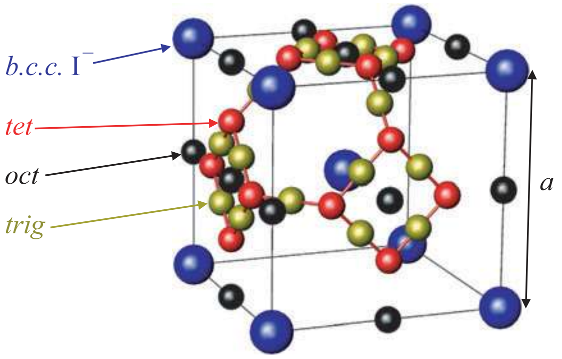

**Figure 2.** The crystal structure of $\alpha$-AgI, showing the bcc anion sublattice and the locations of the octahedral (*oct*), tetrahedral (*tet*) and trigonal (*trig*) interstices. The *tet* sites are predominantly occupied by $Ag^+$ (see section 2.1) and diffusion occurs via the *trig* sites in the $\langle 110 \rangle$ directions shown (after [52]). The cubic lattice parameter $a$ is illustrated. Copyright (1993), with permission from Elsevier.

and 24 trigonal (*trig*) interstices per unit cell[2] (see figure 2) and the two $Ag^+$ per unit cell were proposed to be randomly distributed over all of these 42 positions [40, 41]. This highly disordered picture approximates to a uniform distribution of cations over all the free volume not occupied by anions and, coupled with the high values of ionic conductivity [7], encouraged the use of terms such as 'molten sublattice' and 'liquid-like' to describe $\alpha$-AgI. Such notions were also adopted to discuss the behaviour of other superionic conductors, with the possibility of some form of 'two stage melting' supported by similarities between the entropy changes at the superionic and melting transitions [42]. However, subsequent diffraction studies, using both x-ray and neutron radiations, showed that the cations in $\alpha$-AgI preferentially reside at, or near, the *tet* sites [43–48], though opinion differed over the extent to which the time-averaged distribution extended in the $\langle 100 \rangle$ [44, 46] or $\langle 110 \rangle$ [45, 47] directions (implying $Ag^+$ diffusion via the *oct* and *trig* positions, respectively).

The difficulty in obtaining an unambiguous description of the crystal structure of $\alpha$-AgI using powder diffraction methods is largely a consequence of the limited number of Bragg peaks observed (see figure 3). This, in turn, stems from the high values of the mean squared thermal vibrations of both the anion and cation species [46], which lead to a rapid fall-off in Bragg intensity with increasing scattering vector $Q$. Single crystals of $\beta$-AgI can be grown from solution, but the $\beta \rightarrow \alpha$ transition is of first-order and typically causes them to shatter on heating. However, a single crystal of $\alpha$-AgI of dimensions $\approx 10\,\text{mm}^3$ was prepared by nucleating the $\beta \rightarrow \alpha$ transition at one end of a needle shaped single crystal of $\beta$-AgI (grown such that the hexagonal [001] direction was along its length) and propagating the transition along the needle [49]. In this way 28 reflections could be measured using neutron diffraction and the anharmonic thermal vibrations of the $Ag^+$ about the *tet* sites determined. This indicated a preference for vibration towards the *trig* positions, with the *oct* sites forming local density minima [49].

As illustrated in figure 3, diffraction data collected from $\alpha$-AgI show clear evidence of undulating diffuse scattering between the Bragg peaks, arising from short-range instantaneous correlations between disordered ions. A wider discussion of diffuse scattering and its treatment

---

[2] Formally, within space group $Im\bar{3}m$ the bcc anion sublattice comprises the 2($a$) sites at 0, 0, 0 and $\frac{1}{2}, \frac{1}{2}, \frac{1}{2}$. The *oct* positions are the 6($b$) sites at $0, \frac{1}{2}, \frac{1}{2}$, etc, the *tet* positions are the 12($d$) sites at $\frac{1}{4}, 0, \frac{1}{2}$, etc and the *trig* positions are the 24($h$) sites at $0, y, y$ etc with $y = \frac{3}{8}$.

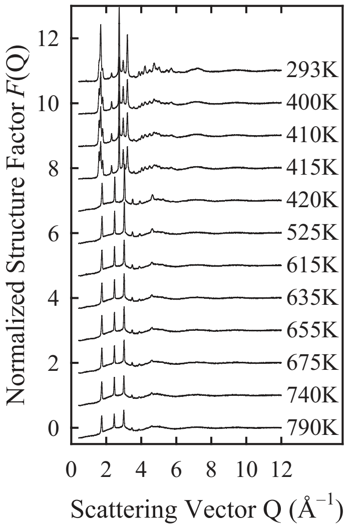

**Figure 3.** The evolution of the measured neutron structure factor, $F(Q)$, of AgI on heating from 293 K (top) to 790 K (bottom). The $\beta \to \alpha$ transition at 420 K and the diffuse scattering within the $\alpha$-AgI phase (observed as undulations in the 'background' scattering) are both clearly visible (after [52]). Copyright (1993), with permission from Elsevier.

is beyond the scope of this review, but its study has provided important insights into the diffusion processes within a number of superionic compounds (for a recent textbook on the subject, see [50]). In the case of $\alpha$-AgI, analysis of the total scattering data shown in figure 3 (i.e. both Bragg and diffuse components) using the so-called Reverse Monte Carlo (RMC) method [51] demonstrated that the Ag$^+$ spend ~75% of their time on the *tet* sites, with hops between these positions in $\langle 110\rangle$ directions outnumbering those along $\langle 100\rangle$ directions by about 6 : 1 [52]. These findings were supported by measurements of the distribution of the diffuse scattering over three-dimensional reciprocal space $Q$ [53, 54], including studies of a large single crystal of $\alpha$-AgI grown from the melt *in situ* on the diffractometer [54].

The structural model of $\alpha$-AgI in which Ag$^+$ diffuse in $\langle 110\rangle$ directions between the tetrahedrally co-ordinated interstices formed by an essentially rigid bcc anion sublattice is supported by many other techniques, including extended x-ray absorption fine structure (EXAFS) measurements [55–57] and molecular dynamics (MD) simulations [58–60] (for an extensive review of the literature devoted to AgI, see [61]). In the latter case, an acceptable agreement with the experimentally observed Bragg intensities and ionic conductivity of $\alpha$-AgI initially required the inclusion of 'harmonic springs' to stabilize the bcc-structured anion sublattice [58]. However, the subsequent development of the so-called Rahman–Vashishta–Parrinello (RVP) empirical interionic potential removed the need for such non-physical artefacts [59]. In this case, the potential between ions *i* and *j* has the general form

$$V_{ij}(r) = \frac{H_{ij}}{r^{n_{ij}}} + \frac{Z_i Z_j e^2}{r} - \frac{1}{2}(\alpha_i Z_j^2 + \alpha_j Z_i^2)\frac{e^2}{r^4} - \frac{W_{ij}}{r^6},$$

where $H_{ij} = A_{ij}(r_i + r_j)^{n_{ij}}$, $n_{ij}$ is typically $\geqslant 7$, $A_{ij}$ is the short-range repulsive strength and $r_{\mathrm{i}}$ and $r_j$ are the ionic radii. $Z_{\mathrm{i}}$ and $Z_j$ are the ionic charges, $\alpha_{\mathrm{i}}$ and $\alpha_j$ the electronic polarizabilities, and $W_{ij}$ the coefficients of the Van der Waals interaction. The values of these coefficients were determined by reference to experimental data, including the phonon dispersion curves, compressibility and lattice energy [59]. The MD simulations of $\alpha$-AgI showed that $Ag^+$ diffusion predominantly occurs by jumps between nearest neighbour *tet* sites, in good agreement with the experimental diffraction studies. However, following a single hop there is a bias towards backward jumps (40%) compared to 20% in each of the other three directions (all would be 25% in an unbiased case) [59].

As will be shown later, the good agreement between the various experimental and simulation techniques concerning the $Ag^+$ diffusion mechanism within $\alpha$-AgI is not necessarily the case in other compounds. Nevertheless, the development of physically meaningful models to describe the interionic interactions allows the possibility to vary the properties of the ions within simulations and assess the role of, for example, the ionic charge or polarizability in the development of superionic behaviour. To facilitate later discussions along these lines, it is instructive at this stage to consider, in very general terms, the factors that might promote high ionic conductivity within a solid phase.

### 2.2. *Factors promoting superionic behaviour*

In the simplest case, the ionic conductivity of a solid can be written as $\sigma_i = nZ\mu$, where $n$ is the concentration of mobile ions, which have charge $Z$ and mobility $\mu$. The superionic phase $\alpha$-AgI has $\sigma_i \sim 1\ \Omega^{-1}\ \mathrm{cm}^{-1}$ and $n \approx \frac{1}{2}$, compared to $\sigma_i \sim 10^{-5}\ \Omega^{-1}\ \mathrm{cm}^{-1}$ and $n \sim 10^{-4}$ for a typical 'normal' ionic conductor such as NaCl at temperatures immediately below the melting point (figure 1). Whilst naive, the relative similarity of the derived values of the ions' mobility in each case implies that the high values of $\sigma_i$ characteristic of the superionic phase are primarily a consequence of the extensive lattice disorder (large $n$), rather than anomalously rapid ionic diffusion (large $\mu$)[3]. However, when faced with the task of designing a new compound with a high ionic conductivity for a specific application, both factors need to be maximized. It is then natural to ask what characteristics are desirable to meet these aims:

- Concentration of mobile ions. Increasing the concentration $n$ of mobile ions within the expression $\sigma_i = nZe\mu$ is clearly advantageous, provided there are a sufficient number of suitable empty sites to accommodate them.
- Structure of the immobile sublattice. The presence of numerous unoccupied interstitial sites within the immobile sublattice (such as the *tet* sites in $\alpha$-AgI) will promote superionic behaviour, but also requires the presence of low energy pathways (conduction channels) between these sites to enhance the mobility $\mu$.
- Ionic polarizability. Highly polarizable ions within the immobile sublattice can deform to allow diffusing ions to 'squeeze' through smaller gaps.
- Bonding character. The preferred co-ordination of a mobile ion (tetrahedral, octahedral, etc) is a manifestation of the bonding character of the material. It has been suggested that mixed bonding character (such as ionic-covalent) is an essential characteristic of good superionics by allowing the mobile ion to be stable in several different co-ordinations during the diffusion process [62–64].
- Ionic charge. Lower charge results in lower Coulomb energies during diffusion [65].
- Ionic radius. During the diffusion process a small mobile ion is better able to diffuse through the gaps in the polyhedral faces formed by the immobile sublattice.

Taking the last item, the small ionic radius of $Ag^+$ ($r_{Ag^+} = 1.00$ Å [66]) might feasibly promote diffusion in $\alpha$-AgI by allowing easy migration through the sublattice formed by the larger anions. However, $Na^+$ is comparable in size ($r_{Na^+} = 0.99$ Å [66]) but NaI does not form a superionic phase at elevated temperatures. Indeed, taken to its logical conclusion, superionics with highly mobile *anions* would not be expected, because anions are normally larger than cations (of the commonly encountered cation species, only $Rb^+$ and $Cs^+$ are significantly larger than the smallest anion, $F^-$ [66]). In reality, and as will be demonstrated later in this review, $F^-$ and $O^{2-}$ conductors easily outnumber $Ag^+$ ones. Clearly, simplistic discussions of this sort neglect the fact that the various factors listed above are, to varying degrees, interrelated, so that no single factor can be used in isolation to explain the presence of high ionic conductivity. Nevertheless, such intuitive notions will prove useful later in this review as convenient tools to explain differences observed in the microscopic and macroscopic behaviour of various individual superionic systems.

---

[3] On these grounds, the alternative description 'fast-ion' conductor is slightly misleading and explains the author's preference for the term 'superionic'.

The discussion above also implies a more general assumption, that the picture of mobile ions diffusing between the interstices formed by a rigid sublattice of counter-ions adopted for $\alpha$-AgI can be used to describe the structural behaviour of all superionic conductors. To assess its validity, the case of $\beta$-$PbF_2$ will be considered next.

### 2.3. *Lead fluoride: $\beta$-$PbF_2$*

As illustrated in figure 1, the ionic conductivity $\sigma_i$ of $\beta$-$PbF_2$ shows a rapid, though continuous, increase on heating, which levels off at a value indistinguishable from that of the liquid state [4–6]. It is now widely accepted that the high value of ionic conductivity observed in superionic $\beta$-$PbF_2$ (and other fluorite-structured compounds [67]) is due almost entirely to anion diffusion, owing to the comparatively large energy required for cation defect formation [68] and the large electronic band gap [69]. The transition to the superionic state is accompanied by a so-called λ-type peak in the specific heat $C_p$, whose maximum is generally taken to define the superionic transition temperature ($T_c = 711$ K in $\beta$-$PbF_2$ [70]). Anomalous behaviour of the elastic constants has also been reported, with a more rapid decrease in the $C_{11}$ component at temperatures above $T_c$ [71, 72]. The earliest descriptions of the ionic distribution within superionic $\beta$-$PbF_2$ proposed a molten anion sublattice (see [73] and references therein). However, whilst there remains some disagreement over the degree of anion disorder (see section 4.1), analysis of the $C_p$ data [70], diffraction studies [74–78] and MD simulations [79–82] all suggest that the anion defect concentration is less than $\sim 10\%$ at temperatures above $T_c$. This is probably a consequence of repulsive interactions between defects [26], which suppress the development of complete sublattice disorder of the type observed in $\alpha$-AgI (section 2.1).

The cubic fluorite crystal structure (space group $Fm\bar{3}m$ [83]) can be described as a face-centred cubic (fcc) array of cations in which all the tetrahedrally co-ordinated interstices are filled with anions and the octahedrally co-ordinated ones are empty[4] (see figure 4). However, to describe the nature of the anion disorder it is often more convenient to illustrate the ionic arrangement as a simple cubic array of anions with cations occupying alternate cube centres (see figure 5). At temperatures well below $T_c$ the principal defect clusters are anion Frenkel pairs, with the interstitial anion in one of the empty anion cube centre positions [84] (which are the *oct* sites in the fcc cation array, see figure 4) and the vacancy is at least more distant than the next nearest neighbour anion site [85]. However, as the defect concentration increases above $\sim 1\%$ the presence of $F^-$ vacancies at closer distances destabilize the interstitials in the cube centre sites [85] and there is a fundamental change in the nature of the defects. Neutron diffraction studies using single crystals of $\beta$-$PbF_2$ showed that the empty cube centre (*oct*) positions are not significantly occupied at $T > \sim T_c$ [76]. Instead, an appreciable

---

[4] Within the centrosymmetric space group $Fm\bar{3}m$ an fcc sublattice is formed by filling the 4(*a*) sites at 0, 0, 0, etc. The *oct* and *tet* positions are in the 4(*b*) sites at $\frac{1}{2}, \frac{1}{2}, \frac{1}{2}$, etc and the 8(*c*) sites at $\frac{1}{4}, \frac{1}{4}, \frac{1}{4}$, etc, respectively. In the non-centrosymmettric case ($F\bar{4}3m$), the former are unchanged but the latter are spilt into two inequivalent sets in 4(*c*) sites at $\frac{1}{4}, \frac{1}{4}, \frac{1}{4}$, etc and 4(*d*) sites at $\frac{3}{4}, \frac{3}{4}, \frac{3}{4}$, etc (see figure 4).

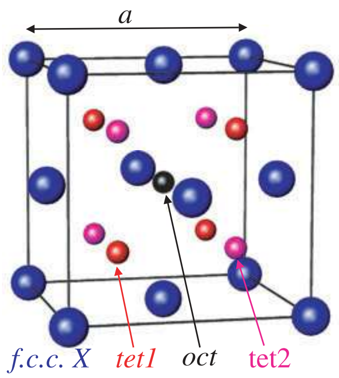

| *A* Sites | Type | Structure |
|---|---|---|
| *oct* | $AX$ | rocksalt |
| *tet*1 or *tet*2 | $AX$ | zincblende |
| *tet*1 and *tet*2 | $AX$ | α-CuI |
| *tet*1 and *tet*2 | $AX_2$ | fluorite |

**Figure 4.** The locations of the octahedral (*oct*) and tetrahedral (*tet*1 and *tet*2) interstices within a generalized fcc-structured sublattice (space group $F\bar{4}3m$). The cubic lattice parameter *a* is illustrated. Various structure types generated by occupying these interstices with counterions in different ways are listed. Copyright (2003) by the American Physical Society.

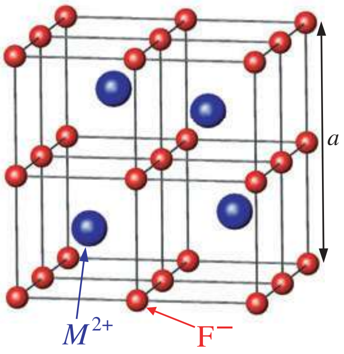

**Figure 5.** The cubic fluorite crystal structure of a compound of stoichiometry $MF_2$, illustrated as a simple cubic array of anions ($F^-$) with cations ($M^{2+}$) occupying alternate cube centres. The cubic lattice parameter *a* is shown.

fraction of the anion lattice sites are vacant and $F^-$ are also located at the sites labelled F1 and F2 in figure 6. The former was considered to be the location of the 'true' Frenkel interstitials, situated between the midpoint of the two nearest neighbour anion sites and the centre of an anion cube in a ⟨110⟩ direction, whilst the latter was attributed to nearest neighbour lattice anions relaxed off their regular sites in ⟨111⟩ directions towards the centres of adjacent empty anion cubes [76]. This leads to the construction of the two defect cluster models labelled 3 : 1 : 2 and 4 : 2 : 2 (where the $v : i : r$ notation is number of vacancies : Frenkel interstitials : relaxed anions) illustrated in figure 7 [76]. The stability of these clusters, and the probable location of the charge compensating anion vacancies, was determined by static energy calculations [86].

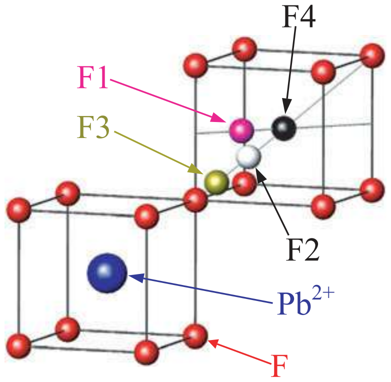

**Figure 6.** The sites proposed to be occupied within the superionic phases of the fluorite-structured compounds (see section 2.3), within anion-excess fluorite-structured compounds (section 4.6) and in the anti-fluorite-structured superionics (section 4.11). In space group $Fm\bar{3}m$ the F1, F2, F3 and F4 positions form the 48($g$) sites at $\frac{1}{2}, y, y$, etc with $y \approx 0.38$, the 32($f$) sites at $x, x, x$, etc with $x \approx 0.4$, the 32($f$) sites at $x, x, x$, etc with $x \approx 0.3$ and the 4($b$) sites at $\frac{1}{2}, \frac{1}{2}, \frac{1}{2}$, etc, respectively.

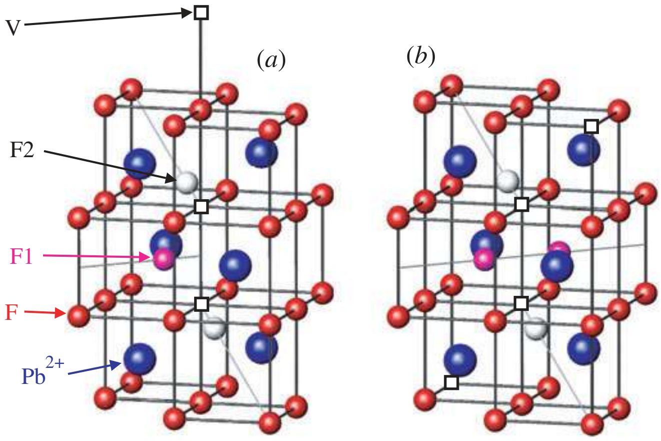

**Figure 7.** The dynamic anion Frenkel defect clusters observed within the superionic phases of the fluorite-structured halides [76, 77]. These are labelled ($a$) 3 : 1 : 2 and ($b$) 4 : 2 : 2, where the $v : i : r$ notation denotes the number of vacancies : Frenkel interstitials : relaxed anions. The probable locations of the charge compensating anion vacancies were determined by static energy calculations [86] (after [76, 77]).

Further support for the presence of such defect clusters within superionic $\beta$-PbF$_2$ was provided by the observation of coherent neutron diffuse scattering within well-defined regions of reciprocal space, indicating that dynamic correlations occur between defective anions [77]. Good agreement with the observed diffuse scattering was obtained by calculating the pattern expected using a 9 : 1 : 8 cluster, which is a 3 : 1 : 2 defect of the type illustrated in figure 7($a$) but with additional (smaller) outward relaxations of the six next nearest neighbour anions in $\langle 111 \rangle$ directions towards empty anion cube centres (corresponding to the F3 sites shown in figure 6). The diffuse neutron scattering was found to be broadened in neutron energy transfer, indicating that the anion Frenkel defects are dynamic and have typical lifetimes of $\sim 10^{-12}$ s [77]. Using the defect model described above, powder neutron diffraction data collected at around 100 temperatures over the range 373–1078 K were analysed to probe the

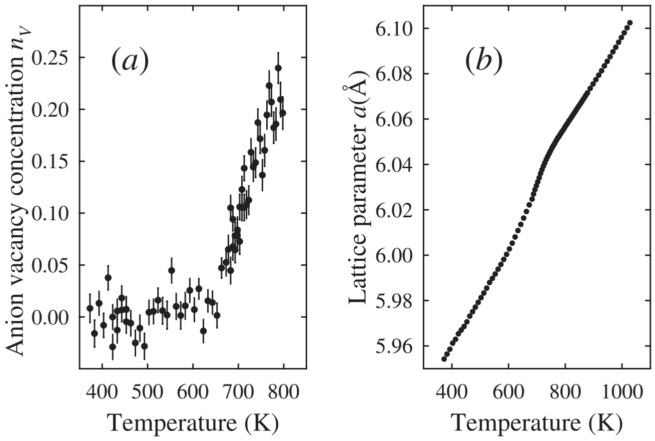

**Figure 8.** The temperature dependence of (*a*) the anion vacancy concentration, $n_V$, and (*b*) the lattice parameter $a$ of $\beta$-PbF$_2$ (after [78]).

**Table 1.** Summary of the superionic properties of the compounds AgI and $\beta$-PbF$_2$.

| Compound | AgI | $\beta$-PbF$_2$ |
|---|---|---|
| Family | Ag$^+$ and Cu$^+$ chalcogenides and halides | Fluorite-structured halides and oxides |
| Other examples | CuI, CuBr, Ag$_2$S, etc | CaF$_2$, SrCl$_2$, UO$_2$, etc |
| Superionic transition | 1st-order structural transition (type-I) | Gradual transition (type-II) |
| Mobile species | Cations | Anions |
| Ambient T structure | Zincblende, wurtzite, etc | Cubic fluorite |
| Superionic structure | bcc/fcc anion sublattice plus 'liquid-like' cations | Fluorite structure plus dynamic anion Frenkel defects |

temperature evolution of the number of anions leaving their regular sites (see figure 8(*a*)) [78]. These data were shown to be consistent with the measured heat capacity anomaly in $\beta$-PbF$_2$ and also demonstrate anomalous behaviour of the lattice parameter $a$ in the vicinity of $T_c$ (figure 8(*b*)) [87].

### 2.4. *Type-I and type-II superionic transitions*

Table 1 summarizes the key features of the superionic properties of $\alpha$-AgI and $\beta$-PbF$_2$ and highlights the significant differences between their respective behaviour. As sections 3 and 4 will show, both are members of wider families which display broadly similar behaviour to their respective archetypes. In particular, first-order transitions to the highly conducting state are a common feature of Ag$^+$ and Cu$^+$ based halides and chalcogenides, whilst a gradual onset of superionic behaviour is characteristic of many halides and oxides that adopt the fluorite crystal structure. The differing nature of the evolution of the highly conducting state with temperature has been used to categorize superionic compounds as type-I (abrupt) or type-II (continuous) [24]. A number of attempts to explain the preferred transition method have recently been made, including theoretical models based on lattice gas methods (see, e.g. [88]) and semi-empirical derivations more specifically devoted to AgI and $\beta$-PbF$_2$ [89, 90].

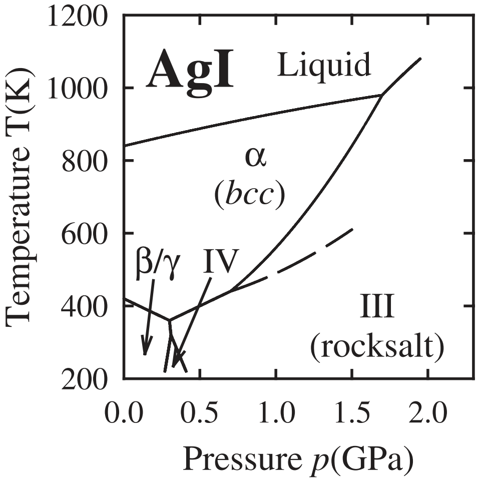

**Figure 9.** The pressure–temperature phase diagram of AgI (after [93]). Under ambient conditions AgI generally exists as a mixture of the wurtzite-structured $\beta$ and zincblende-structured $\gamma$ phases. On increasing temperature the material transforms to the superionic $\alpha$ phase at 420 K, whilst increasing pressure favours transformation to the rocksalt-structured phase III via the tetragonal intermediate phase IV [94]. The dashed line shows the locus of the proposed superionic transition within AgI-IV [97, 98]. Copyright (1996) by the American Physical Society.

A plot of the free enthalpy of a crystal versus its defect concentration $n$ generally shows a minimum at low concentration, due to the counterplay of positive formation enthalpy and configurational entropy gain. However, including an additional term describing the contribution due to defect–defect interactions can lead to a further minimum at higher $n$ [89]. If the second minimum becomes lower than the first, a phase transition occurs from the low defective state to the highly defective (superionic) state. Its nature (type-I or type-II) depends on the balance between various terms in the free enthalpy which are, in turn, functions of the defect–defect interaction, the defect formation enthalpy and the defect configuration (number of interstitials, etc). The former, and in particular its dependence on $n$, has been shown to be particularly important [89]. For the compounds AgI and $\beta$-PbF$_2$, a cube root term, $\sqrt[3]{n}$, yields an excellent agreement with the experimentally determined transition temperatures and ionic conductivity and is consistent with the defect concentrations obtained from MD and Monte Carlo (MC) simulations for both compounds (see [91, 92] and [81], respectively). However, this approach does not, in itself, explain the experimentally observed preference for type-I transitions within the Ag$^+$ and Cu$^+$ based binary halides [24] and type-II transitions within the fluorite-structured halides and oxides. As a consequence, it is instructive to ask whether this distinction holds as a general ‘rule’ for such compounds and, if so, what specific physical properties underlie it. This question is addressed in the next subsection.

### 2.5. *High pressure studies*

The pressure–temperature ($p$–$T$) phase diagram of AgI (figure 9, [93]) shows that the application of hydrostatic pressure at ambient temperature transforms the material from a two phase mixture of the wurtzite-structured $\beta$ and zincblende-structured $\gamma$ phases to a rocksalt-structured form (labelled AgI-III) via an intermediate phase (AgI-IV). The latter has a tetragonal structure [94] and is stable over a sufficiently narrow pressure range that it can be ignored for our purposes. The mechanisms of the pressure-induced wurtzite/zincblende → rocksalt

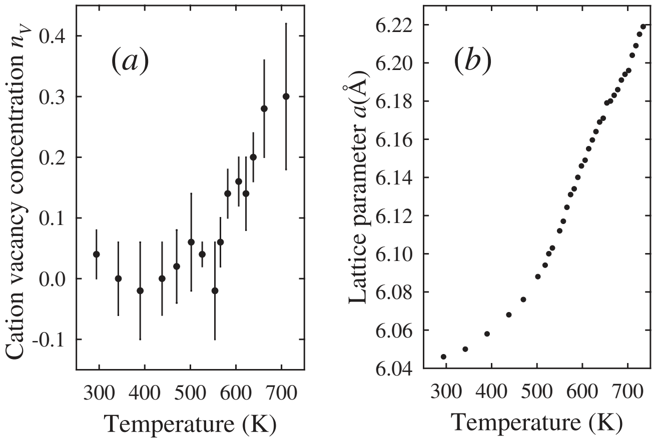

**Figure 10.** The temperature dependence of (*a*) the cation vacancy concentration, $n_V$, and (*b*) the lattice parameter $a$ of rocksalt-structured AgI-III (after [100]). Copyright (1996) by the American Physical Society.

transitions have been extensively studied (see, e.g. [95, 96] and references therein) and involves an increase in the co-ordination of both cations and anions from tetrahedral to octahedral (see figure 4). Ionic conductivity measurements showed a rapid increase in $\sigma_i$ on increasing temperature within the stability field of AgI-III, followed by a small discontinuous increase at the transition to the $\alpha$-AgI phase [97]. This is indicative of a type-II superionic transition within the rocksalt-structured modification. Whilst MD simulations using RVP-type interionic potentials were able to accurately reproduce the locations of many of the phase boundaries within the $p$–$T$ phase diagram, they provided conflicting evidence for [98] and against [99] extensive $Ag^+$ disorder within the AgI-III phase. However, a recent neutron diffraction study on increasing temperature at $p = 1.1$ GPa showed clearly that an increasing fraction of $Ag^+$ leave the *oct* sites characteristic of the rocksalt arrangement and reside on the *tet* sites at $T > \sim 550$ K [100]. The extent of this Frenkel disorder reaches $n_V \sim 0.3$, before the material transforms to $\alpha$-AgI at a temperature of $\approx 700$ K. As illustrated in figure 10, the behaviour of $n_V$ and the lattice parameter $a$ on increasing temperature both mirror that observed in $\beta$-$PbF_2$ at ambient pressure (figure 8 [78]) and confirm that AgI-III undergoes a type-II superionic transition with $T_c \approx 580$ K. Interestingly, the 'cube-root' model for describing the defect–defect interactions discussed at the end of the previous subsection [89] can correctly reproduce the change in the character of the superionic transition within AgI from type-I to type-II under pressure, though a rigorous test of this semi-empirical method is made difficult by the lack of suitable experimental data for the entropy of defect formation at elevated pressure (for a discussion, see [100]).

In common with AgI, $PbF_2$ also generally exists as a mixture of two phases under ambient conditions, these being the cubic fluorite-structured $\beta$ form and the metastable orthorhombic, cotunnite-structured ($\alpha$) phase (space group *Pnma*) [101]. $\alpha$-$PbF_2$ is approximately 10% more dense than the $\beta$ form and the anion sublattice contains two symmetry independent anions (see [102]), such that the $Pb^{2+}$ are surrounded by an irregular co-ordination shell containing nine anions. The $p$–T phase diagram (figure 11, see [102] and references therein) shows that the irreversible $\beta \rightarrow \alpha$ transition occurs at relatively modest pressures ($\approx 0.5$ GPa) at ambient temperature whilst the opposite $\alpha \rightarrow \beta$ transition is also irreversible and can be achieved by heating to temperatures in excess of 600–610 K [103]. High pressure differential

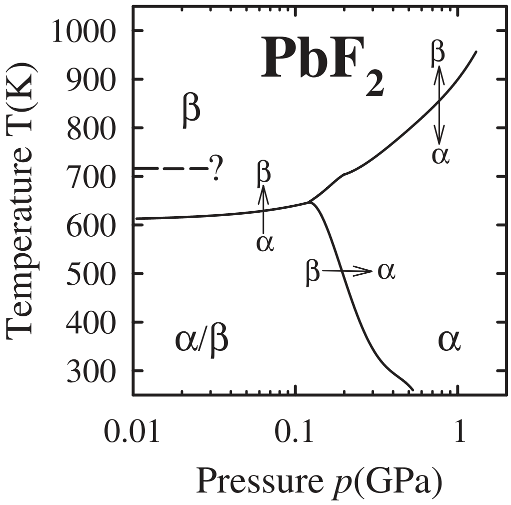

**Figure 11.** The pressure–temperature phase diagram of $PbF_2$ (see [102] and references therein). Under ambient conditions $PbF_2$ exists as a mixture of the fluorite-structured $\beta$ phase and the cotunnite-structured $\alpha$ phase, of which the former is stable at elevated temperatures and the latter favoured at high pressures. The dashed line shows the (possible) locus of the superionic transition within $\beta$-$PbF_2$ on increasing pressure. Copyright (1998) by the American Physical Society.

thermal analysis (DTA) studies showed evidence of a type-II superionic transition within the stability field of $\alpha$-$PbF_2$ [103, 104] (see figure 11), though later investigations using the same technique questioned these observations [105]. Intuitively, extensive lattice disorder would not be expected within the cotunnite-structured $\alpha$ phase because there are no large empty cavities to accommodate interstitial anions. Nevertheless, indirect support for limited anion disorder within $\alpha$-$PbF_2$ was provided by evidence of an anomalous increase in the ionic conductivity of $PbCl_2$ (which adopts the cotunnite structure at ambient pressure) in a narrow temperature range just below its melting point [106] and by observations of rapid hops between the two symmetry independent anion sites in nuclear magnetic resonance (NMR) studies of $\alpha$-$PbF_2$ [107, 108]. The question of superionic behaviour within $\alpha$-$PbF_2$ has recently been resolved by both powder neutron diffraction [102] and MD studies [109]. The former showed that the mean occupancies of both anion sites remain equal to unity (within error) at all temperatures, whilst the latter demonstrated that significant $F^-$ disorder requires the presence of vacancies on the anion sublattice. As a consequence, heating $PbF_2$ at pressures in excess of $\approx$0.5 GPa results in a type-I superionic transition at the $\alpha \rightarrow \beta$ structural transition (see figure 11).

In summary, the application of hydrostatic pressure changes the character of the superionic transition from type-I to type-II in AgI and from type-II to type-I in $PbF_2$. Therefore, the nature of the superionic transition within each family of compounds listed in table 1 is not inherently ‘fixed’ and future structural studies might show evidence of, for example, type-I transitions within other binary halide compounds [67]. In a wider context, the experimental studies described in this subsection are examples of the increasing use of high pressure techniques to probe the structural behaviour of superionics, despite the practical difficulties in performing diffraction studies at elevated pressures and temperatures. Further examples will be given later in this review.

## 3. $\alpha$-AgI: chemical and structural derivatives

This section begins with a discussion of the structural properties of superionic phases within the wider family of binary $Ag^+$ and $Cu^+$ compounds, followed by descriptions of several ternary (chemical) derivatives of AgI. These will be illustrated using the same generalized picture used to describe the structure of $\alpha$-AgI in the previous section, with mobile ions performing jump diffusion between the interstices formed by an immobile sublattice. This approach is inevitably an approximation to the real situation and ignores, for example, the extreme anharmonic thermal vibrations [110, 111] and the increased probability that an ion undergoing a forward hop will subsequently hop backwards [59] or induce local relaxations within the immobile sublattice [112–114]. Nevertheless, this simplistic picture is a convenient method of visualizing the essential features of the conduction processes and is particularly valuable when comparing the conduction mechanisms within a number of compounds which, on purely chemical grounds, appear unrelated.

### *3.1. The family of $Ag^+$ and $Cu^+$ halide superionics*

Silver iodide, AgI, is a member of a family of binary compounds that display high ionic conductivities at elevated temperatures, as summarized in table 2 (and see [111]). This grouping includes its fellow halides AgBr and AgCl, the three copper based counterparts CuI, CuBr and CuCl and the three silver chalcogenides $Ag_2Te$, $Ag_2Se$ and $Ag_2S$. The structural properties of the copper analogues to the latter have also been investigated [115–117], though the ease with which they form non-stoichiometric phases such as $Cu_{2-\delta}S$ has led to a degree of inconsistency between different experimental studies (see, e.g. the phase transition sequence in '$Cu_2Te$' [118–121]) and they will not be considered here.

The two compounds AgCl and AgBr adopt the rocksalt arrangement under ambient conditions (see figure 4) and retain this structure up to their melting points, $T_m$. However, both compounds show anomalous increases in their ionic conductivity in the temperature region ~100–150 K below $T_m$, reaching values of $\sigma_i \approx 0.5\,\Omega^{-1}\,cm^{-1}$ [7]. Ionic conductivity and quasi-elastic neutron scattering studies of AgBr were interpreted in terms of hopping of $Ag^+$ between the lattice *oct* and interstitial *tet* sites [122], whilst powder neutron diffraction studies performed at temperatures up to ≈0.3 K below the melting point of 701 K indicated that the $Ag^+$ vibrate anisotropically about the *oct* sites, with an increasing occupancy of the *tet* positions as $T_m$ is approached [123]. Just below $T_m$ the concentration of these cation Frenkel defects is $n \sim 0.04$ [123]. This implies that AgBr starts to undergo a type-II superionic transition [124], which is interrupted by the melting transition before reaching a highly disordered state of the type observed within $\beta$-$PbF_2$ (section 2.3) and the high pressure rocksalt-structured phase of AgI (section 2.5). This hypothesis is supported by anomalous behaviour of the elastic constants of AgBr at temperatures above ~500 K [125], analogous to that observed during the type-II superionic transition in $\beta$-$PbF_2$ [71, 72]. However, the premature melting of AgBr may be due to the co-incident formation of a small (but significant) concentration of Schottky defects, which induce disorder on the anion sublattice and promote melting [124].

In contrast, the three copper halides CuCl, CuBr and CuI all adopt ambient temperature ($\gamma$) phases with the cubic zincblende structure [83], though powder neutron diffraction studies show strongly anharmonic thermal vibrations of the tetrahedrally co-ordinated $Cu^+$ in $\langle 111 \rangle$ directions towards the *oct* positions [126–128]. However, as shown in table 2, the behaviour of the three $Cu^+$ halides on increasing temperature is very different. CuCl transforms to a wurtzite-structured $\beta$ phase at 681 K before melting at 703 K [129]. The wurtzite structure ($P6_3mc$) comprises a hexagonal close-packed (hcp) anion sublattice in which the cations are ordered

**Table 2.** Summary of the phases observed in the family of $Ag^+$ and $Cu^+$ halides and $Ag^+$ chalcogenides (for references, see sections 2.1, 2.5, 3.1, 3.2, 3.3 and 3.4 and [24, 111, 678]). Phases denoted by $*$ are only stable at elevated pressures. The structures labelled bcc, fcc and hcp indicate the sublattice formed by the immobile anions within superionic phases.

| Compound | Phase | Temperature range | Structure | Space group |
|---|---|---|---|---|
| AgI | $\gamma$ | <420K | Zincblende | $F\bar{4}3m$ |
| | $\beta$ | <420 K | Wurtzite | $P\bar{6}_3mc$ |
| | $\alpha$ | 420–829 K | bcc | $Im\bar{3}m$ |
| | III | $*$ | Rocksalt | $Fm\bar{3}m$ |
| AgBr | | <701 K | Rocksalt | $Fm\bar{3}m$ |
| AgCl | | <728 K | Rocksalt | $Fm\bar{3}m$ |
| CuI | $\gamma$ | <642 K | Zincblende | $F\bar{4}3m$ |
| | $\beta$ | 642–680 K | hcp | $P\bar{3}m1$ |
| | $\alpha$ | 680–878 K | fcc | $Fm\bar{3}m$ |
| | VII | $*$ | bcc | $Im\bar{3}m$ |
| CuBr | $\gamma$ | <664 K | Zincblende | $F\bar{4}3m$ |
| | $\beta$ | 664–744 K | hcp | $P\bar{6}_3mc$ |
| | $\alpha$ | 744–765 K | bcc | $Im\bar{3}m$ |
| CuCl | $\gamma$ | <681 K | Zincblende | $F\bar{4}3m$ |
| | $\beta$ | 681–703 K | Wurtzite | $P\bar{6}_3mc$ |
| | III | $*$ | bcc | $Im\bar{3}m$ |
| $Ag_2Te$ | $\beta$ | <423 K | Monoclinic | $P2_1/c$ |
| | $\alpha$ | 423–1075 K | fcc | $Fm\bar{3}m$ |
| | $\gamma$ | 1075–1223 K | bcc | $Im\bar{3}m$ |
| $Ag_2Se$ | $\beta$ | <406 K | Orthorhombic | $\mathrm{P2_12_12_1}$ |
| | $\alpha$ | 406–1170 K | bcc | $Im\bar{3}m$ |
| $Ag_2S$ | $\gamma$ | <452 K | Monoclinic | $P2_1/c$ |
| | $\beta$ | 452–873 K | bcc | $Im\bar{3}m$ |
| | $\alpha$ | 873–1115 K | fcc | $Fm\bar{3}m$ |

over half the *tet* interstices[5] (see figure 12). The ionic conductivity of $\beta$-CuCl is relatively high ($\sigma_i \sim 0.1\,\Omega^{-1}\,\mathrm{cm}^{-1}$, see [57] and references therein) but the cations predominantly remain on the *tet* sites and it is not a true superionic phase [129]. CuBr undergoes structural phase transitions at 664 and 744 K and shows a dramatic change in the long-range structure of the immobile $Br^-$ sublattice, from fcc($\gamma$) → hcp($\beta$) → bcc($\alpha$) [130]. However, total neutron scattering studies indicated that relatively little change in the local structure of the $Cu^+$ occurs, with essentially tetrahedral co-ordination in all three phases [131]. The cations in $\beta$-CuBr are distributed over the two pairs of *tet* sites which are filled and empty within the fully ordered wurtzite-structured arrangement (*tet*1 + *tet*2 and *tet*3 + *tet*4 in figure 12) in approximately the ratio 3 : 1 [131]. Since $\alpha$-CuBr is also characterized by predominantly tetrahedral co-ordination of the cations within a bcc anion sublattice, it is isostructural with $\alpha$-AgI [130, 131]. The third compound in this series, CuI, will be discussed in more detail in the following subsection.

A glance at the periodic table shows that the $Ag^+$ and $Cu^+$ halides can considered as 'I–VII' compounds, which are end members of the series IV → III–V → II–VI → I–VII. At the

---

[5] The highest symmetry description of an hcp sublattice uses the 2($c$) sites of space group $P6_3/mmc$ at positions $\frac{1}{3}, \frac{2}{3}, \frac{1}{4}$ and $\frac{2}{3}, \frac{1}{3}, \frac{3}{4}$. The *oct* and *tet* interstices within this sublattice are located in the 2($a$) sites at 0, 0, 0 and 0, 0, $\frac{1}{2}$ and the 4($f$) sites at $\frac{1}{3}, \frac{2}{3}, z$, etc with $z = \frac{5}{8}$, respectively. For ideal close packing, the lattice parameters should have $c/a = \sqrt{\frac{8}{3}} = 1.6330$.

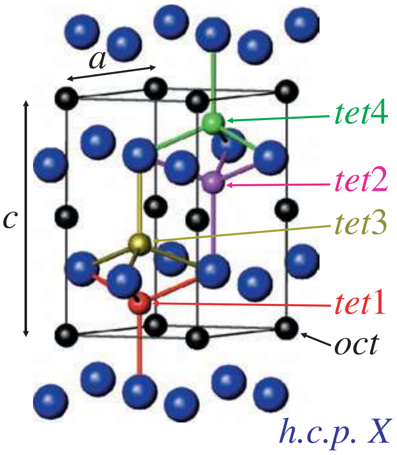

| *A* Sites | Type | Structure |
|---|---|---|
| *oct* | *AX* | *NiAs* |
| *tet*1 and *tet*2 | *AX* | wurtzite |
| *tet*2 and *tet*3 | *AX* | ‘β-CuI’ |

**Figure 12.** The locations of the octahedral (*oct*) and various tetrahedral (*tet*1 to *tet*4) interstices within an hcp-structured sublattice. The most common structure types generated by filling these interstices with counterions in different manners are listed. The lattice parameters *a* and *c* are also shown.

left-hand end, the group IV elemental semiconductors such as Si and Ge are predominantly covalently bonded and the degree of ionicity increases with increasing separation of the two constituent elements within the periodic table. Quantitatively, the $Ag^+$ and $Cu^+$ halides have $f \sim 0.7$–$0.8$ on the Phillips scale of ionicity and span the boundary between a predominantly ionic and predominantly covalent character located at $f_c = 0.785$ [132]. This feature is clearly seen in the crystal structures adopted under ambient conditions (see table 2), which change from the tetrahedral co-ordination characteristic of covalent bonding (zincblende and/or wurtzite structures for AgI, CuCl, CuBr and CuI) to the octahedral environment typically observed in ionic compounds (as in the cases of rocksalt-structured AgCl and AgBr). As a consequence, it has been proposed that the *oct* and *tet* sites are of comparable energy, such that the local bonding character is very sensitive to interionic distance and small fluctuations (comparable to the lattice vibration amplitude) can change the overlap integral and promote extensive ionic motion [62–64]. Whilst the electronic structure is undoubtedly influential in promoting superionic behaviour within the $Ag^+$ and $Cu^+$ halides [133], this argument is not a sufficient condition for superionic behaviour, since a number of poorly conducting compounds also have ionicities close to the ionic–covalent ‘boundary’ (such as $Mg_2S$ and $Mg_2Se$, both with $f \approx 0.78$ [24]). Furthermore, such models imply that ionic conduction occurs between *tet* interstices via the *oct* ones. This is not true in bcc-structured $\alpha$-AgI [52] and, as will be discussed in the next subsection, is not the case in the fcc-based phase $\alpha$-CuI either.

### 3.2. The preferred cation sites in $\alpha$-CuI

CuI transforms from the zincblende-structured $\gamma$ phase to its $\beta$ phase at 642 K, in which the anions form an hcp sublattice [130, 134, 135]. The $Cu^+$ are distributed in the approximate ratio

5 : 1 over two sets of tetrahedral interstices, though the preferentially occupied sites differ from those observed in $\beta$-CuBr, such that the space group is $P\bar{3}m1$ rather than $P\bar{6}_3mc$ (see figure 12) [135]. On further heating, the anion sublattice reverts to an fcc arrangement at the transition to the superionic $\alpha$ phase at 680 K [130, 134, 135].

The distribution of the mobile $Cu^+$ within $\alpha$-CuI has been the subject of some debate within the literature. Early diffraction studies proposed that $\alpha$-CuI possesses the zincblende structure (i.e. isostructural with the ambient temperature $\gamma$-CuI phase, with either the *tet*1 or *tet*2 sites in figure 4 fully occupied) but with large displacements of the $Cu^+$ in $\langle 111\rangle$ directions [134], or the $Cu^+$ are predominantly distributed over all the tetrahedrally co-ordinated sites (*tet*1 and *tet*2 in figure 4), but with $\sim$25% situated on the *oct* positions [136]. The latter model was supported by EXAFS measurements [57], though neutron diffraction studies consistently found no evidence for significant occupancy of the *oct* sites [127, 128, 130]. A series of MD studies using a slightly modified RVP potential supported the neutron studies, with cation diffusion between the supernumerary *tet* positions occurring principally in $\langle 100\rangle$ directions [137–140]. However, other simulations using essentially the same interionic potentials claimed that $\sim$35% of $Cu^+$ were located in the *oct* positions [141]. The apparent disagreement can largely be traced to differences in interpretation of the mean ionic distributions within the simulations [128], with the latter workers dividing the unit cell of $\alpha$-CuI into eight tetrahedra and four octahedra joined via triangular faces formed by the immobile (fcc) anions. Thus, an *oct* site is 'occupied' if the $Cu^+$ lies within the octahedron, and so forth. The discrepancy arises because the $Cu^+$ within the *tet* cavities undergo extensive anharmonic thermal vibrations in the $\langle 111\rangle$ directions and will, on occasion, venture into a neighbouring octahedron. However, the cation does not undergo diffusion in this direction and quickly returns to the tetrahedron. The centres of the octahedra are actually density minima and the *oct* sites should, therefore, be considered locations that are 'avoided' rather than 'occupied' [128].

Clearly, this issue highlights the difficulties in interpreting the results of MD simulations and the limitations of structural models which inherently assume that the ions perform hops between well-defined crystallographic sites (*tet*, *oct*, etc) whilst ignoring the presence of extensive anharmonic thermal vibrations. Indeed, the reliability of such MD simulations of $\alpha$-CuI using RVP-type interionic potentials has recently been questioned [142], since the derived partial pair distribution functions $g_{\mathrm{CuI}}(r)$ and $g_{\mathrm{CuCu}}(r)$ are very different from those measured by neutron diffraction [128] and EXAFS methods [142] (though there is no perfect agreement between these two experimental techniques either). In particular, the MD method does not reproduce the observed $Cu^+$–$Cu^+$ contacts of $\approx$2.5 Å observed experimentally within $\alpha$-CuI, which probably correspond to simultaneous occupancy of nearest neighbour *tet* sites in $\langle 100\rangle$ directions [142]. Similar problems have been encountered in reconciling the simulated and experimental values for the $Cu^+$ diffusion coefficient [137, 138], probably due to the neglect of three-body effects which are a consequence of the high polarizability of $I^-$ [140].

Whilst a detailed description of the short-range correlations between the cations within $\alpha$-CuI remains the subject of some debate, the time-averaged structure can, to a good approximation, be described by a random distribution of $Cu^+$ over all the *tet* cavities within an fcc anion sublattice [127, 130]. Recalling that the ambient temperature zincblende-structured $\gamma$ phase has the $Cu^+$ ordered over half the *tet* interstices in an fcc array, the $\gamma \rightarrow \alpha$ transition can be interpreted as a gradual (type-II) superionic transition interrupted by the presence of the two first-order $\gamma \rightarrow \beta$ and $\beta \rightarrow \alpha$ structural transitions. Support for this notion was provided by x-ray diffraction studies of CuI on increasing temperature, which showed that extrapolation of the temperature dependence of the intensities of the Bragg peaks observed in the $\gamma$ phase across the 'gap' in which the $\beta$ phase is stable meet those measured in the $\alpha$ phase [134]. In addition, there is evidence of the onset of $Cu^+$ disorder within $\gamma$-CuI at the upper region

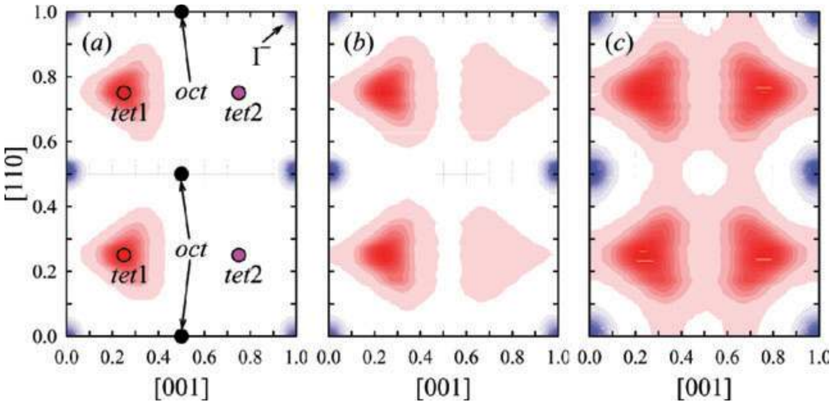

**Figure 13.** The mean ionic density of $I^-$ and $Cu^+$ within the $(1\bar{1}0)$ plane of CuI at temperatures of (*a*) 600 K, (*b*) 660 K and (*c*) 670 K, simulated by MD methods. The $I^-$ densities are centred at $0, 0, 0, \frac{1}{2}, \frac{1}{2}, 0$, etc and form an fcc-structured sublattice. All other contours correspond to $Cu^+$ density. The ionic distributions are calculated within a slice of thickness 0.1 perpendicular to the plane. The locations of the octahedrally (*oct*) and tetrahedrally (*tet*1 and *tet*2) co-ordinated sites are illustrated in (*a*). The type-I superionic transition, corresponding to dynamic disorder of the $Cu^+$ over all the *tet* sites, occurs at ≈665 K (after [149]). Copyright (2003) by the American Physical Society.

of its temperature regime provided by ionic conductivity [143], NMR [144], Raman [145], MD [137] and neutron diffraction [127, 128] data. The latter two techniques indicate that ∼5% of $Cu^+$ leave the zincblende lattice sites and reside on the alternative set of *tet* cavities at temperatures immediately below the $\gamma \rightarrow \beta$ transition. Conversely, calorimetry measurements [134] and earlier MD simulations [146] both showed that $\gamma$-CuI and $\alpha$-CuI have substantially different lattice energies, suggestive of a type-I superionic transition. To resolve this issue, the possibility that the $\beta$ phase might be eliminated under pressure was proposed [147]. However, subsequent diffraction measurements indicated that at $p > \approx 0.3$ GPa the $\gamma \rightarrow \alpha$ transition does not become second order but, instead, occurs via a different intermediate phase with rhombohedral symmetry [148]. Instead, this issue has recently been resolved by the addition of small quantities of $Cs^+$ to CuI, which destabilizes the $\beta$ phase. The resultant doped material was shown to undergo a type-I $\gamma \rightarrow \alpha$ transition at 643(2) K [149]. MD simulations of pure CuI on increasing temperature, with the tendency to form the hexagonal phase removed by constraining the shape of the simulation box to remain cubic, also showed an abrupt transition from a slightly disordered $\gamma$ phase to the fully disordered (superionic) $\alpha$ phase at ≈665 K (see figure 13) [149].

### *3.3. The role of the immobile sublattice*

It is difficult to systematically assess the influence of the structure of the immobile sublattice on the superionic behaviour within the $Ag^+$ and $Cu^+$ halides because the number of phases observed is rather small (see table 2). However, as illustrated by the case of AgI in section 2.5, many superionic compounds undergo structural phase transitions at relatively low pressures[6]. If the high pressure phases display superionic behaviour then their study can give important insights, by allowing the nature of lattice disorder to be studied within *different* phases of the *same* compound (and, by extension, within *different* compounds with the *same* structure).

---

[6] This may not be merely coincidental, since the presence of phase transitions within many superionic compounds at low pressures has been attributed to the ‘structural instabilities’ that are a consequence of the borderline covalent-ionic nature of the bonding discussed at the end of section 3.1 [150].

Intuitively, the application of hydrostatic pressure would not be expected to promote superionic behaviour, because compression favours structural phase transitions to more densely packed arrangements of the immobile ions, leaving a smaller 'free volume' available for the mobile ones. However, this intuitive notion is contradicted by the presence of a type-II superionic transition in AgI-III (section 2.5), despite it having a density almost 20% higher than the ambient pressure form [94]. CuCl provides an even more dramatic example, since it does not possess a true superionic phase at ambient pressure [129] (see section 3.1), but does have a high pressure superionic bcc-structured phase (CuCl-III) at $p > \approx 0.2$ GPa and $T > \approx 700$ K [151, 152]. CuI has also been shown to adopt a bcc-structured superionic phase (CuI-VII) at $p > \approx 1.2$ GPa and $T > \approx 920$ K, in addition to its (ambient pressure) fcc-structured $\alpha$ phase [148, 151]. In principle, the four bcc-structured superionic phases $\alpha$-AgI, $\alpha$-CuBr, CuCl-III and CuI-VII allow the preferred cation locations to be studied for different sizes of cations and anions. Neutron diffraction studies [46, 52, 130, 131], including those performed at elevated $p$ and $T$ [148, 152], indicate that such steric factors have little influence on the ionic conduction process, since all four phases are characterized by predominantly tetrahedral cation site occupancy. This preference is also a feature of the fcc (AgI-III [100] and $\alpha$-CuI [127, 135]) and hcp ($\beta$-CuBr [131] and $\beta$-CuI [127, 135]) based phases.

A consequence of the cations' favoured occupancy of the tetrahedrally co-ordinated cavities within the $Ag^+$ and $Cu^+$ halide superionics is that bcc-based phases should possess higher ionic conductivities than fcc and hcp-based ones, because there are six *tet* sites available for each mobile ion rather than two (compare figures 2, 4 and 12). Furthermore, the different stacking sequences of close-packed layers which construct the fcc and hcp lattices result in edge- and corner-sharing of anion tetrahedra in the former but face-, edge- and corner-sharing in the latter. The pairs of face-sharing tetrahedra parallel to $[001]_{\mathrm{hex}}$ in the hcp case produce short cation–cation contacts (of separation $c/2$, where $c$ is the hexagonal lattice parameter, see figure 12) and, in practice, these pairs of sites cannot be simultaneously occupied. Thus, the number of available tetrahedrally co-ordinated holes for each mobile ion within an hcp sublattice is only 1. This probably accounts for the presence of only partial disorder observed within those phases which possess an hcp immobile sublattice ($\beta$-CuBr [131] and $\beta$-CuI [127, 135]). These simple geometric considerations imply that the ionic conductivity of superionic phases will decrease in the sequence bcc → fcc → hcp. This prediction is broadly in accord with experimental data for the $Ag^+$ and $Cu^+$ halides [24] and also holds for the $Ag^+$ chalcogenides (next subsection) and several ternary derivatives of AgI (section 3.7).

### 3.4. *Ion–ion correlations: the $Ag^+$ chalcogenides*

The three silver chalcogenides $Ag_2S$, $Ag_2Se$ and $Ag_2Te$ all adopt low symmetry ordered phases under ambient conditions (space groups $P2_1/c$ [153], $P2_12_12_1$ [154] and $P2_1/c$ [155], respectively) and form at least one high temperature phase characterized by extensive dynamic $Ag^+$ disorder within an immobile anion sublattice (see table 2). Numerous diffraction [116, 156–161] and MD [161–169] studies of these superionic phases have been reported, principally to compare their structural properties with the $Ag^+$ halides and assess the effects of the doubled density of mobile cations.

The most recent neutron diffraction studies of the two fcc-structured phases $\alpha$-$Ag_2S$ [161] and $\alpha$-$Ag_2Te$ [160] showed their time-averaged structures to be very similar, with the majority of the cations located in the *tet* interstices but with a significant fraction (up to around half) located close to the *oct* positions. Following the discussion given in the previous subsection,

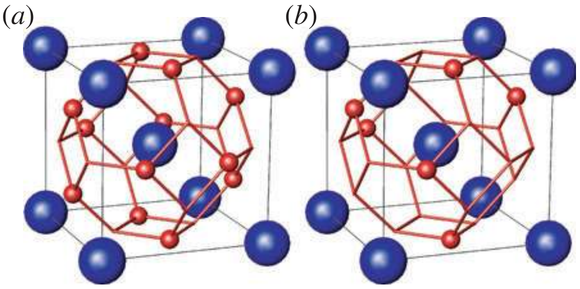

**Figure 14.** Hypothetical crystal structures obtained by filling the *tet* interstices within a bcc sublattice avoiding simultaneous occupancy of (*a*) next nearest neighbour sites and (*b*) next next nearest neighbour sites. Both would be expected to be poor conductors, because a mobile ion cannot move to a neighbouring empty *tet* site without adopting unfavourably short nn or nnn. contacts. The ratios of the number of mobile to immobile ions are (*a*) 3 : 1 and (*b*) 1.5 : 1, respectively.

exclusive occupancy of the *tet* positions means that the number of available sites is equal to the number of mobile $Ag^+$. This generates a fully ordered 'anti-fluorite' structure (figure 4), with the cations filling all the *tet* cavities within an fcc anion array. Thus, the observed high ionic conductivity within the fcc-structured phases is inconsistent with sole occupancy of the *tet* sites and requires the additional partial occupancy of the *oct* positions. There is apparently no such restriction within the three bcc-structured phases $\beta$-$Ag_2S$, $\alpha$-$Ag_2Se$ and $\gamma$-$Ag_2Te$, because there are twelve *tet* sites per unit cell available for four cations. Diffraction studies confirm that the $Ag^+$ are predominantly distributed over the *tet* interstices (see [156, 161], [116] and [159, 160], respectively) with only evidence of limited occupancy of the *oct* positions in $\beta$-$Ag_2S$ at the lower end of its temperature range [157].

Despite the availability of numerous empty sites, geometric effects due to the finite size of the ions can still impose restrictions on the instantaneous distribution of $Ag^+$ within a bcc-structured sublattice. Each *tet* site has four nearest neighbour (nn) *tet* sites at a distance $\sqrt{2}a/4$, two next nearest neighbour (nnn) sites at a distance $a/2$ and a further eight sites at a distance $\sqrt{6}a/4$. The cubic lattice parameters of $\alpha$-AgI ($a = 5.05(1)$ Å at 420 K [46]) and $\alpha$-$Ag_2S$ ($a = 4.882(1)$ Å at 558 K [161]) and the ionic radius of the monovalent silver ion ($r^{\mathrm{IV}}_{\mathrm{Ag}^+} = 1.00$ Å [66]) indicate that no nn *tet* sites can be simultaneously filled because their separation is only ≈1.7 Å. This halves the number of available *tet* sites per unit cell to six (see figure 14(*a*)), which corresponds to three available sites per immobile ion ($I^-$ or $S^{2-}$). This still exceeds the cation content given by the stoichiometry, so there is no requirement for the occupancy of the *oct* sites in order to achieve high macroscopic conductivity within the bcc-structured phases of the $Ag^+$ chalcogenides. Clearly, if the mobile ions were larger, such that simultaneous occupancy of the nnn sites were not possible, this figure would be halved again (see figure 14(*b*)).

Whilst such steric limitations alone are insufficient to promote long-range ordering over the *tet* sites within the $Ag^+$ chalcogenides, Coulomb repulsions between the cations do cause short-lived, short-range correlations between the motion of individual mobile ions. This has been demonstrated by the low values of the Haven's ratio in $\alpha$-$Ag_2S$, this being defined as $H_{\mathrm{r}} = D_{\mathrm{t}}/D_{\sigma}$, where $D_{\mathrm{t}}$ and $D_{\sigma}$ are the diffusion coefficients measured by tracer diffusion and ionic conductivity methods, respectively. For uncorrelated motion $H_{\mathrm{r}}$ is equal to unity, but experimental values of $H_{\mathrm{r}} \approx 0.5$ have been reported (see [170] and references therein). A more direct confirmation was provided by the observation of anisotropic diffuse x-ray [157] and neutron [158] scattering from $\beta$-$Ag_2S$. To interpret these data, a structural model of local cation ordering over the *tet* sites was proposed [157]. Considering the *tet* sites within

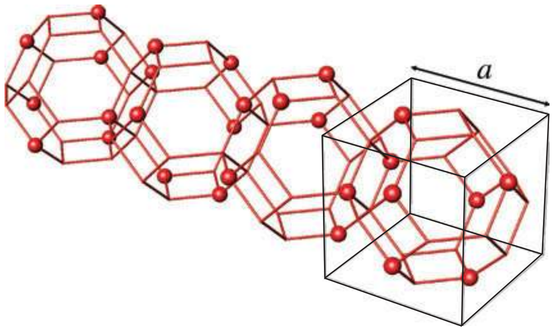

**Figure 15.** Structural model for a microdomain of ordered $Ag^+$ arranged over the *tet* sites within four unit cells of bcc-structured $\beta$-$Ag_2S$ (after [157]). Copyright (1980) by the American Physical Society.

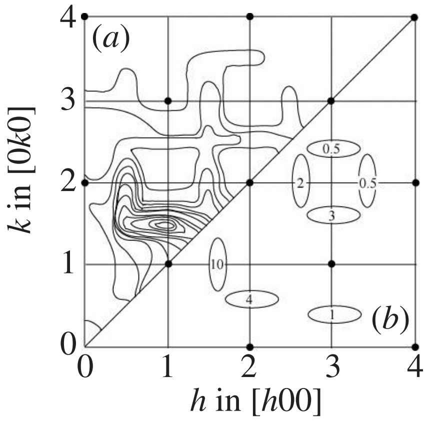

**Figure 16.** Comparison of (*a*) the calculated diffuse scattering using the microdomain model illustrated in figure 15 with (*b*) a schematic representation of the observed diffuse x-ray scattering from $\beta$-$Ag_2S$ in the (001) plane of reciprocal space (after [157]). Copyright (1980) by the American Physical Society.

the unit cell to form a cuboctahedron allows the construction of an idealized microdomain of ordered $Ag^+$ sites (figure 15) consisting of four connected cuboctahedra. The calculated diffuse scattering based on this model is in good agreement with that measured experimentally (see figure 16 [157]).

The presence of short-range correlations between the motions of the diffusing cations does not have a significant detrimental effect on the magnitude of the ionic conductivities of the three silver chalcogenides $Ag_2S$, $Ag_2Se$ and $Ag_2Te$ (see figure 17, [171]), which exceed that of $\alpha$-AgI [7] by a factor of $\sim$3. $Ag_2S$ and $Ag_2Te$ possess both fcc- and bcc-structured superionic phases and the higher ionic conductivities of the latter in both compounds is consistent with the discussion of the relative number of available interstices given in the previous subsection, despite their order on increasing temperature being reversed.

### *3.5. Stabilizing the $\alpha$-AgI phase at ambient temperature*

Despite having a lower cation density than the bcc-structured phases of the $Ag^+$ chalcogenides, a number of reports of correlations between the motions of the cations within $\alpha$-AgI at the

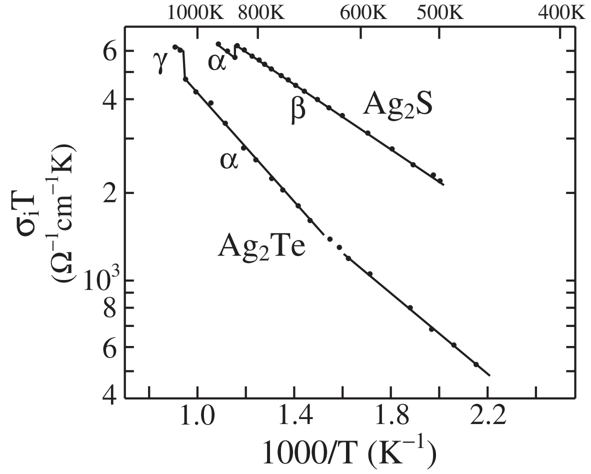

**Figure 17.** The temperature variation of the ionic conductivity, shown as $\sigma_i T$ versus $1000/T$, of $Ag_2S$ and $Ag_2Te$. The ionic conductivity within the bcc-structured phases $\beta$-$Ag_2S$ and $\gamma$-$Ag_2Te$ is higher than within the fcc-structured phases $\alpha$-$Ag_2S$ and $\alpha$-$Ag_2Te$ (after [171]). Copyright (1981), with permission from the Physical Society of Japan.

lower temperature end of its stability range have appeared in the literature. These include evidence for an 'order–disorder' transition within $\alpha$-AgI at ≈670 K (for a discussion, see [61]) and claims of a 'memory effect'. In the latter, a two-phase $\beta + \gamma$ mixture was heated above the transition to the $\alpha$ phase at 420 K, but kept below ≈450 K, and a mixture with the original $\beta + \gamma$ phase composition was retrieved on cooling [172]. Both experimentally observed anomalies remain controversial [61].

From an applications point of view, the complete long-range cation ordering process which occurs when $\alpha$-AgI transforms to $\beta/\gamma$-AgI on cooling is a more important issue, since an understanding of this transition mechanism is key to attempts to stabilize the high conductivity bcc-structured phase at ambient temperature. The possible ordering schemes for the $2 \times Ag^+$ per unit cell over the 12 *tet* positions within $\alpha$-AgI have been considered [173, 174], by dividing the available sites into six interpenetrating equivalent bcc sublattices (see figure 18). At high temperatures all the sublattices are (on average) equally occupied, whilst at low temperature repulsive interactions favour full occupancy of only one sublattice. Interestingly, at intermediate temperatures two partially ordered states are predicted, corresponding to cations distributed over two and three of the sublattices illustrated in figure 18, with their relative stabilities determined by the ratio of the nn and nnn repulsive interactions [173, 174]. MD simulations of $\alpha$-AgI on cooling, which allowed the shape of the simulation box to change, successfully reproduced the $\alpha \rightarrow \beta$ transformation [60]. To probe the ordering process within the $\alpha$ phase, other studies did not allow reorganization of the $I^-$ sublattice to form the hexagonal $\beta$-AgI structure, with local ordering of the $Ag^+$ onto one of the sublattices illustrated in figure 18 observed at temperatures less than ≈500 K [175]. However, subsequent simulations showed that a different ordering scheme was preferred at temperatures below the stability range of $\alpha$-AgI [176]. A monoclinic arrangement of $Ag^+$ was suggested to be the driving force for transformation to the $\beta$ phase [176], though more recent calculations using density functional theory [177] and lattice MC methods [178] claimed that the structural change of the $I^-$ and ordering of the $Ag^+$ are correlated, rather than the latter driving the former.

In practice, the $\alpha \rightarrow \beta + \gamma$ transition occurs very quickly in bulk AgI and the superionic $\alpha$ phase cannot be obtained at ambient temperature by quenching methods [172]. However,

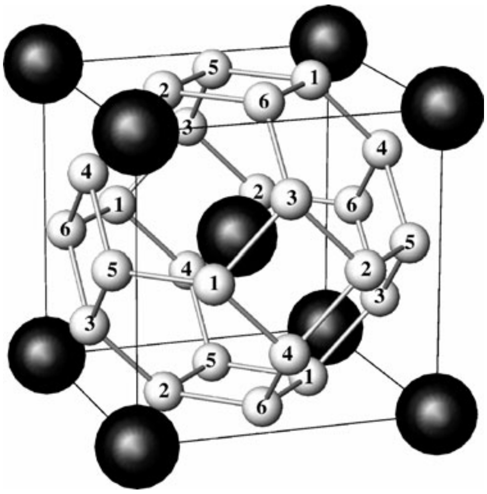

**Figure 18.** Schematic diagram of a bcc-structured sublattice (larger spheres) illustrating the division of the *tet* interstices into six interpenetrating bcc sublattices (numbered smaller spheres) (after [173, 174]).

it has been demonstrated that small particles of $\alpha$-AgI can be formed at ambient temperature inside samples of $(\mathrm{AgI})_x$–$(\mathrm{Ag_3BO_3})_{1-x}$ glasses rapidly quenched from the melt [179]. Glass formation in this system occurs over the composition range $0.57 \leqslant x \leqslant 0.87$, but at AgI concentrations slightly higher than the glass forming limit $\alpha$-AgI particles of ~20–40 nm in size [180] are frozen in, provided the cooling rate exceeds $\sim 10^5\,\mathrm{K\,s^{-1}}$ [179]. The resultant glass+crystallite composites have relatively high conductivities ($\sigma_\mathrm{i} \sim 10^{-2}\,\Omega^{-1}\,\mathrm{cm}^{-1}$), whilst slower cooling produces poorly conducting glasses containing particles of $\beta$-AgI. The excess AgI also forms $\beta$-phased particles for $x > \approx 0.91$ [179]. The ability to retain $\alpha$-AgI particles at ambient temperature has been attributed to the presence of large heterogeneous lattice strains at the AgI–glass matrix boundary [180] and heating the samples relieves these strains and accelerates the $\alpha \rightarrow \beta$ transition [181]. On cooling the $\alpha$-AgI containing glasses, a peak in the specific heat $C_p$ [182] and a change in the slope of $\sigma_\mathrm{i}$ versus $T$ [181] were observed at ≈270 K and interpreted as ordering of $\mathrm{Ag^+}$ within the bcc sublattice of the $\alpha$-AgI particles [181]. It would be interesting to determine whether this followed one of the schemes illustrated in figure 18.

### 3.6. *The room temperature superionic: $\mathrm{RbAg_4I_5}$*

The more conventional approach to stabilize high temperature phases under ambient conditions is chemical doping, using isovalent or aliovalent species incorporated into either the immobile or mobile sublattices. The favourable properties of the bcc sublattice and relatively low superionic transition temperature have made AgI the most popular parent compound, with the various doping options illustrated schematically in figure 19.

Replacing some of the $\mathrm{Ag^+}$ or $\mathrm{I^-}$ with isovalent species which are members of the family of $\mathrm{Ag^+}$/$\mathrm{Cu^+}$ halide superionics forms extensive solid solutions in which the stoichiometry is unchanged. In general, these systems have lower values of $\sigma_\mathrm{i}$, despite evidence that both cation species are mobile in the solid solution $(\mathrm{Ag}_{1-x}\mathrm{Cu}_x)\mathrm{I}$ [183], and a significant reduction in the superionic transition temperature in $\mathrm{Ag(I}_{1-x}\mathrm{Br}_x)$ with increasing $x$ [184]. The addition of other isovalent cation species generally incorporates ions which are significantly larger than $\mathrm{Ag^+}$,

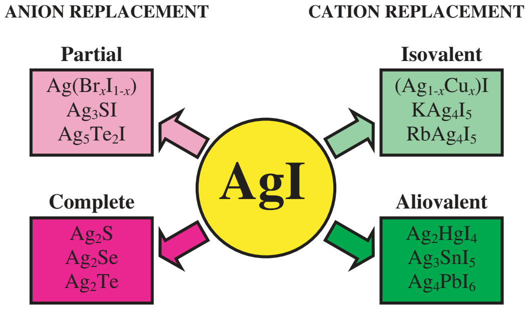

**Figure 19.** Schematic diagram of possible chemical doping schemes based on AgI, illustrating the various superionic compounds formed by replacement of some (or all) of the anions or cations.

resulting in solid solutions with much lower concentration limits and an increased tendency to form discrete ternary phases. Extensive, but largely unsuccessful, attempts have been made to identify high conductivity compounds formed by the addition of $MX$ ($M = K^+$, $Rb^+$ and $Cs^+$; $X = Cl^-, Br^-, I^-$) to their corresponding silver and copper halides [185–188]. Of the 30 or so ternary phases identified in the $(AgX)_x$–$(MX)_{1-x}$ and $(CuX)_x$–$(MX)_{1-x}$ phase diagrams, $RbAg_4I_5$ is the only one to attract extensive interest [114, 189–193], because it possesses one of the highest values of ionic conductivity at ambient temperature ($\sigma_i = 0.21(6)\,\Omega^{-1}\,cm^{-1}$ [193]). Although $RbAg_4I_5$ has been the focus of several trials for solid state battery applications [194, 195], problems of high raw material cost and relatively low energy densities have hampered its commercial viability. The former drawback can, in principle, be overcome by replacing $Ag^+$ by $Cu^+$, though the compound $RbCu_4I_5$ does not exist and a reduction in the size of the anion sublattice is required to compensate for the smaller $Cu^+$, as in the case of $RbCu_4Cl_3I_2$ [196,197].

An important structural criterion for obtaining good $Ag^+$ room temperature conductors is to discourage close packing of $Ag^+$ [198] and the most convenient method to achieve this goal is to retain the bcc sublattice characteristic of $\alpha$-AgI. However, the immobile $Rb^+$ within $RbAg_4I_5$ do not stabilize the high temperature $\alpha$-AgI form but instead force the anion sublattice to adopt an alternative structure that approximates to that of metallic Mn in its $\beta$ modification (space group $P4_132$ [189, 190]). The $\beta$-Mn-structured anion sublattice within $RbAg_4I_5$ possesses non-intersecting one-dimensional strings of tetrahedrally co-ordinated sites parallel to the three $\langle 100 \rangle$ directions, which form convenient conduction pathways for $Ag^+$ (see figure 20 [193]). Further discussions of the 'determinative structural role' of isovalent minority cations in promoting the formation of anion arrangements conducive to high $Ag^+$ conductivity (including the use of organic radicals such a $C_5H_5NH^+$ and $(CH_3)_4N^+$) are given elsewhere [25]. However, the number of available *tet* sites per anion (three in the case of $RbAg_4I_5$) is invariably lower than that offered by the bcc sublattice (six) and, at least in principle, there remains the scope for still higher conductivities within compounds in the latter category.

### 3.7. The role of dopant cations: $Ag_2MI_4$, $Ag_3MI_5$ and $Ag_4MI_6$ compounds

The addition of aliovalent $M^{2+}$ species to AgI forms compounds such as $Ag_2CdI_4$ [199, 200], $Ag_2HgI_4$ [201], $Ag_2ZnI_4$ [202], $Ag_3SnI_5$ [203] and $Ag_4PbI_6$ [204, 205], in which two mobile cations ($2 \times Ag^+$) are replaced by a single divalent one ($M^{2+}$) and a vacancy ($\Box$). At ambient temperature, $\varepsilon$-$Ag_2CdI_4$ and $\beta$-$Ag_2HgI_4$ adopt tetragonal structures (space groups $I\bar{4}2m$ [206] and $I\bar{4}$ [207], respectively) in which the $2 \times Ag^+$, $M^{2+}$ and $\Box$ are arranged in slightly different ways over the tetrahedrally co-ordinated sites occupied by $Ag^+$ in zincblende-structured $\gamma$-AgI.

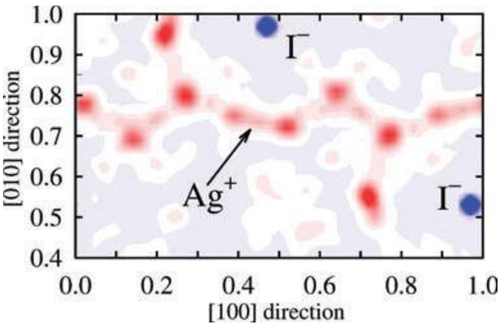

**Figure 20.** The time-averaged ionic density within $RbAg_4I_5$ at ambient temperature. The (001) section shown is a slice with $0.45 \leqslant z \leqslant 0.55$. The distribution of $Ag^+$ in the [100] direction at $y \approx \frac{3}{4}$ demonstrates that the cations diffuse predominantly along one-dimensional channels within the $\beta$-Mn-structured anion sublattice. The peaks in the $Ag^+$ density at $x \approx 0.22$, $y \approx 0.95$ and $x \approx 0.72$, $y \approx 0.55$ are parts of channels running perpendicular to the plane of the figure. There is some evidence of $Ag^+$ hopping between different channels (for details, see [193]). Copyright (2002), with permission from Elsevier.

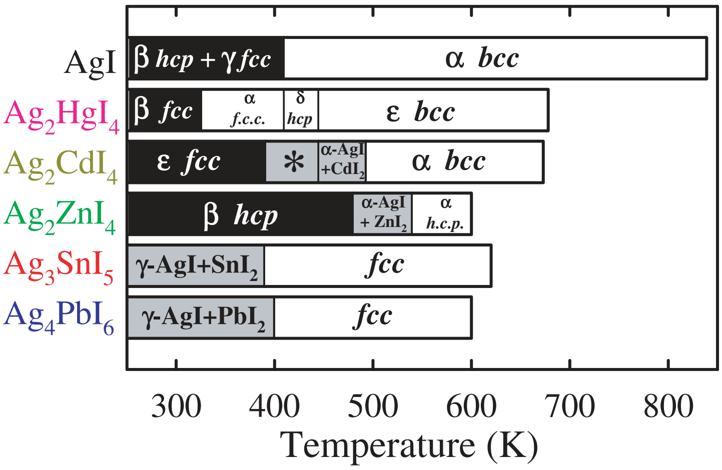

**Figure 21.** Schematic diagram summarizing the structural behaviour of AgI and the $Ag^+$-rich phases in the AgI-$MI_2$ systems. A black background indicates low conductivity phases, grey denotes mixed phase regions, whilst superionic phases have a white background. In the case of $Ag_2CdI_4$, the region labelled $*$ is a mixture of $\beta$-$Ag_2CdI_4$, $\beta$-AgI and $CdI_2$ (after [206]).

The crystal structure of $\beta$-$Ag_2ZnI_4$ is generated in an analogous manner by filling the *tet* sites occupied by the cations in wurtzite-structured $\beta$-AgI, leading to orthorhombic symmetry (space group $Pmn2_1$ [206]). $Ag_3SnI_5$ and $Ag_4PbI_6$ are only stable at elevated temperatures, but cover relatively wide compositional ranges [203–205].

To a good approximation, the differences in stoichiometry can be ignored and the five compounds $Ag_2HgI_4$, $Ag_2CdI_4$, $Ag_2ZnI_4$, $Ag_3SnI_5$ and $Ag_4PbI_6$ treated as a single family. Their high temperature structural behaviour is relatively complex and includes superionic and poorly conducting phases, plus some two-phase regions (see figure 21 [206]). A recent extensive series of ionic conductivity and diffraction studies have identified seven superionic phases, formed with bcc ($\alpha$-$Ag_2CdI_4$ [206] and $\varepsilon$-$Ag_2HgI4$ [208]), hcp ($\delta$-$Ag_2HgI_4$ [208] and $\alpha$-$Ag_2ZnI_4$ [206]) and fcc ($\alpha$-$Ag_2HgI_4$ [207], $Ag_3SnI_5$ [206] and $Ag_4PbI_6$ [209]) anion

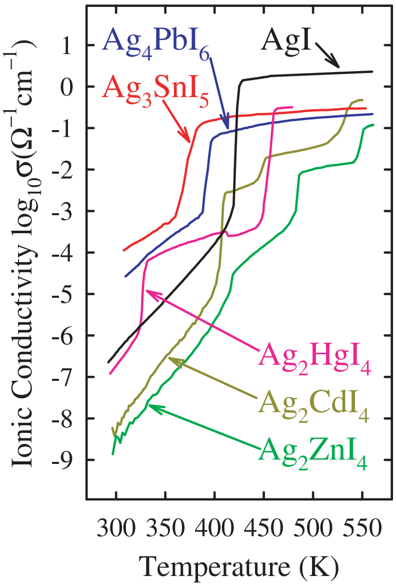

**Figure 22.** The temperature variation of the ionic conductivity, $\sigma_i$, of AgI, $Ag_2CdI_4$, $Ag_2ZnI_4$, $Ag_2HgI_4$, $Ag_3SnI_5$ and $Ag_4PbI_6$ (after [206]). The various phase transitions can be identified with reference to figure 21.

sublattices. The latter three cases are of particular interest, because ionic conductivity data (figure 22) show that the addition of the $M^{2+}$ dopant ions lowers the superionic transition temperature relative to pure $\alpha$-AgI (from 420 to 326(2) K in the case of $Ag_2HgI_4$ [207]). Unfortunately, this occurs at the cost of a large reduction in $\sigma_i$, even though the divalent ions are also mobile [210]. This decrease is too large to be attributed solely to the reduction in the number of charge carriers per anion in the ternary systems. As illustrated in figure 21, the superionic phases $\alpha$-$Ag_2HgI_4$, $Ag_3SnI_5$ and $Ag_4PbI_6$ possess fcc anion sublattices and the arguments made in section 3.3 based on the number of available *tet* interstices are more significant. Indeed, neutron diffraction studies of $\alpha$-$Ag_2HgI_4$ indicated that only those sites occupied within zincblende-structured $\gamma$-AgI are occupied [207], which further halves the number of sites available in the fcc sublattice relative to the bcc one (see figure 4). Presumably this restriction avoids unfavourable Coulomb repulsions between divalent cations simultaneously occupying nearest neighbour sites separated by $a/2$ in $\langle 100\rangle$ directions. Interestingly, the fcc-structured phases $Ag_3SnI_5$ [206] and $Ag_4PbI_6$ [209] differ from $\alpha$-$Ag_2HgI_4$ because the cations predominantly occupy *oct* sites within the $I^-$ sublattice. Within the (ordered) binary halides, the cations adopt tetrahedral anion co-ordination in $HgI_2$ and octahedrally co-ordinated environments in $SnI_2$ and $PbI_2$ [83]. Thus, the $M^{2+}$ ions adopt their 'favoured' co-ordination within the three ternary superionic phases but, at present, there is no explanation of how the dopant $M^{2+}$ species 'impose' their preferred co-ordination on the mobile $Ag^+$.

The tendency of the divalent cations to favour the formation of fcc sublattices (and, in some cases, to move the stability of the bcc-structured phase to higher temperatures) is clearly undesirable. To explain this behaviour, it is important to note that the *tet* and *oct* sites with the bcc sublattice are both distorted. The *tet* interstices have I-cation-I angles of $2\sin^{-1}\sqrt{3/5} = 101.54^\circ$ and $2\sin^{-1}\sqrt{4/5} = 126.87^\circ$, rather than the ideal value of $2\sin^{-1}\sqrt{2/3} = 109.47^\circ$, and the *oct* interstices have four cation-I distances of $a/\sqrt{2}$ plus two shorter contacts of $a/2$. In contrast, both the *tet* and *oct* environments are 'ideal' within an fcc sublattice. The unique ability of $Ag^+$ ions to reside in several different and distorted environments is not, in general, shared by the dopant cations, which are better able to accommodate their requirement for near regular co-ordination if the anion sublattice adopts an fcc arrangement [206]. Whilst rather speculative, this argument parallels the much wider situation observed within ordered (non-superionic) compounds, where the filling of octahedrally and tetrahedrally co-ordinated cavities within an fcc array of identical ions generates numerous common structure types (zincblende, rocksalt, fluorite, spinel, etc), whereas compounds formed by filling some, or all, of the (distorted) cavities within a bcc-structured lattice are rather rare.

In summary, attempts to stabilize the high temperature bcc anion sublattice characteristic of $\alpha$-AgI by isovalent or aliovalent chemical replacement of some of the mobile (cation) species have proved largely fruitless. However, as illustrated in figure 19, an alternative strategy is to replace some of the (immobile) anions.

### 3.8. *The $\alpha$-AgI and perovskite structures: $Ag_3SI$*

The superionic phases $\alpha$-AgI and $\alpha$-$Ag_2S$ both comprise bcc-structured immobile sublattices and the AgI–$Ag_2S$ phase diagram [211] contains only one intermediate compound of stoichiometry $Ag_3SI$ [212–214]. $Ag_3SI$ exists in its $\alpha$ phase at temperatures above 519 K. Its structure is analogous to that of $\alpha$-AgI, with a random distribution of $S^{2-}$ and $I^-$ over the sites forming the bcc-structured anion sublattice and a highly disordered arrangement of mobile $Ag^+$ [215–218]. Samples that are annealed for prolonged periods at a temperature $\approx$450 K and slowly cooled to room temperature show complete long-range ordering of the two cation species over the 0, 0, 0 and $\frac{1}{2}, \frac{1}{2}, \frac{1}{2}$ positions. Diffraction studies of this so-called $\beta$-$Ag_3SI$ have generally concluded that the $Ag^+$ reside close to the *oct* positions, but displaced in one of four $\langle 100\rangle$ directions towards the neighbouring *tet* sites [216–220]. In contrast, quenching from the $\alpha$ phase stability region to room temperature retains the random distribution of $S^{2-}$ and $I^-$. This is the metastable phase labelled $\alpha$*-$Ag_3SI$ [217, 218, 221], which slowly converts to $\beta$-$Ag_3SI$ on heating above $\approx$325 K. Interest in the compound $Ag_3SI$ stems from the impressive ionic conductivity of the quenched $\alpha^*$ phased material at ambient temperature ($\sigma_i \approx 0.3\,\Omega^{-1}\,\mathrm{cm}^{-1}$ [222]), which exceeds that of the annealed $\beta$ phase by almost two orders of magnitude [222].

To explain the influence of $S^{2-}/I^-$ ordering on the dynamic behaviour of the $Ag^+$ within $Ag_3SI$ it is necessary to consider a hypothetical bcc-structured sublattice formed by equal numbers of two ionic species *A* and *B*. A random arrangement of *A* and *B* ions corresponds to an average structure which, studied by diffraction methods, would display $Im\bar{3}m$ symmetry and can be described as an '$\alpha$-AgI' structure. However, placing all the *A* ions on the $\frac{1}{2}, \frac{1}{2}, \frac{1}{2}$ sites and the *B* ions on the 0, 0, 0 sites lowers the symmetry to $Pm\bar{3}m$. As illustrated in figure 23, this process splits the six *oct* sites in $Im\bar{3}m$ into two symmetry independent sets of three in $Pm\bar{3}m$ (labelled *oct*1 and *oct*2). Recalling that the octahedral co-ordination is highly irregular (section 3.7), the *oct*1 and *oct*2 positions are inequivalent because the former has $2 \times B$ ions at the shorter distance of $a/2$ and the latter has $2 \times A$ ions. Assuming (arbitrarily) that the *A* ions are the larger of the two species, then the *oct*1 sites will become energetically favoured because they have the larger counter-ions at the longer of the two distances (4 at $a/\sqrt{2}$), rather than the opposite. For the *tet* positions, the site at $\frac{1}{2}, 0, \frac{1}{4}$ (for example) in $Im\bar{3}m$ symmetry becomes a $\frac{1}{2}, 0, z$ position in the $Pm\bar{3}m$ case and, with reference to figure 23, the net steric effect of the $2\times A$ and $2 \times B$ nearest neighbours will be to shift the position of the ions at the *tet* positions towards the 'favoured' *oct*1 sites (i.e. $z$ will be reduced from $\frac{1}{4}$ towards zero).

On these simple geometric grounds, ordering the anion species modifies the structure from one containing a network of numerous interconnected equivalent sites ($6 \times$ *oct* and $12 \times$ *tet*) to one in which there are only three isolated, favoured (*oct*1) cavities, though these

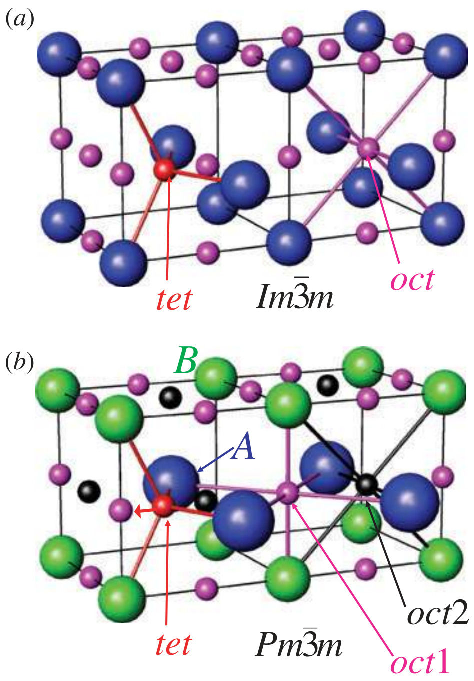

**Figure 23.** Schematic diagram showing the effect of ordering of two different ionic species *A* and *B* over the $\frac{1}{2}, \frac{1}{2}, \frac{1}{2}$ and 0, 0, 0 positions that form a bcc sublattice. The lowering of symmetry from (*a*) $Im\bar{3}m$ to (*b*) $Pm\bar{3}m$ splits the octahedrally co-ordinated *oct* sites into two independent sets, of which those labelled *oct*1 are more favourable because they have the larger *A* counterion at the larger distance (i.e. in $\langle 110 \rangle$ directions rather than $\langle 100 \rangle$). The favoured positions of the tetrahedrally co-ordinated sites (*tet*) are also moved in $\langle 100 \rangle$ directions towards the *oct*1 sites, as shown by the arrow. For clarity, only one *tet* site is illustrated. Overall, this process corresponds to the transition from (*a*) an $\alpha$-AgI type phase to (*b*) an (anti-) perovskite-structured one (after [227]).

are somewhat larger and extend towards the *tet* positions in four $\langle 100 \rangle$ directions. For $A = \mathrm{I}^-$ and $B = \mathrm{S}^{2-}$ (where $r_{\mathrm{I}^-} = 2.20$ Å and $r_{\mathrm{S}^{2-}} = 1.84$ Å [66]), the number of *oct*1 sites within the ordered $\beta$-$Ag_3SI$ phase equals the population of $Ag^+$. Clearly, this discussion offers a plausible explanation for the lower ionic conductivity of the $\beta$-phased material compared to $\alpha^*$-$Ag_3SI$ and is consistent with the $Ag^+$ distribution determined experimentally by neutron diffraction methods [218]. As illustrated in figure 24, the structural model which provides the best fit to the diffraction data distributes the cations over sites situated approximately midway between the *tet* and *oct*1 sites. These sites are grouped in fours and, with one $Ag^+$ per group, an equally valid description of the time-averaged distribution has the cations occupying the *oct*1 positions and undergoing extensive, anisotropic and anharmonic thermal vibrations towards the *tet* sites. For this reason, the crystal structure of $\beta$-$Ag_3SI$ is often described as an ‘anti-perovskite’ arrangement. However, perovskite-structured compounds, in which two cation species form the immobile bcc sublattice and anions sit in (or close to) the *oct*1 positions, are far more numerous than anti-perovskite-structured ones [223].

### *3.9. Perovskite-structured superionics: $MPbF_3$ compounds*

Exchanging the roles of the cations and anions to transform the anti-perovskite structure of $\beta$-$Ag_3SI$ into the perovskite one has a number of consequences for possible ionic diffusion.

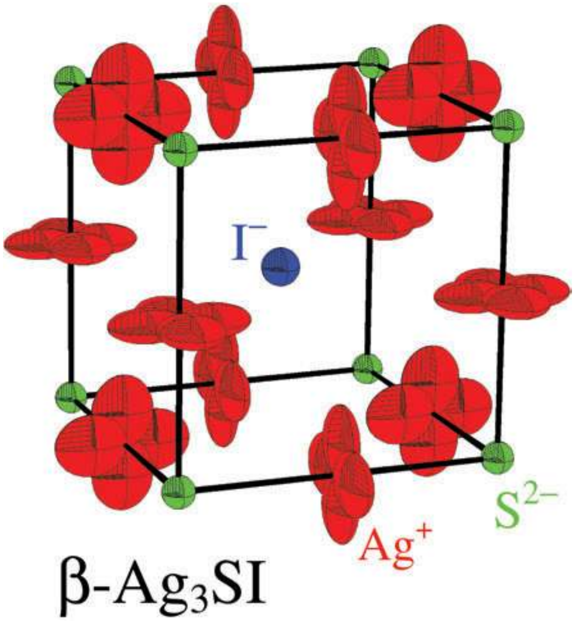

**Figure 24.** The time-averaged structure of $\beta$-$Ag_3SI$ at ambient temperature, illustrated using the thermal ellipsoids determined by powder neutron diffraction methods [218]. The extensive anisotropic and anharmonic thermal vibrations of the $Ag^+$ about the octahedrally co-ordinated cavities are clear.

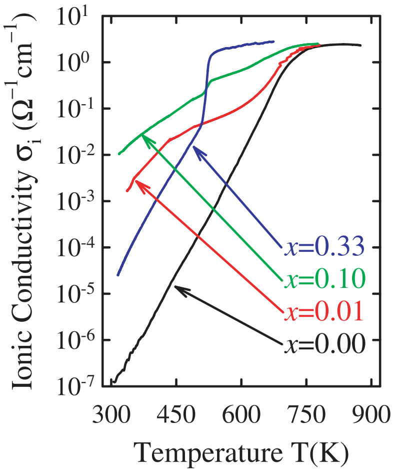

**Figure 25.** The temperature variation of the ionic conductivity, $\sigma_i$, of $(PbF_2)_{1-x}$–$(KF)_x$ with $x = 0.0, 0.01, 0.10$ and $0.30$ (after [227]). The appearance of a type-I superionic transition at ~520 K within the more highly doped samples is apparent.

These are demonstrated in this subsection by considering a group of ternary compounds chemically derived from $PbF_2$ rather than AgI.

As illustrated in figure 25 [224], the addition of $K^+$ to fluorite-structured $\beta$-$PbF_2$ initially causes a dramatic increase in the ionic conductivity of the material at temperatures close to ambient, due to the formation of charge compensating $F^-$ vacancies [82, 225, 226]. Of greater interest here is the appearance of a type-I superionic transition at ≈520 K within samples of higher $K^+$ contents ($x > \approx 0.1$) [224]. Neutron diffraction and impedance spectroscopy measurements of highly doped samples in the $(PbF_2)_{1-x}$–$(KF)_x$ system showed that the superionic phase exists as a single phase for samples with $0.33 \leqslant x < \approx 0.68$, possesses a high ionic conductivity ($\sigma_i \approx 2\,\Omega^{-1}\,cm^{-1}$) and adopts a bcc structure with $a \approx 4.66$ Å [224]. The $Pb^{2+}$ and $K^+$ are randomly distributed over the 0, 0, 0 and $\frac{1}{2}, \frac{1}{2}, \frac{1}{2}$ positions (such that the average symmetry is $Im\bar{3}m$) and the (highly disordered) anions reside predominantly on the *tet* positions, but with a significant fraction (up to ~25%) at the *oct* sites. There are subtle variations in the preferred site occupancies with $x$, which have been correlated with changes in $a$ and $\sigma_i$ [224]. However, the discussion here will be restricted to the $x = 0.5$ case, which corresponds to the stoichiometry $KPbF_3$.

The time-averaged structure of $KPbF_3$ described above can be considered broadly analogous to that of $\alpha^*$-$Ag_3SI$ rather than the (anti-perovskite) $\beta$-$Ag_3SI$ (section 3.8) but with the roles of the cations and anions reversed. As a consequence, it is the *larger* anions that are mobile within $KPbF_3$. Recalling the discussion in section 3.4, the size of the $F^-$ ion ($r_{F^-} = 1.31$ Å [66]) does not allow simultaneous occupancy of either nn or nnn tetrahedral interstices within the bcc-structured $Pb^{2+}/K^+$ sublattice, because these sites are separated by $\sqrt{2}a/4 \approx 1.65$ Å and $a/2 \approx 2.33$ Å, respectively. The populations of mobile ions and available tetrahedral sites are then equal (three per unit cell) and exclusive occupancy of *tet* positions would lead to a fully ordered arrangement of the type illustrated in figure 14(*b*). The high ionic conductivity requires additional occupancy of the *oct* sites, which is consistent with the observed site occupancies and analysis of diffuse neutron scattering data [224].

Unlike $Ag_3SI$, $KPbF_3$ cannot be prepared with an ordered arrangement of $K^+$ and $Pb^{2+}$ over the bcc-structured sublattice. However, the related compounds $RbPbF_3$ and $CsPbF_3$ adopt the space group $Pm\bar{3}m$ and are characterized by complete ordering of the two cation species [227]. In the case of $RbPbF_3$, the anions are distributed almost equally over the *tet* and *oct*1 positions (see figure 23(*b*)) and the conductivity is still relatively high ($\sigma = 0.1\,\Omega^{-1}\,cm^{-1}$ at ≈690 K [227]). $CsPbF_3$ adopts the cubic perovskite structure, with the anions localized on the *oct*1 sites, even at temperatures close to the melting point. As expected, the ionic conductivity is relatively low ($\sigma = 2.3 \times 10^{-3}\,\Omega^{-1}\,cm^{-1}$ at ≈700 K [227]).

The preferred anion locations and decreasing ionic conductivity within the sequence $KPbF_3 \rightarrow RbPbF_3 \rightarrow CsPbF_3$ are consistent with the simple geometric considerations given in section 3.8 and, in a wider sense, illustrates that ordering of two cation species over the $\frac{1}{2}, \frac{1}{2}, \frac{1}{2}$ and 0, 0, 0 sites within a bcc sublattice is detrimental to extensive ionic diffusion. Unfortunately, this long-range ordering is key to explaining the prevalence of the perovskite structure within $ABX_3$ compounds, because it allows cations of differing sizes to simultaneously adopt co-ordinations appropriate to their size (12-fold cuboctahedral sites for the larger $A$ ions and six-fold octahedral positions for the smaller $B$ ones). Furthermore, the cubic lattice parameter $a$ is the only degree of freedom within the cubic perovskite structure [228] and, in the hard sphere model of ionic contacts, it is necessary to simultaneously satisfy the radii conditions $r_A + r_X = a/\sqrt{2}$ and $r_B + r_X = a/2$. These requirements are combined in the so-called 'Goldschmidt tolerance factor' $t_G = (r_A + r_X)/\sqrt{2}(r_B + r_X)$ [229], which, in the ideal case, equals unity. So, the stability of the (cation-ordered) perovskite arrangement is contrary to the geometric requirements for high ionic conductivity and, as a consequence, perovskite-structured compounds are expected to display superionic behaviour at significantly higher temperatures than (cation-disordered) $\alpha$-AgI-structured ones, if at all.

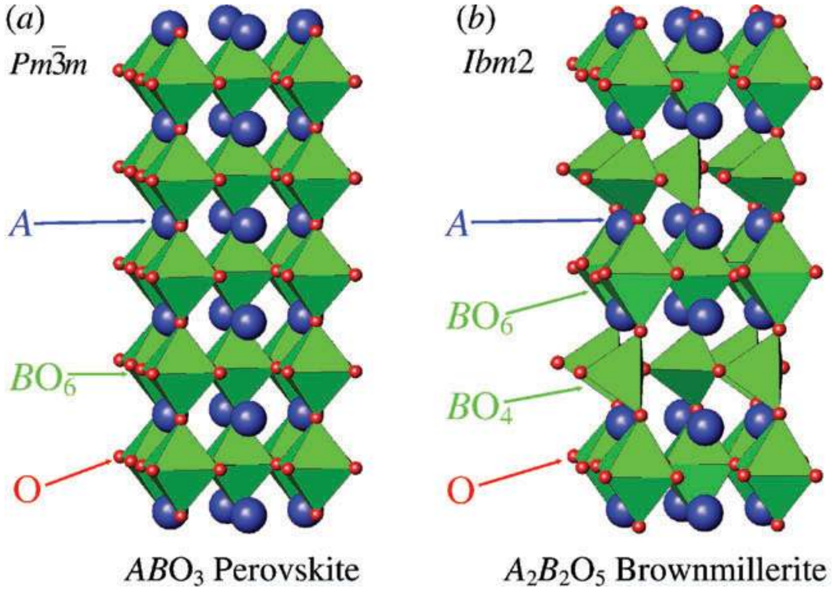

**Figure 26.** The relationship between the crystal structures of (*a*) a perovskite-structured oxide of stoichiometry $AB\mathrm{O}_3$ and (*b*) a brownmillerite-structured oxide of stoichiometry $A_2B_2\mathrm{O}_5$. The former is converted to the latter by replacing half of the $B\mathrm{O}_6$ octahedra with $B\mathrm{O}_4$ tetrahedra. Copyright (2002), with permission from Elsevier.

### *3.10. Distortions of the cubic perovskite structure: halide perovskites*

To develop the discussion of the ionic diffusion mechanisms within perovskite-structured compounds it is necessary to replace the structural picture of anions located in three (distorted) octahedral sites of an ordered bcc sublattice of $A$ and $B$ cations with an alternative description more familiar to crystallographers. The smaller $B$ cation species lie at the centre of an octahedron of anions and each $BX_6$ octahedron shares every corner with other $BX_6$ units, leading to a three-dimensional network. The $A$ cations then sit at the centre of a cube formed by eight corner-sharing $BX_6$ octahedra, with cuboctahedral co-ordination to 12 anions. The case of a perovskite-structured oxide is illustrated in figure 26(*a*).

In practice, perovskite-structured compounds are found to adopt the ideal cubic arrangement for $\approx 0.97 < t_{\mathrm{G}} < \approx 1.03$ [230, 231]. For larger values of $t_{\mathrm{G}}$ hexagonal structures are preferred, in which there is some degree of edge-sharing of the $BX_6$ octahedra [228]. The case of $t_{\mathrm{G}} < 1$ corresponds to the $A$ cations being too small for their cuboctahedral cavities and, as a consequence, co-operative rotations of the $BX_6$ octahedra about one or more of the major crystallographic axes brings some of the $12 \times X$ contacts closer to the $A$ cation [223][7]. The tilting of essentially rigid $BX_6$ octahedra within perovskites has been considered in detail [234, 235], with 15 possible structural models identified [235]. Of these, the octahedral tilting scheme which lowers the symmetry from $Pm\bar{3}m$ to $Pnma$ is amongst the most commonly found [231]. In this case, the rotation of the $BX_6$ octahedra reduces the size of all of the $A$ site interstices, which become slightly distorted towards a tricapped trigonal prismatic environment. The orthorhombic unit cell has dimensions $a \sim \sqrt{2}a_{\mathrm{perov}}$, $b \sim \sqrt{2}a_{\mathrm{perov}}$, $c \sim 2a_{\mathrm{perov}}$ (where $a_{\mathrm{perov}}$

---

[7] Even compounds that adopt the ideal cubic form at ambient temperature often show such distortions on cooling, including the perovskite-structured $\mathrm{CsPbF}_3$ (section 3.9) and the anti-perovskite-structured $\beta$-$\mathrm{Ag}_3\mathrm{SI}$ (section 3.8) ($Pm\bar{3}m \to R3c$ at $T = 187$ K [232] and $Pm\bar{3}m \to R3$ at $T = 157$ K [218, 233], respectively).

is the lattice parameter of the parent cubic form) and contains four $ABX_3$ formula units, with the anions arranged over two symmetry independent sites [228].

The two perovskite-structured compounds $KMgF_3$ and $NaMgF_3$ have $t_G = 1.024$ and 0.938, respectively [66]. As expected, the former possesses the undistorted cubic perovskite structure over a wide temperature range ($4.2 \leqslant T(\mathrm{K}) \leqslant 1223$ [236]) whilst $NaMgF_3$ adopts the *Pnma* variant [237] due to co-operative rotations of the $MgF_6$ octahedra by around 14° [238]. $NaMgF_3$ transforms to the cubic form at $\approx 1170$ K and was reported to undergo a type-II superionic transition just below the melting point ($T_m = 1303$ K) in which $\sigma_i$ reaches $\approx 1.3\,\Omega^{-1}\,\mathrm{cm}^{-1}$ [239]. However, a subsequent MD simulation failed to observe any significant diffusion of either the anions or cations, even with strong superheating [240]. Subsequent measurements of the ionic conductivity of $NaMgF_3$ found no evidence for any abnormal increase in $\sigma_i$ at elevated temperatures and suggested that the previous measurements resulted from spurious surface electronic conduction [241]. Indeed, the presence of superionic behaviour within many fluoride perovskites has been the subject of much debate within the literature, with conflicting evidence for and against extensive $F^-$ ion diffusion in compounds such as $KMgF_3$ [241, 242], $NaMgF_3$ [237, 239–243], $KCaF_3$ [242, 244–246] and $KZnF_3$ [241, 244, 247, 248] on the basis of ionic conductivity measurements, NMR studies, neutron diffraction experiments, MD simulations and investigations of the mechanical properties.

### 3.11. Superionicity in the lower mantle: $MgSiO_3$

A major motivation for the high temperature studies of halide perovskites such as $NaMgF_3$ stems from their role as structural analogues to the perovskite-structured oxide magnesium silicate. $MgSiO_3$ is a major constituent of the earth's lower mantle, which extends from a depth below the surface of $\approx 670$ to $\approx 2900$ km and constitutes approximately half of the volume of our planet. Probable pressure and temperature ranges within the lower mantle are $\approx 24 < p(\mathrm{GPa}) < \approx 135$ and $\sim 2000 < T(\mathrm{K}) < \sim 3000$ [249]. Under these conditions, $MgSiO_3$ exists in a perovskite-structured phase and metastable samples quenched from elevated pressures and temperatures to ambient conditions show the *Pnma* modification discussed in the previous subsection [250].

Considerable research effort has been devoted to elucidating the structural properties of $MgSiO_3$ within its $p$–$T$ stability field, following suggestions that it may display superionic behaviour within the lower mantle [251]. The presence of an ionically conducting solid phase would have consequences for the earth's geophysical behaviour, because the conductivity of the lower mantle controls the transmission of geomagnetic signals from the core to the surface. This may, in turn, help to explain the abrupt 'jerks' in the magnetic field such as that observed in 1969 [251]. Indeed, the propagation of geomagnetic field variations was used to estimate that the conductivity of the lower mantle increases from $\sim 0.01$ to $\sim 1\,\Omega^{-1}\,\mathrm{cm}^{-1}$ when the depth is increased [252, 253]. However, other workers attributed these high values to the presence of water [254] and argued that extensive $O^{2-}$ disorder in $MgSiO_3$ is unlikely because pressure increases the activation energy for ionic diffusion [255]. MD studies suggested that a transition from the orthorhombic (*Pnma*) structure to a highly disordered cubic perovskite phase ($Pm\bar{3}m$) occurs with increasing temperature at pressures greater than 10 GPa [256]. Within the cubic phase, anion motion occurred along the edge of the $SiO_6$ octahedra in $\langle 110 \rangle$ directions [257]. Subsequent MD studies have both supported [258, 259] and contradicted [260] these findings, though a consistent aspect of these simulations is that extensive anion disorder is only observed within the cubic, rather than the orthorhombic, form. Experimentally, recent synchrotron x-ray studies using samples encapsulated in laser-heated diamond anvil cells find no evidence of a transition to the cubic phase at high pressures and temperatures [261, 262] and, therefore, tend not to support the presence of a superionic lower mantle.

### 3.12. *Selection criteria for high conductivity perovskites: $BaCeO_3$ and $LaGaO_3$*

Compounds that exhibit high oxygen ion conductivities at elevated temperatures are very desirable for use as solid electrolytes to provide ‘clean’ electrical power in high energy density fuel cells [31, 33, 34]. Putting aside any commercial, environmental and fabrication considerations, the key requirements for this role are a high ionic conductivity, $\sigma_{\mathrm{i}}$, coupled with a low electrical conductivity, $\sigma_{\mathrm{e}}$. A number of systematic selection criteria have been proposed as a means of identifying promising candidate materials, based largely on steric considerations and ‘chemical sense’ [263–269]. In the case of perovskite-structured $AB\mathrm{O}_3$ oxides, these can be summarized as follows:

- The material should possess low metal–oxygen binding energies to allow the $\mathrm{O}^{2-}$ to ‘break free’ and diffuse through the lattice.
- *B* site cations with multiple valence states should be avoided, since they can give rise to an unwanted contribution from electronic conduction.
- The Goldschmidt tolerance factor $t_{\mathrm{G}}$ should be close to unity, so that the material adopts the ideal cubic perovskite structure. This enhances $\sigma_{\mathrm{i}}$ by making all the oxygen sites crystallographically (and, therefore, energetically) equivalent, but this is not the case for the distorted *Pnma* variant of the perovskite structure discussed in the previous subsections.
- The ‘free volume’ ($V_{\mathrm{Free}} = a^3 - \sum_{A,B,\mathrm{O}} \frac{4}{3}\pi r^3$) should be as large as possible to maximize the space available for $\mathrm{O}^{2-}$ diffusion. However, it has been shown that $V_{\mathrm{Free}}$ increases with decreasing $t_{\mathrm{G}}$, which is contrary to the requirement of the previous criterion [268]. As a compromise, an optimum value of $t_{\mathrm{G}} \approx 0.96$ has been proposed [268].
- On the assumption that anion diffusion in perovskites occurs in $\langle 110 \rangle$ directions along the edges of the *B*-centred octahedra [270], the $\mathrm{O}^{2-}$ must diffuse through a triangular ‘aperture’ formed by $2 \times A$ and $1 \times B$ cations and its radius ($r_{\mathrm{Crit}} = (r_A^2 + 3a^2/4 - \sqrt{2}ar_B + r_B^2)/(2r_A + \sqrt{2}a - 2r_B)$) must be greater than $r_{\mathrm{O}^{2-}}$ [265, 266]. However, this concept has been questioned, because computer simulations showed that the $\mathrm{O}^{2-}$ follow a curved path along the edge of the octahedra to avoid the *B* site cation and significant outward relaxations of the *A* and *B* cations occur [271, 272].

The points listed above may appear rather naive, but their validity can be demonstrated with reference to real compounds [268]. For example, the last two criteria require that the *A* cation be as large as possible. In the case of $A^{3+}B^{3+}\mathrm{O}_3$ perovskites, the largest suitable trivalent cation is $\mathrm{La}^{3+}$ and the requirement for $t_{\mathrm{G}} \approx 0.96$ makes $\mathrm{Ga}^{3+}$ the most appropriate *B* site cation. $\mathrm{LaGaO}_3$ and its derivatives are indeed excellent oxide-ion conducting perovskites (see, e.g. [273]). Similar arguments for the case of $A^{2+}B^{4+}\mathrm{O}_3$ perovskites can be used to ‘predict’ the impressive conducting properties of $\mathrm{BaCeO}_3$. However, whilst oxide ion conductivity in this compound dominates at temperatures in excess of $\sim$1100 K [274], protonic charge carriers can be incorporated into the oxide perovskite lattice via the absorption of water molecules from the air, leading to an enhanced conductivity at lower temperatures [275, 276]. Due to its small size and high polarizing power, the bare proton does not conduct in the same way as other ions and $\mathrm{H}^+$-ion conductors will not be discussed here (though there are a number of comprehensive reviews of this important issue, including [277–279]).

To derive meaningful empirical relationships between the crystal structure (including any distortions of the perovskite lattice) and the bulk $\mathrm{O}^{2-}$ conduction the former needs to be accurately determined, especially at the elevated temperatures at which high ionic conductivity is observed. $LaGaO_3$ and $BaCeO_3$ both adopt the *Pnma* distorted perovskite arrangement at ambient temperature, but their structural behaviour on heating has proved controversial (see [280–285] and [286–288], respectively). In the latter compound, three high temperature phases are observed [288], but major discrepancies between the space group symmetries determined by Raman spectroscopy and diffraction methods have been reported. It is often difficult to extract the correct description of the crystal structure using x-ray diffraction, because the tilts of the $BO_6$ octahedra primarily involve displacements of the lighter $O^{2-}$ and the reflections that violate the parent cubic $Pm\bar{3}m$ symmetry tend, therefore, to be very weak. In addition, the distortions of the unit cell are generally small, resulting in only slight splittings of the Bragg peaks. Consequently, high resolution neutron diffraction techniques have proved to be the most appropriate for their study [288]. Attempts to reconcile the previous Raman and diffraction data for $BaCeO_3$ have recently been made [287] and favour the *Pnma*—563 K → *Imma*—673 K → $R\bar{3}c$—1173 K → $Pm\bar{3}m$ sequence of transitions determined by neutron diffraction methods [286, 288].

The absence of large empty cavities within the perovskite structure effectively precludes the formation of anion- and cation-excess perovskites by aliovalent chemical doping methods. However, the alternative possibility of replacing some of the *B*-site cations by species of a lower valence to generate charge compensating anion vacancies has long been established as a means of enhancing the ionic conductivity at lower temperatures [275]. In this case, two additional criteria to those listed above have been proposed [265, 268]:

- The dopant cation should possess a similar radius to the *B* site cation it replaces, to avoid changing $t_G$ and introducing local distortions into the lattice, which would hinder anion migration.
- The introduction of $O^{2-}$ vacancies increases the free volume available for anion diffusion, causing an initial increase in $\sigma_i$ with $\delta$ in $ABO_{3-\delta}$ (see, e.g. [289]). However, a systematic study of the published literature on oxide-ion perovskites shows that an optimum value of oxygen non-stoichiometry is $\delta \sim 0.2$, because reductions in $\sigma_i$ occur at higher $\delta$ values due to short-range interactions between anion vacancies [268].

An example of the ‘radius matched’ doping scheme is provided by $Ba(Ce_{1-x}Y_x)O_{3-x/2}$ and its $Gd^{3+}$ and $Nd^{3+}$ doped analogues, which have significantly higher ionic conductivities than pure $BaCeO_3$ [32]. Neutron diffraction studies indicated that the extrinsic vacancies are preferentially located on one of the two sets of anion positions [290] though (as in the pure material) there has been disagreement between Raman [291] and neutron diffraction [292] studies concerning the symmetry changes induced by doping. In the case of $LaGaO_3$, partial replacement of both the *A* and *B* sites with comparably sized cations leads to the system $(La_{1-x}Sr_x)(Ga_{1-y}Mg_y)O_{3-x/2-y/2}$, which has been studied by conductivity [273, 293–296], diffraction [282, 284, 285] and computer modelling techniques [272, 297, 298]. For $x \approx 0.1$ and $y \approx 0.1$, its ionic conductivity is $\approx 0.1\,\Omega^{-1}\,cm^{-1}$ at $\sim 1100\,K$ [273, 296]. $(La_{1-x}Sr_x)(Ga_{1-y}Mg_y)O_{3-x/2-y/2}$ is thus a promising solid electrolyte to allow oxide fuel cells to operate at lower temperatures than the current ‘best’ material, the anion-deficient fluorite-structured $(Zr_{1-x}Y_x)O_{2-x/2}$ (which will be discussed in section 4.7) [299, 300].

### 3.13. Anion-deficient perovskites: $Ba_2In_2O_5$ and $MBi_3O_{5.5}$

The onset of short-range correlations between the positions of the $O^{2-}$ vacancies, which causes the reduction in the ionic conductivity of anion-deficient $ABO_{3-\delta}$-type perovskites for $\delta > \sim 0.2$, tends towards long-range ordering as the vacancy concentration increases further. This process is illustrated by the $\delta = 0.5$ case, which corresponds to the stoichiometry $A_2B_2O_5$.

There are many possible patterns of vacancy ordering, with some of the $BO_6$ octahedra replaced by $BO_5$ square pyramids ($Ca_2Mn_2O_5$), $BO_4$ square planar units ($La_2Ni_2O_5$), $BO_4$ tetrahedra ($Ca_2Fe_2O_5$) or combinations thereof [301]. The formation of $BO_4$ tetrahedra leads to the so-called brownmillerite structure type and is particularly relevant in the context of highly conducting solids. The brownmillerite arrangement is an orthorhombic superstructure of the cubic perovskite structure, with $a \sim \sqrt{2}a_{\mathrm{perov}}$, $b \sim 4a_{\mathrm{perov}}$ and $c \sim \sqrt{2}a_{\mathrm{perov}}$. In the [010] direction there is an alternating sequence of corner-sharing octahedra and tetrahedra, with alternate rows of the latter having different orientations (see figure 26(*b*)). However, slight displacements of the ions away from their idealized positions occur and the correct symmetries of brownmillerite-structured compounds have been the subject of some debate, with closely related descriptions in space groups *Icmm*, *Ibm*2 and *Pcmn* proposed [302].

The brownmillerite-structured compound $Ba_2In_2O_5$ has been reported to undergo a type-I superionic transition at $\approx$1200 K, with $\sigma_{\mathrm{i}} \approx 0.1\,\Omega^{-1}\,\mathrm{cm}^{-1}$ immediately above the transition [303]). The crystal structure of $Ba_2In_2O_5$ under ambient conditions has recently been determined to possess *Icmm* symmetry [304] (in contrast to a previous report [305]) and contains (static) disorder of the $InO_4$ tetrahedra over their two different orientations. This leads to a rather complex microstructure [304]. Diffraction studies performed at temperatures in excess of $\approx$1300 K show that $Ba_2In_2O_5$ adopts an anion-deficient cubic perovskite structure [304, 306, 307], in which the $O^{2-}$ sites have a mean occupancy of $\frac{5}{6}$ and the anions undergo highly anisotropic thermal vibrations [304]. However, there is disagreement over the presence of an intermediate tetragonal phase (space group *I*4*cm*) between the orthorhombic and cubic forms and it is not clear whether the high ionic conductivity is associated with the tetragonal and/or cubic-structured phases [304, 306–308]. Despite these uncertainties, several attempts to synthesize highly anion-deficient cubic perovskite-structured compounds based on $Ba_2In_2O_5$ have been made, including compositions around $Ba_2InCoO_5$ ($\delta = 0.5$) [309] and $Ba_3In_2ZrO_8$ ($\delta = 0.333$) [303, 304, 310].

A second example of anion-deficient phases derived from the cubic perovskite structure is provided by compounds of stoichiometry $MBi_3O_{5.5}$, which correspond to $\delta = 0.25$. Specifically, the $M = Cd^{2+}$ and $Ba^{2+}$ materials have been reported to possess high ionic conductivities at elevated temperatures [311]. The relative similarity between the ionic sizes of $Cd^{2+}$ and $Bi^{3+}$ ($r_{Cd^{2+}} = 1.24$ Å and $r_{Bi^{3+}} = 1.31$ Å [66]) and the arguments presented in sections 3.8 and 3.9 suggest that $CdBi_3O_{5.5}$ will adopt a perovskite-structured arrangement with the two cation species disordered over the *A* and *B* cation sites. This has been confirmed experimentally, and the $O^{2-}$ found to reside in the *tet* sites of space group $Im\bar{3}m$ [312]. For the $M = Ba^{2+}$ analogue, the significantly larger size of the divalent cation ($r_{Ba^{2+}} = 1.56$ Å) favours ordering of the $Ba^{2+}$ and $Bi^{3+}$ and the resultant displacement of the anions onto the *oct*1 sites of space group $Pm\bar{3}m$ (see figure 23). However, x-ray diffraction studies of $BaBi_3O_{5.5}$ initially suggested that the material possesses $Im\bar{3}m$ symmetry, with disordered cations and the anions randomly distributed over all six equivalent *oct* cavities [313]. This apparent paradox has been resolved by subsequent neutron diffraction, electron diffraction and high resolution electron microscopy (HREM) studies [314, 315], showing that short-range ordering of both cations and anion vacancies occurs. This leads to a complex structure formed by an intergrowth of regions of composition $BaBiO_3$ (with close to the ideal cation-ordered perovskite structure) and rocksalt-like $Bi_2O_{2-x}$ blocks, in a manner similar to the so-called 'Ruddlesden–Popper' phases [316, 317].

### 3.14. Perovskite intergrowth structures: the BiMeVOx compounds

A second example of layered structures based on sections of a perovskite-structured lattice is provided by the so-called Aurivillius phases [318–320], which can be described as an

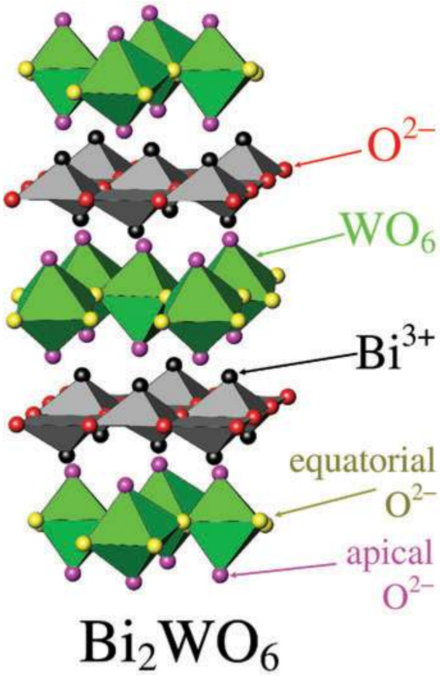

**Figure 27.** The crystal structure of $Bi_2WO_6$ [322], showing the layers of edge-sharing $Bi^{3+}$ capped $BiO_4$ square pyramids sandwiched between perovskite-like sheets of corner-sharing $WO_6$ octahedra. The locations of the apical and equatorial anions within the perovskite-like layers are illustrated. This ionic arrangement forms the basis of the Bi*Me*VOx family of oxygen-ion conductors (see section 3.14).

intergrowth of $n$ perovskite-like layers of composition $(A_{n-1}B_nO_{3n+1})^{2-}$ and bismuth oxide $(Bi_2O_2)^{2+}$ sheets. The latter consist of edge-shared $BiO_4$ groups, in which the $Bi^{3+}$ and $4 \times O^{2-}$ form the apex and square base of pyramidal polyhedra, respectively. This geometry accommodates the specific stereochemical requirements of the former's $6s^2$ lone-pair electrons [321]. The case of $n = 1$ is illustrated by the compound $Bi_2WO_6$ in figure 27 [322]. Closely related compounds with high ionic conductivities at relatively low temperatures (~600 K) can be generated by replacing the $W^{6+}$ with lower valence cations, such as $V^{5+}$ to form $Bi_4V_2O_{11}$ [323]. In this material the perovskite-like layer has a composition $VO_{3.5}$ and within the disordered high temperature tetragonal phase (labelled $\gamma$) the oxygen sites are, on average, $\frac{7}{8}$ occupied [324]. On cooling, the $\gamma$ phase transforms to the orthorhombic $\beta$ form at ≈845 K [324, 325] and to the monoclinic $\alpha$ phase at ≈700 K [324, 326]. Both are characterized by low ionic conductivities, preferential ordering of the vacancies over the anion sites within the perovskite-like layers and co-operative displacements of the $V^{5+}$, leading to lower symmetries and larger unit cells [323–328].

Numerous attempts to stabilize the high temperature $\gamma$ phase of $Bi_4V_2O_{11}$ at ambient temperature have been made by replacing some of the $V^{5+}$ with other metal cations (*Me*). This generates the so-called Bi*Me*VOx family of compounds [329]. To date, over 35 cation species have been incorporated into $Bi_4V_2O_{11}$, ranging in size from $B^{3+}$ to $Ba^{2+}$ and in valence from $Na^+$ to $Mo^{6+}$ (see [330]). Powder diffraction studies of quenched samples with $Me = Co^{2+}$ and $Ni^{2+}$ suggested that the anion vacancies are predominantly located on the equatorial positions of the perovskite-like layer (see figure 27) [331, 332]. This model is supported by the close agreement

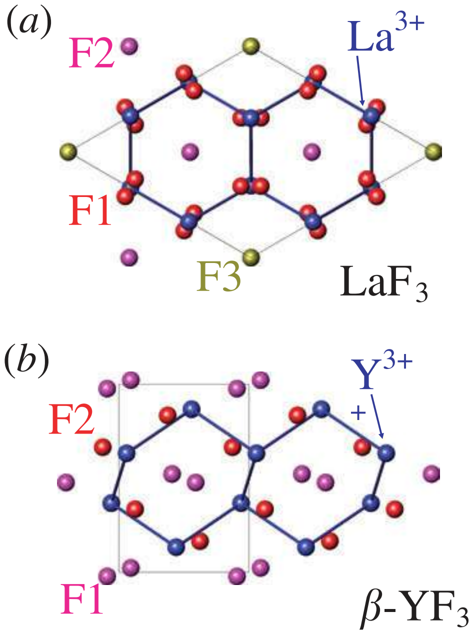

**Figure 28.** The relationship between (*a*) the tysonite crystal structure adopted by LaF$_3$ and (*b*) the $\beta$-YF$_3$ structure. In both cases the sublattice formed by the trivalent cations is shown in blue, whilst the unit cells are illustrated by thin black lines. The two structures are viewed down [001] and [010], respectively, and contain three and two symmetry independent anion sites, respectively (after [348]).

between the observed and theoretical solid solution limits of different *Me* dopants, and has led to the proposal of a conduction mechanism involving movement of equatorial O$^{2-}$ and vacancies between vanadium-centred octahedra and tetrahedra and the formation of an intermediate five-fold co-ordinate V$^{5+}$ arrangement [333]. However, such predictions are at odds with the results of recent $^{17}$O NMR measurements of the $Me$ = Ti$^{4+}$ material, which indicate rapid hopping of the anions between the axial and equatorial positions [334]. Furthermore, many of the $\gamma'$-phased Bi*Me*VOx compounds form extremely complex structures, with ordering of the anion vacancies leading to incommensurate superstructures [335, 336]. Whilst the ionic conductivities of the $\gamma'$ phases are relatively impressive [337], their behaviour can degrade with time at modest temperatures due to the gradual transition to an $\alpha$-Bi$_4$V$_2$O$_{11}$-related phase [338]. In addition, the possibility of V$^{5+}$ → V$^{4+}$ reduction can cause a significant electronic contribution to the conductivity which could prove detrimental to their widespread use in fuel cell applications [339].

### *3.15. B-site deficient perovskites: tysonite-structured LaF$_3$*

The various co-operative tilting schemes demonstrated by the $BX_6$ octahedra within stoichiometric $ABX_3$ perovskites mentioned in section 3.10 convert the cuboctahedral *A* interstices of the parent cubic structure into various icosahedra, rhombic prisms, octahedra, cubes, square anti-prisms and trigonal prisms [234, 340]. In the latter case, removing the *B* cations from the octahedra and making minor adjustments to the locations of the *X* anions generates two closely related structure types, the tysonite [340] and $\beta$-YF$_3$ arrangements (see figure 28).

The former is adopted by the lighter rare-earth trifluorides ($Re\mathrm{F}_3$ for $Re$ = La–Ho) and the latter is favoured by the remainder ($Re$ = Er–Lu) and by $\mathrm{YF}_3$ itself [341].

On heating, the tysonite-structured compounds with $Re$ = La–Pm retain this structural arrangement up to their melting points [342]. However, evidence for a type-II superionic transition within $\mathrm{LaF}_3$ at $T \approx 1200$ K was provided by specific heat data [343]. In contrast, the other tysonite-structured rare-earth trifluorides ($Re$ = Sm–Ho) undergo a first-order structural transition to the $\beta$-$\mathrm{YF}_3$ arrangement (space group *Pnma* [344]) at elevated temperatures [342, 345], whilst those adopting this structure at ambient temperature all transform to an $\alpha$-$\mathrm{YF}_3$-structured form (space group $P\bar{3}m1$ [346]) on heating [342]. Ionic conductivity measurements showed that the change from the $\beta$-$\mathrm{YF}_3$ to the $\alpha$-$\mathrm{YF}_3$ ionic arrangements in $\mathrm{YF}_3$ and $\mathrm{LuF}_3$ is associated with type-I superionic transitions [347], though the structural basis of the disorder within the high temperature phases has not been studied.

Recent attention has focused on the relationship between the ambient temperature $\beta$-$\mathrm{YF}_3$ and tysonite arrangements [345, 348]. As mentioned above, both structure types can be described as heavily distorted $ABX_3$ perovskites with all the $B$ sites empty and the $A$ ($Re^{3+}$) cations situated inside irregular trigonal prisms. In the $\beta$-$\mathrm{YF}_3$ arrangement additional anions are situated close to the three rectangular faces (resulting in a nine-fold co-ordination) whilst the tysonite structure has additional anions occupying sites close to all the faces of the distorted trigonal prisms (3 × rectangular and 2 × triangular), such that the anion environment surrounding the cations is closer to 11-fold co-ordination [345]. The increased co-ordination within the latter has been proposed to result in a rather weaker bonding between the cations and the more distant of the anions and explain the relatively higher ionic conductivities displayed by tysonite-structured compounds [348]. Of these, $\mathrm{LaF}_3$ has been the most widely studied but, unfortunately, the literature is confused by the use of subtly different models to describe its structure. Specifically, the $\mathrm{F}^-$ have been proposed to be distributed over two ($P6_3/mmc$ [349, 350]), three ($P\bar{3}c1$ [351–354]) or four ($P6_3cm$ [355]) symmetry independent sublattices. The sites are labelled from F1 up to F4, with the F1 sites identical in all three models. The F3 and F4 sites within the $P6_3cm$ description are equivalent (and labelled F3) in the $P\bar{3}c1$ structure. Similarly, the F2 and F3 sites of the latter form a single set labelled F2 in the simplest $P6_3/mmc$ model (see [355, 356]).

NMR studies initially favoured the $P6_3/mmc$ structural description for $\mathrm{LaF}_3$ and showed that $\mathrm{F}^-$ motion is restricted to hops between only the F1 sites at relatively low temperatures [357]. On heating, an increasing number of F1 $\leftrightarrow$ F2 hops between the two sublattices were observed, prior to the onset of free diffusion amongst all sites at $T > \approx 600$ K (see [357] and references therein). However, the validity of the $P6_3/mmc$ structural model has been questioned on geometric grounds [356] and subsequent NMR studies assuming the $P\bar{3}c1$ structural description have shown a higher activation energy for F1 $\leftrightarrow$ F2 hops over F1 $\leftrightarrow$ F3 ones [358]. Single crystal neutron diffraction data collected from $\mathrm{LaF}_3$ indicated that the $P\bar{3}c1$ model provides the correct structural description [353]. Interpretation of the strongly anharmonic thermal vibrations suggested that ionic conduction in the [001] direction occurs along channels of F3 sites, whilst diffusion within the (001) plane proceeds via F1 $\leftrightarrow$ F2 and F1 $\leftrightarrow$ F3 hops. As a consequence, all the anions are involved in the conduction process [353]. This model appears consistent with the similarity between the ionic conductivity of $\mathrm{LaF}_3$ measured parallel and perpendicular to [001] [359].

### 3.16. *A-site deficient perovskites:* $La_{2/3}TiO_3$, $La_{1/3}NbO_3$ *and* $WO_3$

Stoichiometric $AB\mathrm{O}_3$ oxide perovskites do not, in general, show significant cation migration. However, cation vacancies can be generated on the cuboctahedral $A$ sites by increasing the

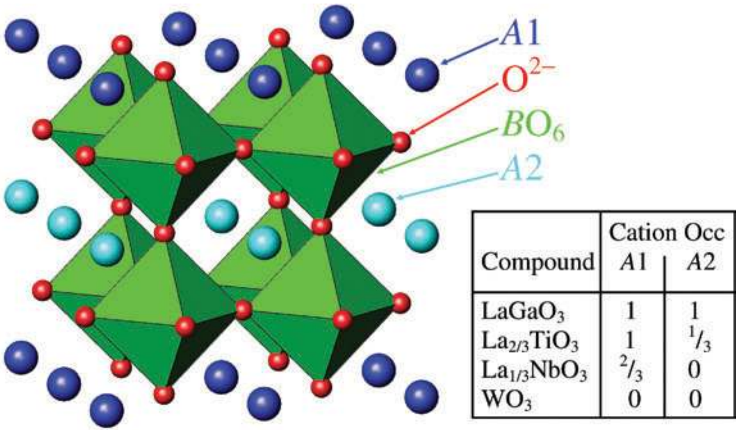

| Compound | Cation Occ A1 | Cation Occ A2 |
|---|---|---|
| $LaGaO_3$ | 1 | 1 |
| $La_{2/3}TiO_3$ | 1 | $^1/_3$ |
| $La_{1/3}NbO_3$ | $^2/_3$ | 0 |
| $WO_3$ | 0 | 0 |

**Figure 29.** Schematic diagram showing the distribution of cations over the *A* sites (labelled *A*1 and *A*2) within the perovskite structure to form the cation-deficient ionic arrangements typified by the compounds $La_{2/3}TiO_3$, $La_{1/3}NbO_3$ and $WO_3$ (for references, see section 3.16).

valence of the octahedral *B* cation species, i.e. $A^{3+}B^{3+}O_3 \rightarrow A^{3+}_{2/3}B^{4+}O_3 \rightarrow A^{3+}_{1/3}B^{5+}O_3 \rightarrow B^{6+}O_3$. This sequence is illustrated by, for example, the compounds $LaGaO_3 \rightarrow La_{2/3}TiO_3 \rightarrow La_{1/3}NbO_3 \rightarrow WO_3$. The distribution of cations within the perovskite-derived structures of the three *A*-site deficient compounds is illustrated schematically in figure 29, though, for clarity, the inevitable tiltings and distortions of the $BO_6$ octahedra are ignored (see [360], [361], [362], respectively). $La_{2/3}TiO_3$, $La_{1/3}NbO_3$ and $WO_3$ do not exhibit high values of ionic conductivity, but it is possible to introduce $Li^+$ onto the *A* site by chemical or electrochemical means. This process leads, for example, to the formation of the $Li_{3x}La_{2/3-x}TiO_3$ system [363–366], which has one of the highest values of $Li^+$-ion conductivity at room temperature ($\sigma_i = 1.53 \times 10^{-3}\ \Omega^{-1}\ cm^{-1}$ for $x = 0.12$ [367]). The exceptionally high ionic conductivity of $Li_{3x}La_{2/3-x}TiO_3$ makes it attractive for use in lightweight solid state batteries, though the possibility of $Ti^{4+} \rightarrow Ti^{3+}$ reduction as a consequence of the $Li^+$ intercalation or a slight oxygen deficiency (i.e. $Li_{3x}La_{2/3-x}TiO_{3-\delta}$) can contribute a significant detrimental electronic conductivity (for further details, see [368]). Related compounds formed by other trivalent rare-earth cations have also been studied but, in general, these possess lower ionic conductivities, probably because the lanthanide contraction reduces the size of the diffusion pathways through the lattice [364, 369].

The stability range of $Li_{3x}La_{2/3-x}TiO_3$ covers $\approx 0.06 < x < \approx 0.14$ [365, 370] and at temperatures in excess of ≈1425 K the material adopts a cubic perovskite arrangement with the $La^{3+}$, $Li^+$ and cation vacancies disordered over all the *A* sites [371, 372]. Whilst the stable form under ambient conditions is generally considered to adopt a structure close to that illustrated in figure 29 (space group *P*4/*mmm*, with $a = b \sim a_{perov}$ and $c \sim 2a_{perov}$ [370]), more complex orthorhombic descriptions also have been given [373, 374] and there are additional reports of metastable phases (see [372]). Within the idealized *P*4/*mmm* structure there are alternating La-rich and La-poor layers (figure 29). The $Li^+$ preferentially reside in the latter [373, 375], implying essentially two-dimensional conduction within these planes. NMR studies indicated that the $Li^+$ undergo hops both within the cuboctahedral cavity and between neighbouring *A* cages [373, 376], and bond valence methods (for details of the formalism, see [377]) predicted that the $Li^+$ occupy positions displaced from the centre of the $AO_{12}$ polyhedra and diffuse between nearest neighbour cuboctahedra in [100] and [010] directions [378].

Unfortunately, neutron diffraction studies could not unambiguously determine the favoured $Li^+$ positions [374] and this two-dimensional diffusion model is not supported by measurements of the ionic conductivity, which is essentially isotropic ($\sigma_i = 5.8 \times 10^{-4}\,\Omega^{-1}\,cm^{-1}$ and $6.8 \times 10^{-4}\,\Omega^{-1}\,cm^{-1}$ parallel and perpendicular to [001], respectively [379]).

The analogous system containing $B^{5+}$ cations, $Li_{3x}La_{1/3-x}NbO_3$, possesses an $A$-site deficient perovskite-structured phase for $0 < x < \approx 0.06$ [380, 381] and also forms a disordered cubic phase at high temperatures [382]. Its idealized structure at ambient temperature is similar to that of $Li_{3x}La_{2/3-x}TiO_3$, except that the 'La-rich' layers are $\frac{2}{3}$ occupied, the 'La-poor' ones are empty (figure 29) and it is best described using an orthorhombic unit cell of size $a \sim \sqrt{2}a_{perov}$, $b \sim \sqrt{2}a_{perov}$, $c \sim 2a_{perov}$ [361, 381, 383–385]. However, the ionic conductivity of the $Li_{3x}La_{1/3-x}NbO_3$ system ($\sigma_i = 4.3 \times 10^{-5}\,\Omega^{-1}\,cm^{-1}$ at 300 K for the $x = 0.04$ compound [381]) is somewhat lower than its $Ti^{4+}$ counterpart and, as a consequence, it has been less extensively studied.

$WO_3$ is the extreme example of an $A$-site deficient perovskite (figure 29) and its structural behaviour is very complex [362, 386–389]. According to the most recent reports [362, 386], six phase transitions occur on heating ($Pc$—230 K → $P\bar{1}$—300 K → $P2_1/n$—620 K → $Pbcn$—1000 K → $P2_1/c$—1070 K → $P4/ncc$—1170 K → $P4/nmm$), prior to melting at ≈1750 K. Interestingly, $WO_3$ does not form an ideal cubic-structured phase ($Pm\bar{3}m$) at elevated temperature, with all seven phases showing distortions of the high symmetry form [362, 386–389]. Ionically conducting phases can be produced by intercalation of $H^+$ or $Li^+$, though more interest has focused on the use of such compounds within thin film electrochromic devices ('smart windows'), due to the colour centres associated with the concomitant reduction of $W^{6+} \rightarrow W^{5+}$ [390]. In the case of $Li_xWO_3$, the addition of $Li^+$ gradually transforms the material from the ambient temperature monoclinic phase to a tetragonal-structured one over the range $0.01 \leqslant x \leqslant 0.082$ and then to a cubic-structured modification that is stable for $0.13 \leqslant x \leqslant 0.36$ [391]. Neutron diffraction studies of an $x = 0.36$ sample showed the latter to possess $Im\bar{3}$ symmetry [392], with the distortion of the perovskite-like network of corner-sharing $WO_6$ octahedra producing two crystallographically distinct $A$ sites. These are 12-fold and four-fold co-ordinated to anions and the $Li^+$ probably occupy the latter [392].

### 3.17. Double perovskites: cryolite-structured $Na_3AlF_6$

The elpasolite structure is derived from the perovskite arrangement by ordering of two different cation species over the $B$ sites, i.e. $2 \times ABX_3 \rightarrow A_2BB'X_6$. As illustrated in figure 30, the $BX_6$ and $B'X_6$ octahedra alternate along the three cubic $\langle 100 \rangle$ axes, so that the ideal elpasolite structure has $a \sim 2a_{perov}$ and adopts space group $Fm\bar{3}m$. In practice, the corner-sharing network of $BX_6$ and $B'X_6$ polyhedra undergoes co-operative tilts and distortions of the type seen in the parent perovskite-structured compounds, leading to a variety of lower symmetry derivatives and numerous temperature- and pressure-induced phase transitions [393–395]. Relatively little attention has been paid to possible thermally induced ionic disorder within elpasolite-structured compounds. However, if identical cations occupy the $A$ and $B'$ sites, such that the stoichiometry is $A_3BX_6$, the cryolite structure is formed. The most widely studied example of a superionic compound with this ionic arrangement is the mineral cryolite itself, which has the chemical composition $Na_3AlF_6$.

At ambient temperature, slight tilting and deformation of the $AlF_6$ octahedra lowers the symmetry of $Na_3AlF_6$ to $P2_1/n$ [396]. On heating, abrupt increases in the ionic conductivity were reported at 838 and 1153 K and the former attributed to a structural transition to the 'ideal' cubic modification [397, 398]. The latter was assigned to a type-I superionic transition characterized by extensive, dynamic $F^-$ disorder [399], based on the observation that the ionic

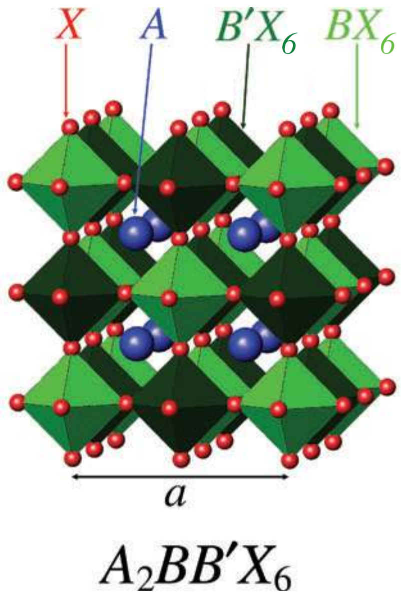

**Figure 30.** The elpasolite crystal structure of a compound of stoichiometry $A_2BB'X_6$ derived from the perovskite arrangement by alternating $BX_6$ and $B'X_6$ octahedra along the ⟨100⟩ directions. The cubic lattice parameter $a$ is illustrated.

conductivity of $Na_3AlF_6$ only increases by ∼10× on melting, compared to ∼7000× for NaF [399]. However, recent single crystal diffraction studies and $^{27}$Al, $^{23}$Na and $^{19}$F NMR studies have completely revised this picture [396]. The high temperature phase was shown to possess an orthorhombic distortion of the idealized cubic arrangement, with symmetry *Immm*. The $F^-$ undergo extensive anisotropic thermal vibrations as the $AlF_6$ octahedra perform extensive librations, but it is the $Na^+$ which become mobile [396]. NMR studies indicated that the high ionic conductivity is characterized by hopping of $Na^+$ between the six (octahedral $B$ site) and eight (distorted cuboctahedral $A$ site) co-ordinated environments [400]. Recent MD studies demonstrated that the $AlF_6$ octahedra rotate about the central $Al^{3+}$ at temperatures above 600 K, so that the structure can be viewed as an fcc array of spinning $AlF_6$ units, with all the octahedral and tetrahedral cavities filled with $Na^+$ [401]. The $AlF_6$ octahedra are isolated and there is no long-range migration of $F^-$, whilst the $Na^+$ diffusion proceeds via the formation of doubly occupied octahedral interstices [401].

The differing timescales for $AlF_6$ rotation and $Na^+$ diffusion within $Na_3AlF_6$ at elevated temperatures suggests that these two processes are unrelated [401]. This hypothesis is supported by studies of the chiolite-structured compound $Na_5Al_3F_{14}$, in which the sheets of $AlF_6$ octahedra are interlayered with edge-sharing $NaF_6$ octahedra [402]. This more rigid linkage appears to hinder large thermal motion of the $F^-$, though $^{23}$Na NMR studies show that extensive diffusion of $Na^+$ still occurs within $Na_5Al_3F_{14}$ [400]. However, the wider question of correlations between the ionic diffusion and the rotational motion of rigid polyhedra within such ‘rotator’ phases has proved to be a rather contentious one and will be revisited in section 4.12.

## 4. $\beta$-PbF$_2$: chemical and structural derivatives

This section begins by assessing the extent to which the Frenkel model of anion disorder described for $\beta$-PbF$_2$ in section 2.3 can be applied to other fluorite-structured halides and

**Table 3.** Summary of the superionic transition temperatures, $T_c$, and the melting temperatures, $T_m$, of various fluorite-structured halides and oxides and anti-fluorite-structured compounds (for references, see sections 2.3, 4.1, 4.10 and 4.11 and [24, 26]).

| Compound | $T_c$ (K) | $T_m$ (K) | $T_c/T_m$ |
|---|---|---|---|
| $CaF_2$ | 1430 | 1633 | 0.88 |
| $SrF_2$ | 1400 | 1723 | 0.81 |
| $BaF_2$ | 1275 | 1550 | 0.82 |
| $\beta$-$PbF_2$ | 711 | 1158 | 0.61 |
| $SrCl_2$ | 1001 | 1146 | 0.87 |
| $UO_2$ | 2610 | 3120 | 0.84 |
| $ThO_2$ | ~2950 | 3663 | ~0.81 |
| $Li_2O$ | ~1200 | 1705 | ~0.7 |
| $Na_2O$ | ~1240 | 1403 | ~0.9 |
| $Na_2S$ | ~1270 | 1442 | ~0.9 |
| $K_2S$ | 1050 | 1221 | 0.86 |

oxides. In an analogous manner to section 3, chemical derivatives of the parent binary compounds (including anion-excess and anion-deficient systems) will be considered, followed by a discussion of structurally related superionic compounds which can be derived by filling the various interstices within an fcc sublattice in different ways. Finally, the comparative merits of the fcc and hcp sublattices in promoting superionic behaviour will be assessed.

### *4.1. The concentration of Frenkel defects*

The fluorite-structured halides $SrF_2$, $CaF_2$, $BaF_2$ and $SrCl_2$ all undergo type-II superionic transitions when the temperature is increased (see table 3, [26, 67, 73] and references therein), and their macroscopic behaviour (ionic conductivity, specific heat, thermal expansion, etc) closely resembles that of $\beta$-$PbF_2$. At the ionic level, neutron diffraction studies indicated that the same dynamic Frenkel defect cluster model (figure 7) could also account for the coherent diffuse scattering observed from $CaF_2$ and $SrCl_2$ above $T_c$ (see figure 31), with minor differences in the extent of the outward relaxations of the surrounding anions consistent with the relative sizes of the ions [77]. From the experimental point-of-view, $SrCl_2$ is a particularly interesting example because the chlorine nucleus possesses a significant incoherent scattering cross-section for neutrons and the energy broadening of the incoherent (rather than coherent) diffuse scattering can be used to probe the geometry of the anion diffusion process[8]. Analysis of data collected at 1053 K using the Chudley-Elliott [404] and Wolf [405] encounter models showed that 73(5)% of $Cl^-$ hops occur between nearest neighbour anion positions in $\langle 100\rangle$ directions, with the remainder between next nearest neighbour sites in $\langle 110\rangle$ directions [406].

MD simulations of $\beta$-$PbF_2$ [79], $CaF_2$ [407–409] and $SrCl_2$ [410–412] reproduced the key experimentally observed features characteristic of the superionic state, including the preference for discrete hops between nearest neighbour anion sites in $\langle 100\rangle$ directions, the high anion diffusion coefficients and the absence of anions at the empty cube centre F4 positions (see figure 6) [413]. However, significant differences were reported concerning the extent of

---

[8] Formally, the coherent and incoherent contributions to the measured diffuse scattering are related by a double Fourier transform to the time-dependent total pair correlation function $G(\boldsymbol{r}, t)$ and the time-dependent self correlation function $G_S(\boldsymbol{r}, t)$, respectively. Given an ion at the origin at $t = 0$, $G(\boldsymbol{r}, t)\mathrm{d}\boldsymbol{r}$ gives the probability that *any* ion (including the same one) will be found within a volume $\mathrm{d}\boldsymbol{r}$ at time $t$, whilst $G_S(\boldsymbol{r}, t)\mathrm{d}\boldsymbol{r}$ gives the probability that the *same* ion will be found within a volume $\mathrm{d}\boldsymbol{r}$ at time $t$ (for a more detailed discussion, see [403]).

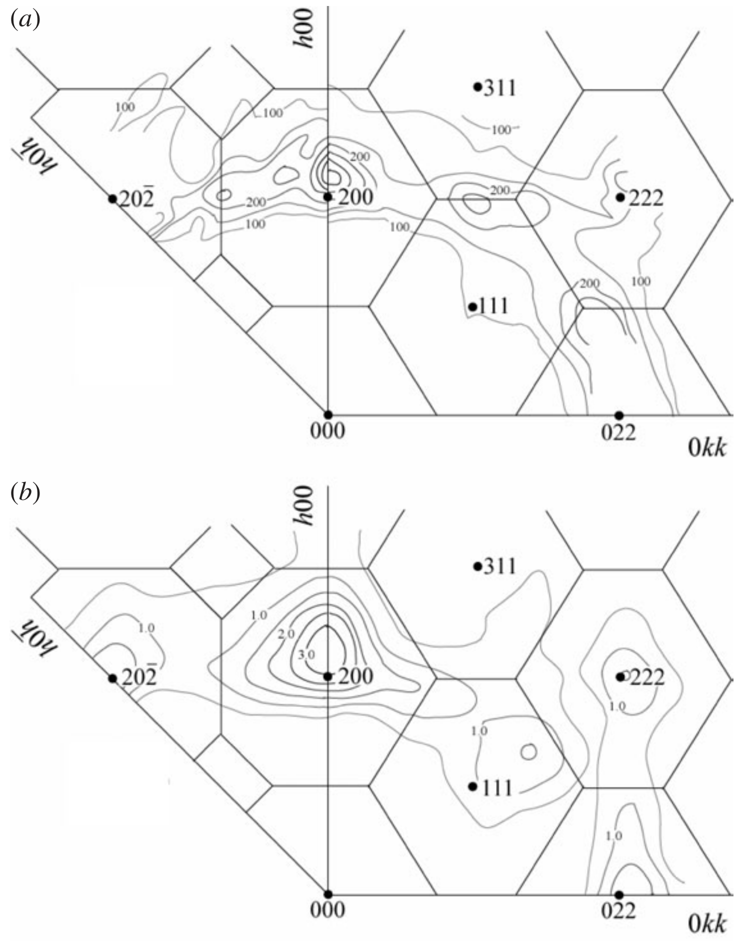

**Figure 31.** Comparison of (*a*) the measured distribution of neutron diffuse scattering from $CaF_2$ in the $(01\bar{1})$ and (010) planes of reciprocal space at 1473 K with (*b*) that calculated using a model of dynamic Frenkel defects of the type illustrated in figure 7 (after [77]).

anion disorder within the superionic phase, with values of $n \approx 0.02$ predicted by MD methods [79, 410] and $n \sim 0.3$–0.5 determined by neutron diffraction studies [76–78] at comparable temperatures. The absence of identifiable discrete defect clusters of the type illustrated in figure 7 within the MD studies (possibly due to the relatively small size of the simulation box) suggests that the apparent discrepancy may arise from differences in the interpretation of the structural behaviour of such highly disordered systems. Analysis of MD simulations typically gives the number of ion jumps, whilst diffraction experiments measure the total number of anions leaving their normal lattice sites. With reference to figure 7, the latter includes both 'true' Frenkel interstitials and those neighbouring ions merely relaxed off their regular lattice sites, whose relative populations differ by a factor dependent on the model of the defect cluster used to fit the data (i.e. by a factor of 3 or 9 for 3 : 1 : 2 and 9 : 1 : 8 clusters, respectively). This explanation was supported by calculations of the Bragg structure factors using the time-averaged ionic distribution simulated for $\beta$-$PbF_2$ at 991 K, which were then analysed using Frenkel defect models [79]. The resultant defect concentration of $n \approx 0.27$ was in broad agreement with that found experimentally ($n \approx 0.47$ at 973 K [76]) and considerably in excess of the value of $n \approx 0.02$ obtained by analysis of the anion hops within the simulated system.

### *4.2. The role of cation polarizability*

The MD simulations of the halide fluorites discussed in the previous subsection used the so-called 'rigid-ion' and 'shell' models to describe the interionic potentials [79, 407–412]. The latter includes harmonic springs coupling the ionic core to a massless shell, which mimic the effect of polarizability of the ions (for details, see [414]). In the case of $CaF_2$, the use of a shell model was found to have little impact on the simulated ionic motion, implying that polarization effects have minimal influence on the superionic behaviour [409]. However, the physical justification for the use of these types of interionic potentials has recently been questioned [80] and alternative formulations developed on an *ab initio* basis from electronic structure calculations. These incorporate, for example, the adaption of the size of the anion to its instantaneous environment [415] and demonstrate that cation polarizability is a rather important factor. For example, the number of anion defects in $CaF_2$ at 1400 K increases by a factor of around four with its inclusion [416]. In simple terms, this can be understood by noting that polarization lowers the energies of anions in lower symmetry environments (of the type experienced during hopping) relative to higher symmetry ones.

Such arguments are even more important for the case of $\beta$-$PbF_2$, because the $6s^2$ ground state of $Pb^{2+}$ leads to a greatly enlarged dipole polarizability [80, 416]. A recent MD study [80] demonstrated that cation polarization is essential to explain the lower superionic transition temperature of $\beta$-$PbF_2$, both in absolute ($T_c$) and relative ($T_c/T_m$) terms, compared to other fluorite-structured halides with comparably sized cations (such as $SrF_2$ and $BaF_2$, see table 3). Indeed, the simulations were also able to successfully reproduce the considerably lower fluorite to cotunnite transition pressure observed in $\beta$-$PbF_2$ (see figure 11) and differences in the measured phonon dispersion curves [80]. Clearly, the development of interionic potentials that include realistic representations of distinct physical effects such as ionic polarizability is essential to provide meaningful simulations of ionic diffusion processes. A recent example of the progress in this direction is given in the next subsection.

### *4.3. Ternary layered fluorite: $PbSnF_4$*

Intuitively, the addition of $Sn^{2+}$ to fluorite-structured $\beta$-$PbF_2$ does not appear to be a promising method to enhance its ionic conducting properties. Doping with isovalent cations does not introduce mobile charge-compensating anion vacancies or interstitials and the smaller size of $Sn^{2+}$ would be expected to lower $\sigma_i$ by reducing the size of the unit cell. Nevertheless, the ternary compound $PbSnF_4$ has one of the highest values of ionic conductivity at ambient temperature of any $F^-$ ion conductor ($\sigma_i \sim 10^{-3}\ \Omega^{-1}\ cm^{-1}$ [417]), which has led to potential applications within fast response oxygen gas sensors [418, 419].

$PbSnF_4$ adopts the cubic fluorite structure with a random arrangement of the $Pb^{2+}$ and $Sn^{2+}$ cations within its $\gamma$ phase (space group $Fm\bar{3}m$), which is stable in a narrow temperature range ($\approx$10 K) below its melting point of 663 K [417, 420]. However, the crystal chemistry of $PbSnF_4$ under ambient conditions is rather more complex, because several closely related phases are formed depending on the preparation method (see [421] and references therein). Most possess structures closely related to that of fluorite, but with cation ordering in the sequence PbPbSnSnPbPbSnSn... along one of the pseudocubic $\langle 100 \rangle$ axes, which causes major rearrangements of the anion sublattice [422–429]. In the $\alpha$-$PbSnF_4$ polymorph commonly

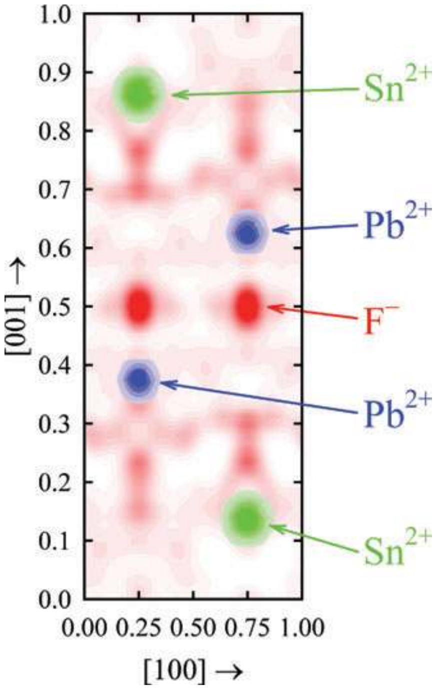

**Figure 32.** The time-averaged ionic density within the tetragonal unit cell of $\alpha$-$PbSnF_4$ at ambient temperature determined by powder neutron diffraction methods and projected down the [010] direction (after [430]). The PbPbSnSnPbPbSnSn... cation ordering sequence along the [001] axis is evident. The $F^-$ in the $Pb^{2+}$–$Pb^{2+}$ layers are localized close to the anion sites occupied within the equivalent fluorite-structured lattice, whilst the $Sn^{2+}$–$Sn^{2+}$ layers are essentially empty. The displaced anions are distributed in a highly disordered manner within the $Pb^{2+}$–$Sn^{2+}$ layers, implying that anisotropic $F^-$ conduction occurs predominantly within these (001) planes.

synthesized by solid state reaction of the constituent binary fluorides (space group $P4/nmm$ [427]) the $F^-$ between the two $Pb^{2+}$ layers lie close to the tetrahedrally co-ordinated sites occupied within the equivalent fluorite structure. In contrast, the $Sn^{2+}$–$Sn^{2+}$ layers have a low [427] or zero [424] population of anions. The displaced anions are located in the empty $F_8$ cubes between the $Pb^{2+}$ and $Sn^{2+}$ sheets (see figure 32 [430]). NMR studies of the isostructural compound $BaSnF_4$ (which is a somewhat poorer conductor, such that the timescales of fluorine motion lie within the accessible range of the technique) confirm that the $F^-$ located in the $Ba^{2+}$–$Ba^{2+}$ layers are immobile but those in the $Ba^{2+}$–$Sn^{2+}$ layers (and a few also in the $Sn^{2+}$–$Sn^{2+}$ layers) are in rapid exchange with one another leading to predominantly two-dimensional conduction [431, 432].

The dominant role of the $Sn^{2+}$ cations in stabilizing the layered structure adopted by $\alpha$-$PnSnF_4$ under ambient conditions has generally been attributed to their $5s^2$ electron lone-pairs. These point into the interlayer space between the two $Sn^{2+}$ sheets, creating cation-centred pseudo-octahedral $SnF_5E$ units (where $E$ represents the lone-pair). However, the time-averaged anion density and two-dimensional diffusion within $\alpha$-$PbSnF_4$ have recently been successfully reproduced within MD simulations, which essentially treat the 'lone-pairs' as an extreme manifestation of cation polarizability [401, 430]. As a consequence, the structural behaviour of $\alpha$-$PbSnF_4$ can be interpreted in terms of a higher 'effective' polarizability of the smaller $Sn^{2+}$ ion. The ability to derive realistic interionic potentials for highly polarizable cations conventionally described in terms of stereochemically active electron lone-pairs is clearly important to perform MD simulations of the numerous superionic compounds containing cations such as $Pb^{2+}$, $Sn^{2+}$ and $Bi^{3+}$ [9].

### 4.4. Cuboctahedral defects: $(K_{1-x}Bi_x)F_{1+2x}$ and $(Rb_{1-x}Bi_x)F_{1+2x}$

Another example of a highly polarizable cation species characterized by the presence of lone-pair electrons is provided by $Bi^{3+}$, which also readily stabilizes highly irregular local environments and is conducive to extensive anion disorder. This behaviour has already been demonstrated for the perovskite-related oxygen ion conductors within the $M$Bi$_3$O$_{5.5}$ and Bi$Me$VO$_x$ families (sections 3.13 and 3.14, respectively) and also underlies the impressive fluorine ion conductivity of $KBiF_4$ and $RbBiF_4$ [435]. The latter two compounds both adopt cubic fluorite-related structures with randomly arranged $K^+$/$Rb^+$ and $Bi^{3+}$ at ambient temperature. As such, they are isostructural to the high temperature $\gamma$-$PbSnF_4$ phase discussed in the previous subsection. These fluorite-structured phases were shown to be the $x = 0.5$ end-members of solid solutions $K_{1-x}Bi_xF_{1+2x}$ and $Rb_{1-x}Bi_xF_{1+2x}$, with approximate stability fields $0.50 \leqslant x < 0.70$ and $0.50 \leqslant x < 0.60$, respectively [436][10]. Intuitively, one might expect that increasing $x$ would enhance the ionic conductivity, since it increases both the proportion of the 'favourable' $Bi^{3+}$ cations *and* the population of the $F^-$ charge carriers. However, experimental studies showed that $\sigma_i$ decreases with $x$ within both the $K_{1-x}Bi_xF_{1+2x}$ and $Rb_{1-x}Bi_xF_{1+2x}$ series [436].

Powder neutron diffraction studies of $K_{1-x}Bi_xF_{1+2x}$ and $Rb_{1-x}Bi_xF_{1+2x}$ indicated that a significant fraction of the anions were located on interstitial F1 sites (see figure 6) rather than the regular lattice positions, even for the 'stoichiometric' $x = 0.5$ members [439]. The proportion of anions residing on these F1 sites increases with $x$ (from $\approx$25% at $x = 0.50$ to $\approx$39% at $x = 0.70$ in the case of $K_{1-x}Bi_xF_{1+2x}$ [439]) and was interpreted as the formation of $BiF_8$ square anti-prisms and larger cuboctahedral units (see figure 33). The former does not change the relative population of cationic and anions, whilst the latter is generated by the simultaneous conversion of six edge-sharing fluorite cubes into six corner-sharing square anti-prisms and accommodates four additional anions into the fluorite lattice [439]. $^{19}$F NMR measurements [440], EXAFS studies [441] and static energy calculations [442, 443] were all shown to be consistent with this structural model. Interestingly, the $x = 0.75$ compounds $KBi_3F_{10}$ and $RbBi_3F_{10}$ have relatively low ionic conductivities [436] and possess a regular array of cuboctahedral units coupled with long-range ordering of the two cation species (see figure 34, [444]). Thus, the reduction in the ionic conductivity with increasing $x$ appears to be a consequence of the trapping of the anions within these larger polyhedral units. Alternatively, MD studies of the $Rb_{1-x}Bi_xF_{1+2x}$ solid solution [441] suggested that $F^-$ diffusion occurs via the unoccupied F4 positions (see figure 6), and $\sigma_i$ is suppressed due to the reduction in the number of these 'empty cube' sites as the population of cuboctahedral polyhedra increases. However, this model for anion migration is not supported by diffraction studies [439].

---

[9] However, in this context, it is interesting to note that a new design strategy for materials with high oxygen-ion conductivity has recently been suggested, starting with a mixed oxide including a 'lone-pair' element of valence $m$ and replacing it with a 'non-lone-pair' element of approximately the same size and valence $m + 1$, so that every two substituted cations introduce one extra $O^{2-}$ (located in the space previously occupied by the lone-pair) and a vacancy [433, 434]. This process has been demonstrated by the synthesis of $La_2Mo_2O_9$, which is derived from the 'lone-pair' structure of $\beta$-$SnWO_4$ and has an ionic conductivity $\sigma_i = 6 \times 10^{-2}\ \Omega^{-1}\ \mathrm{cm}^{-1}$ at 1073 K [433].

[10] However, the fluorite-structured phases of both $KBiF_4$ and $RbBiF_4$ were subsequently shown to be metastable at ambient temperature, the stable forms being poorly conducting and possessing lower symmetry structures (see [437] and [438], respectively).

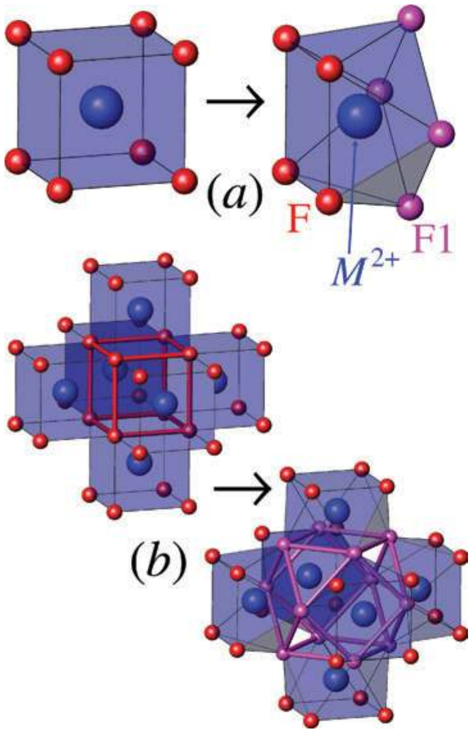

**Figure 33.** Schematic diagram showing (*a*) the conversion of an $MF_8$ cube into an $MF_8$ square anti-prism (such that half the anions are now located in F1 sites, see figure 6) and (*b*) the conversion of an assembly of six edge-sharing $MF_8$ cubes into one comprising six corner-sharing $MF_8$ square anti-prisms. The latter process converts the central cavity from an $F_8$ cube to an $F1_{12}$ cuboctahedron and replaces an $M_6F_{32}$ fragment of the fluorite lattice with one of composition $M_6F_{36}$ (or $M_6F_{37}$ if an additional anion is accommodated within the cuboctahedral cavity).

### 4.5. *Non-stoichiometric fluorites*

The formation of cuboctahedral structural units to accommodate high concentrations of excess anions within $KBi_3F_{10}$ and $RbBi_3F_{10}$ is just one example of the remarkable stability of the basic fluorite arrangement, even with gross deviations from the ideal $MX_2$ stoichiometry. Many attempts to synthesize non-stoichiometric derivatives of the binary $MX_2$ fluorites with improved ionic conductivities have been reported. A large proportion of these studies have focused on $\beta$-$PbF_2$, since it has the lowest value of the superionic transition temperature $T_c$ (table 3), and cover anion-deficient systems such as $(Pb_{1-x}K_x)F_{2-x}$ [82, 224–226] and numerous anion-excess examples including $(Pb_{1-x}Bi_x)F_{2+x}$ [226, 445–448], $(Pb_{1-x}Y_x)F_{2+x}$ [82, 225, 447, 449], $(Pb_{1-x}Al_x)F_{2+x}$ [450–452], $(Pb_{1-x}Th_x)F_{2+2x}$ [453, 454], $(Pb_{1-x}Zr_x)F_{2+2x}$ [455–457] and $(Pb_{1-x}Ta_x)F_{2+3x}$ [458]. Their structural properties are relatively complex and a thorough description of these studies (and those based on different host binary halides) is clearly beyond the scope of this review. However, a number of common features are observed.

In general, fluorite-structured solid solutions are formed at relatively modest dopant concentrations (typically $x < 0.2$–$0.3$). As implied by the brackets used to denote their chemical formulae, the aliovalent cations sit substitutionally on the host cation sites and overall charge neutrality is maintained by incorporating vacancies or interstitials within the

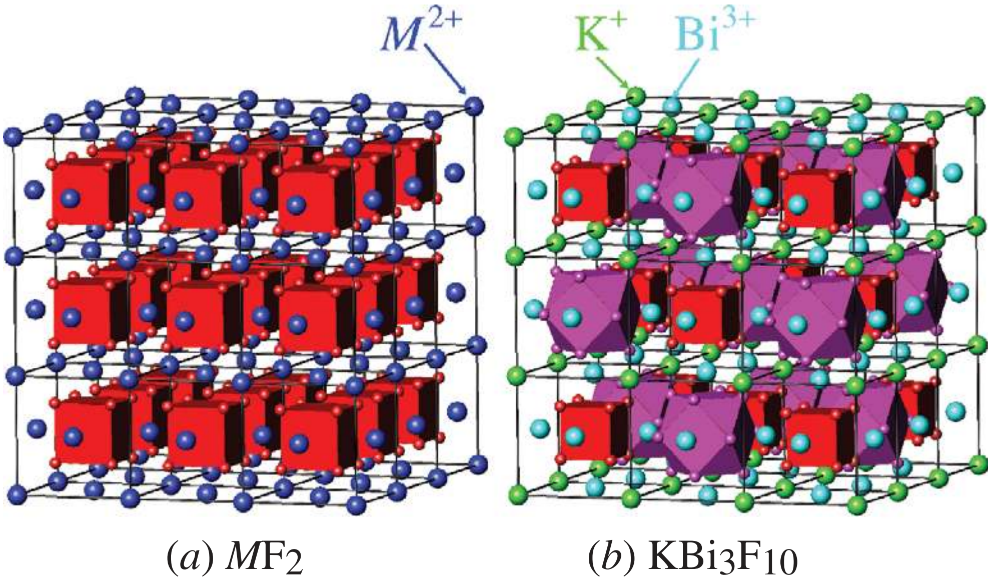

**Figure 34.** The crystal structures of (*a*) a fluorite-structured compound of stoichiometry $MF_2$ and (*b*) the compound $KBi_3F_{10}$ [444]. To illustrate their relationship, empty $F_8$ cubes and empty $F_{12}$ cuboctahedra are shown. As demonstrated in figure 33(*b*), the conversion of each cube into a cuboctahedron incorporates four additional anions into the lattice.

anion sublattice. These extrinsic defects are often responsible for a significant increase in the ionic conductivity with $x$ at temperatures close to ambient (see, e.g. figure 25). However, as the aliovalent cation content $x$ increases beyond $\sim 0.1$, $\sigma_i$ levels off and then, in many cases, falls (see, e.g. [65, 459, 460]). Following the discussion given in the previous subsection, the decrease in $\sigma_i$ with $x$ can be attributed to the formation of extrinsic defect clusters which trap potentially mobile anion vacancies and interstitials. The nature of these defects and their influence on the high temperature superionic behaviour has been the subject of much debate within the literature, with the two most widely studied anion-excess and anion-deficient systems being $(Ca_{1-x}Y_x)F_{2+x}$ and $(Zr_{1-x}Y_x)O_{2-x/2}$, respectively.

### 4.6. Anion-excess fluorite: $(Ca_{1-x}Y_x)F_{2+x}$

The stable defect cluster at low dopant concentrations ($x < \sim 0.01$) within anion-excess halide fluorites formed by the addition of trivalent cations comprises a substitutional $M^{3+}$ dopant and a charge compensating anion interstitial located in either the nearest neighbour or next nearest neighbour F4 site (see figure 6), depending on the relative sizes of the host and dopant cation species [461, 462]. Extensive diffraction studies of more heavily doped $CaF_2$, $BaF_2$, $PbF_2$ and $SrCl_2$ compounds (see, e.g. [65, 463] and references therein) have identified a number of crystallographic sites in which the charge compensating anion interstitials are accommodated, which essentially correspond to the F1, F2, F3 and F4 sites illustrated in figure 6.

In the specific case of $(Ca_{1-x}Y_x)F_{2+x}$, the earliest studies of samples with $0.06 \leqslant x \leqslant 0.32$ using neutron diffraction [464–466] concluded that the anions preferentially reside at the F1 and F2 positions. The mean occupancies of these two sites were comparable and consistent with defect clusters comprising a pair of F1 interstitials and outward relaxations of the two nearest neighbour lattice anions into F2 positions (see figure 35(*a*)). At higher values of

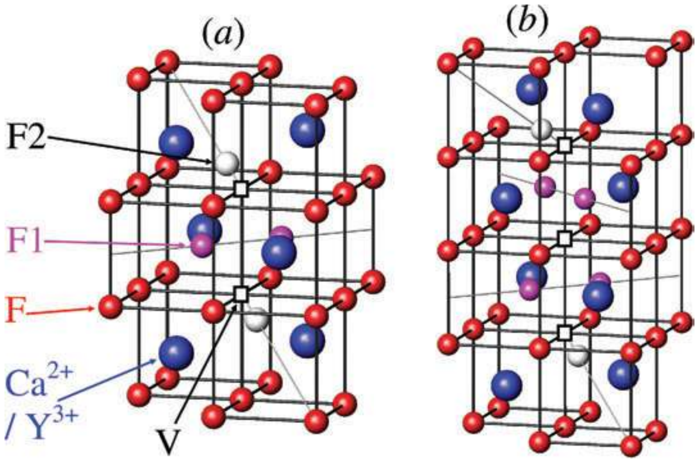

**Figure 35.** Extrinsic defect clusters proposed to accommodate additional $F^-$ within the anion-excess fluorite-structured compound $(Ca_{1-x}Y_x)F_{2+x}$ [465]. These are labelled (*a*) 2 : 2 : 2 and (*b*) 3 : 4 : 2, where the $v:i:r$ notation denotes the number of vacancies : interstitials : relaxed anions. The (charge compensating) interstitials reside in F1 sites and cause the two nearest neighbour anions to relax in ⟨111⟩ directions into F2 sites.

$x$ extended clusters (figure 35(*b*)) were also identified. In the notation used in section 2.3, these extrinsic defects are 2 : 2 : 2 and 3 : 4 : 2 clusters, respectively, and can be considered as static counterparts to the dynamic Frenkel 3 : 1 : 2 defects observed within the pure fluorites at temperatures above $T_c$ (see figure 7). However, the former contain anomalously short ($<2$ Å) contacts between the two F1 ions in the ⟨110⟩ directions and a re-analysis of the earlier data provided slightly different occupancies of the F1 and F2 positions [467]. A series of alternative defect clusters were then proposed, formed by the conversion of a cation-centred $(Ca,Y)F_8$ cube into a square anti-prism (see figure 33(*a*)), with between one and four interstitial anions located in F2 positions adjacent to the rotated face. However, a subsequent single crystal study [468] suggested that the apparent occupancy of the F2 sites is an artefact of the analysis procedure [469] and that a good fit to the experimental structure factors could be obtained with excess anions only occupying the F1 positions, provided that their thermal vibrations were treated as anisotropic. The most recent neutron diffraction study of the $(Ca_{1-x}Y_x)F_{2+x}$ system confirmed the absence of a measurable anion density at the F2 positions [463]. Instead, the $F^-$ were distributed over the F1 and F3 sites in the approximate ratio 1 : 2, which is consistent with the presence of cuboctahedral defects (figure 33(*b*)) with additional slight outward relaxations of the surrounding 24 lattice anions in ⟨111⟩ directions into the F3 positions. Detailed analysis of the coherent diffuse neutron scattering using the various defect cluster models [464–467] confirmed that the excess anions are predominantly accommodated within cuboctahedral clusters (see figure 36), which possibly contain an additional anion within the central cavity (an F4 site) [463].

Neutron diffraction [470–472] and EXAFS [473–475] studies have demonstrated that cuboctahedral defect clusters of the type found in $(Ca_{1-x}Y_x)F_{2+x}$ are a common feature within many anion-excess halide fluorites. Static energy calculations [476] have confirmed that their formation is preferable to other defect types, provided that the $M^{3+}$ dopant cations are relatively small. Similarities in the $^{19}F$ NMR spectra of $(Ca_{1-x}Y_x)F_{2+x}$ samples on increasing $x$ [477] are also consistent with the increasing concentration of excess anions being accommodated into the structure by an increasing number of cuboctahedral units. Their density eventually becomes

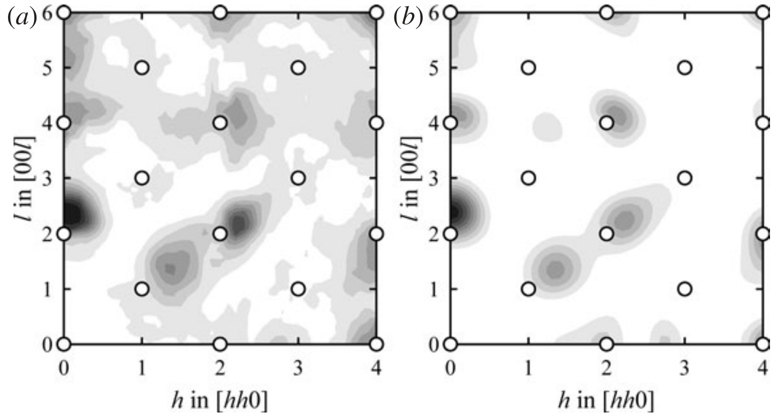

**Figure 36.** Comparison of (*a*) the measured distribution of the diffuse neutron scattering in the $(1\bar{1}0)$ plane of reciprocal space from $(\mathrm{Ca}_{1-x}\mathrm{Y}_x)\mathrm{F}_{2+x}$ with $x = 0.06$ at 293 K with (*b*) that calculated using a distribution of cuboctahedral defect clusters of the type shown in figure 33(*b*). The circles denote the positions of the Bragg peaks (after [463]). Copyright (1992), with permission from Elsevier.

sufficiently high that long-range ordering occurs and the material becomes poorly conducting. Indeed, the crystal structures of many ordered fluorite-related phases can be described as three-dimensional packings of cuboctahedral structural motifs, which also contain a central anion [478–480]. In the case of the $(\mathrm{Ca}_{1-x}\mathrm{Y}_x)\mathrm{F}_{2+x}$ system, the replacement of a $(\mathrm{Ca,Y})_6\mathrm{F}_{32}$ fluorite fragment by a $(\mathrm{Ca,Y})_6\mathrm{F}_{37}$ cuboctahedral unit generates a homologous series $\mathrm{Ca}_{m-5}\mathrm{Y}_5\mathrm{F}_{2m+5}$. The phases $\mathrm{Ca}_{14}\mathrm{Y}_5\mathrm{F}_{43}$ ($x = 0.263$) [481], $\mathrm{Ca}_2\mathrm{YF}_7$ ($x = 0.333$) [482], $\mathrm{Ca}_9\mathrm{Y}_5\mathrm{F}_{33}$ ($x = 0.357$) [482] and $\mathrm{Ca}_8\mathrm{Y}_5\mathrm{F}_{31}$ ($x = 0.385$) [482] have been reported, corresponding to the $m = 19$, 15, 14 and 13 members. However, full structural characterization has only been reported for the first compound, which occurs naturally as the mineral tveitite [481]. $(\mathrm{Ca,Y})_6\mathrm{F}_{37}$ cuboctahedral units are distributed along one of the $\langle 111 \rangle$ axes of the parent cubic structure, separated by relatively undistorted fragments of the fluorite lattice and leading to $R\bar{3}$ symmetry [481].

Whilst the structural properties of the $(\mathrm{Ca}_{1-x}\mathrm{Y}_x)\mathrm{F}_{2+x}$ system under ambient conditions are now largely understood, there is less certainty concerning the high temperature behaviour and, in particular, the interplay between the extrinsic (charge compensating) and intrinsic (thermally-induced) defects. The addition of trivalent cations such as $\mathrm{Y}^{3+}$ has been shown to increase the low temperature ionic conductivity of halide fluorite compounds [483] and to substantially depress the temperature at which the type-II superionic transition occurs [484, 485]. In the $(\mathrm{Ca}_{1-x}\mathrm{Y}_x)\mathrm{F}_{2+x}$ system, $T_c$ falls from 1430 K at $x = 0$ to $\approx$1200 K for $x = 0.09$ [484]. Single crystal neutron diffraction studies of an $x = 0.06$ sample showed a gradual increase in the occupancy of the F2 sites with increasing temperature and, at $T > \approx 1100$ K, the ratio of the occupancies of the F1 and F2 positions approaches the value 1 : 2. This is consistent with the break up of the cuboctahedral clusters, such that the excess anions are accommodated in dynamic defects whose structure is more closely related to the Frenkel clusters observed within the superionic phase of the undoped fluorites (figure 7(*a*)). This suggestion is supported by analysis of the coherent diffuse neutron scattering measured at 1173 K (see figure 37 [486]). Thus, at temperatures above $T_c$, both extrinsic and intrinsic clusters are present, which differ only by the presence of a charge compensating anion vacancy within the latter. Inevitably, the real situation is highly dynamic and more complex than this simple picture, though it is probable that both defect types contribute to the anion transport and give rise to the higher ionic conductivity observed in the doped system [484].

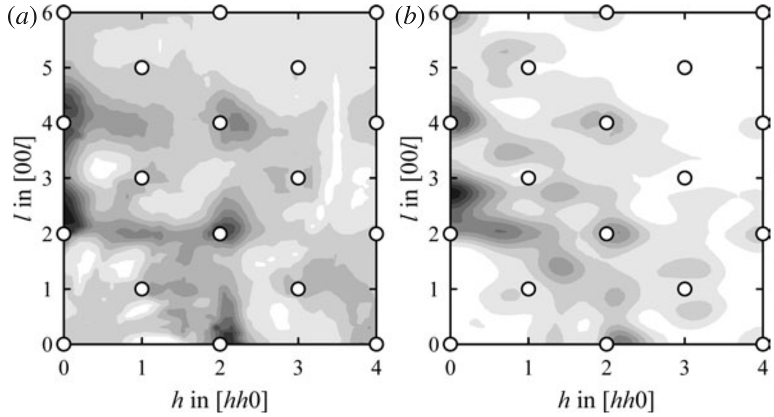

**Figure 37.** Comparison of (*a*) the measured distribution of the diffuse neutron scattering in the $(1\bar{1}0)$ plane of reciprocal space from $(\mathrm{Ca}_{1-x}\mathrm{Y}_x)\mathrm{F}_{2+x}$ with $x = 0.06$ at 1173 K with that calculated using a distribution of Frenkel type defects (see text). The circles denote the positions of the Bragg peaks (after [486]).

### 4.7. Anion-deficient fluorite: $(\mathrm{Zr}_{1-x}\mathrm{Y}_x)\mathrm{O}_{2-x/2}$

The binary oxide zirconia, $\mathrm{ZrO_2}$, only adopts the cubic fluorite structure within a relatively narrow temperature range immediately below its melting point ($\approx 2643\,\mathrm{K} < T < T_\mathrm{m} \approx 2988\,\mathrm{K}$ [487, 488]). Below ≈2643 K, this cubic phase ($c$-$\mathrm{ZrO_2}$) transforms to a tetragonal form ($t$-$\mathrm{ZrO_2}$, space group $P4_2/nmc$ [489]), in which alternate {110} planes of anions are displaced in opposite directions along the [001] axis by ≈0.3 Å. A further structural change occurs on cooling below ≈1370 K, such that the $\mathrm{Zr}^{4+}$ co-ordination shell becomes an irregular polyhedron of seven anions within the monoclinic baddelyite-structured phase ($m$-$\mathrm{ZrO_2}$, $P2_1/c$ [490]). It is well known that the addition of suitable divalent ($\mathrm{Ca}^{2+}$, $\mathrm{Mg}^{2+}$, etc) and trivalent ($\mathrm{Y}^{3+}$, $\mathrm{Sc}^{3+}$, $\mathrm{Nd}^{3+}$, etc) cation species can stabilize the two high temperature forms under ambient conditions (see, e.g. [491]). In these 'stabilized' tetragonal ($t^*$-$\mathrm{ZrO_2}$) and cubic ($c^*$-$\mathrm{ZrO_2}$) zirconias the dopant cations are located substitutionally on the $\mathrm{Zr}^{4+}$ sites and a fraction of the oxygen sites become empty to retain overall electrical neutrality. The presence of high concentrations of anion vacancies gives rise to impressive values of ionic conductivity at relatively modest temperatures. Coupled with their very low electronic conductivities, this makes stabilized zirconia ceramics highly attractive for technological applications within, for example, fuel cells and oxygen sensors [492].

Ionic conductivity measurements [493, 494] and quasi-elastic light scattering studies [495] have confirmed that the high ionic conductivity shown by stabilized zirconias at elevated temperatures is due to mobile $\mathrm{O}^{2-}$ vacancies. However, a simple picture of uncorrelated diffusion of anion vacancies through the crystal lattice cannot account for the variation of $\sigma_\mathrm{i}$ with dopant concentration $x$, which generally shows a maximum close to the lower limit of stability of the $c^*$ phase [496–498]. This observation has provided a challenge to theoretical attempts to model the microscopic diffusion mechanism using MC [499–501], MD [502–506] and other [507–513] methods. A simple model of a bound dopant cation–anion vacancy pair reproduced the peak in $\sigma_\mathrm{i}$, but its rapid decrease with increasing $x$ within the $c^*$ phase could only be reproduced by including a free energy-like function describing the ordering of $\mathrm{O}^{2-}$ vacancies by long-range defect–defect interactions [514]. Similarly, defect clusters formed by the aggregation of dopant cations have been shown to create deep traps that immobilize vacancies and give a qualitative agreement with the observed concentration dependence of

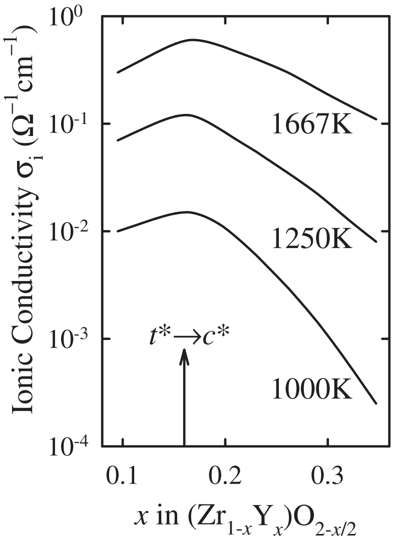

**Figure 38.** The variation of the ionic conductivity $\sigma_i$ of $(Zr_{1-x}Y_x)O_{2-x/2}$ with dopant concentration $x$ at three different temperatures. The maximum in $\sigma_i$ occurs close to the lower limit of stability of the stabilized cubic form ($c^*$) (schematic representation based on data published in [496, 497]).

$\sigma_i$ [507]. However, the precise structure(s) of the extrinsic defects present within stabilized zirconias have been the subject of numerous diffraction studies, especially in the case of $(Zr_{1-x}Y_x)O_{2-x/2}$.

The $m \rightarrow t^*$ and $t^* \rightarrow c^*$ transitions occur within the $(Zr_{1-x}Y_x)O_{2-x/2}$ system at $x \approx 0.05$ and $x \approx 0.16$, respectively, though there is a degree of co-existence between the neighbouring phases [487]. The latter coincides roughly with the maximum value of $\sigma_i$ (see figure 38 [496]). Electron [515–522], x-ray [523–528] and neutron [529–536] diffraction studies of the $c^*$-$(Zr_{1-x}Y_x)O_{2-x/2}$ phase have shown that significant fractions of both the anions and cations are displaced off their regular lattice sites. However, the detailed description of the local structure has proved controversial. For example, the observed diffuse x-ray scattering could be successfully simulated by allowing only the cations to move in $\langle 110 \rangle$ directions, with the extent of their individual relaxations depending on the proximity of oxygen vacancies [526]. Conversely, single crystal neutron diffraction studies showed that the anions are displaced from their lattice sites predominantly in $\langle 100 \rangle$ directions and, to a lesser extent, in $\langle 111 \rangle$ directions [535].

A recent comprehensive study of the structural properties of $c^*$-$(Zr_{1-x}Y_x)O_{2-x/2}$ as a function of both composition ($0.182 \leqslant x \leqslant 0.388$) and temperature ($293\,K \leqslant T \leqslant 2780\,K$) analysed the Bragg and coherent diffuse scattering from single crystals measured by both neutron and x-ray radiations, exploiting their increased sensitivity to the locations of the anions and cations, respectively [536]. As might be expected, the defect structure is rather complex. At lower $Y^{3+}$ concentrations ($x < \approx 0.26$) there are regions of the crystal typically $\sim 20$ Å in size, containing relatively few oxygen vacancies, in which the anion sublattice undergoes a slight tetragonal distortion of the type observed in the $t^*$ phase which is stable at lower $x$ values [530]. As $x$ increases, an increasing number of single vacancies and pairs of vacancies aligned along $\langle 111 \rangle$ directions appear. Both of these defect types are surrounded by relaxation fields characterized by displacements of the neighbouring anions in $\langle 100 \rangle$ directions towards the vacancies and nearest neighbour cations in $\langle 111 \rangle$ directions away from the vacancies (see figure 39). The cation-centred $\langle 111 \rangle$ vacancy pairs tend to pack together in $\langle 112 \rangle$ directions

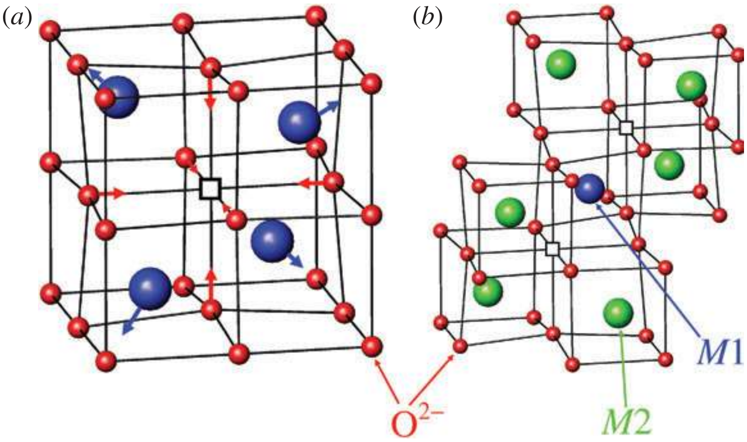

**Figure 39.** The defect structures observed within the $c^*$ phase of $(Zr_{1-x}Y_x)O_{2-x/2}$. These are (*a*) an isolated single vacancy with associated relaxations of nearest neighbour anions and cations and (*b*) a cation-centred vacancy pair along a $\langle 111 \rangle$ direction with relaxations of the surrounding anions and cations (after [536]). The latter pack together in $\langle 112 \rangle$ directions to form aggregates $\sim 15$ Å in size containing six- and seven-fold co-ordinated cation sites (labelled *M*1 and *M*2, respectively). Copyright (1999) by the American Physical Society.

to form aggregates $\sim 15$ Å in diameter. Measurements of the quasi-elastic energy broadening of the coherent diffuse scattering arising from each defect type showed these aggregates to be essentially static, even at very high temperatures close to the melting point [536]. In contrast, the isolated anion vacancies become mobile at $T > \sim 1000$ K (see figure 40) and are clearly responsible for the high macroscopic ionic conductivity. Using this structural model, the rapid decrease in $\sigma_i$ with increasing $x$ within the $c^*$ phase was attributed to a decrease in the mobility of the isolated vacancies, since both the number and size of the (static) aggregates increase with $x$ [536] such that they effectively block the diffusion pathways. This hypothesis is supported by observations of a maximum in the $O^{2-}$ diffusion coefficient at $x \approx 0.18$ [537] and by MD simulations [505].

The stability of the vacancy aggregate clusters within the $c^*$ phase of $(Zr_{1-x}Y_x)O_{2-x/2}$ at elevated temperatures contrasts with the behaviour of the extrinsic cuboctahedral clusters observed within the anion-excess fluorite $(Ca_{1-x}Y_x)F_{2+x}$ (see section 4.6), since the latter break up on heating and enhance, rather than hinder, the onset of high ionic conductivity. However, the tendency to form ordered compounds at higher values of $x$ via long-range packing of their respective defect units is a common feature to both systems. The ionic arrangement within the vacancy-pair aggregates observed within $c^*$-$(Zr_{1-x}Y_x)O_{2-x/2}$ closely resembles the structure of the compound $Zr_3Y_4O_{12}$ [538,539]. $Zr_3Y_4O_{12}$ is the only ordered intermediate phase in the $(Zr_{1-x}Y_x)O_{2-x/2}$ system and corresponds to $x = 0.571$ [488]. Its crystal structure is derived from the 'ideal' fluorite arrangement by ordering of the $\langle 111 \rangle$ vacancy pairs, lowering the symmetry from cubic to rhombohedral (space group $R\bar{3}$ [538]) and giving an effective stoichiometry of $M1M2_6O_{12}\square_2$ (where $\square$ denotes an anion vacancy). The cation sites *M*1 and *M*2 correspond to the six-fold and seven-fold co-ordinated positions within the defect aggregate, respectively (see figure 39(*b*)). Computer simulations of a variety of doped zirconia systems suggested that the anion vacancies are preferentially located close to whichever of the two cation species (host or dopant) is the smallest [510, 513]. Unfortunately, the relative similarity between the neutron and x-ray scattering powers of $Zr^{4+}$ and $Y^{3+}$ does not allow the distribution of the two cation species over the *M*1 and *M*2 sites to be established by diffraction methods

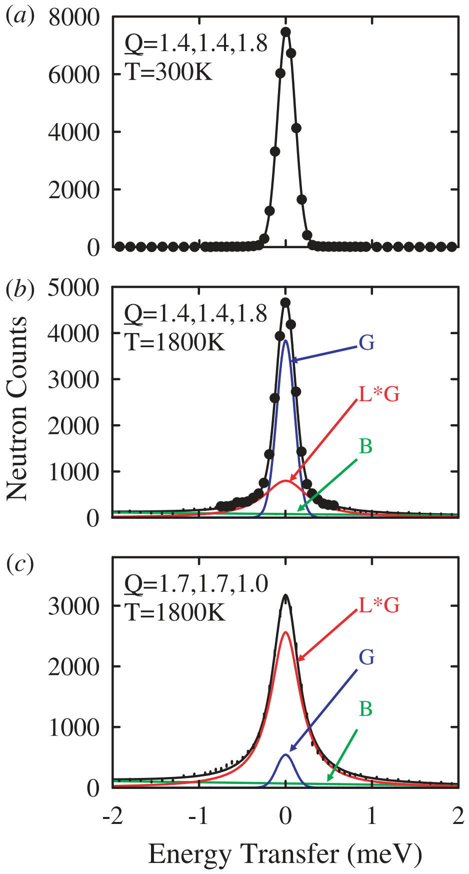

**Figure 40.** Quasi-elastic scans of the neutron energy transfer at constant scattering vector $\underline{Q}$ through the coherent diffuse scattering from a $(Zr_{1-x}Y_x)O_{2-x/2}$ sample with $x = 0.126(5)$ at the temperatures shown. The experimental data are fitted by a combination of an instrumental resolution limited Gaussian peak (G), a broadened Lorentzian component convolved with the Gaussian instrumental resolution function (L $*$ G) and a linear background contribution (B). The profile at $\underline{Q} = 1.4, 1.4, 1.8$ does not broaden significantly on increasing the temperature from (*a*) 300 K to (*b*) 1800 K, indicating that the aggregates of cation-centred vacancy pairs which give rise to the diffuse scattering at this $\underline{Q}$ position remain stable up to high temperatures. In contrast, (*c*) the diffuse scattering at $\underline{Q} = 1.7, 1.7, 1.0$ arises predominantly from isolated $O^{2-}$ vacancies and its significant quasi-elastic energy broadening clearly indicates that these defects are mobile and contribute to the macroscopically observed ionic conductivity (after [536]). Copyright (1999) by the American Physical Society.

[539]. In principle, the EXAFS technique can probe the individual co-ordination polyhedra surrounding each cation type, but the published studies provide opposing reports favouring preferential association of the vacancies with the host $Zr^{4+}$ [540, 541] and dopant $Y^{3+}$ [542] cations. Contradictory findings have also been reported on the basis of MD simulations (see [502, 503] and [505], respectively).

### *4.8. Pyrochlore-structured superionics: $Zr_2M_2O_7$ compounds*

The ionic conductivities of the stabilized $c^*$ phases formed by the addition of trivalent rare-earth cations ($Re^{3+}$) to $ZrO_2$ show similar behaviour to that discussed for $(Zr_{1-x}Y_x)O_{2-x/2}$

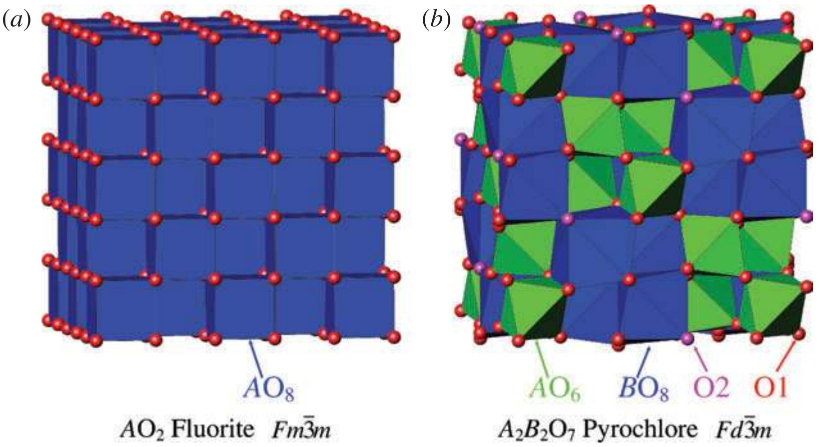

**Figure 41.** The relationship between the crystal structures of (*a*) a fluorite-structured oxide of stoichiometry $AO_2$ and (*b*) a pyrochlore-structured oxide of stoichiometry $A_2B_2O_7$. The former is converted into the latter by replacement of half the $AO_8$ cubes by $AO_6$ distorted octahedra. The two symmetry independent anion sites (O1 and O2) within the pyrochlore arrangement are illustrated.

in the previous subsection (see, e.g. [31, 491, 498]). However, fluorite-related phases of stoichiometry $Zr_3Re_4O_{12}$ ($x = \frac{4}{7}$) are only observed for smaller $Re^{3+}$ ions [543]. For $r_{Re^{3+}} > r_{Tb^{3+}}$ (which includes $Re^{3+} = Gd^{3+}$, $Sm^{3+}$, $Nd^{3+}$ and $Pr^{3+}$), increasing $x$ instead favours the formation of phases of composition $Zr_2Re_2O_7$ ($x = \frac{1}{2}$) with the cubic pyrochlore structure (space group $Fd\bar{3}m$) [544, 545]. The pyrochlore structure is a superstructure of the cubic fluorite arrangement with $a_{\text{Pyro}} = 2a_{\text{Fluorite}}$, so that the unit cell contains $16 \times Zr^{4+}$, $16 \times Re^{3+}$ and $56 \times O^{2-}$. The two cation species are ordered into rows in $\langle 110 \rangle$ directions. The 64 anion positions in the equivalent fluorite arrangement are described using $Fd\bar{3}m$ symmetry by a 48-fold set (labelled O1) plus two eight-fold sets (labelled O2 and O3)[11]. Both the O1 and O2 positions are fully occupied within an 'ideal' pyrochlore, whilst the O3 sites are completely empty. As a consequence, the O1 anions relax in $\langle 100 \rangle$ directions towards the vacant O3 sites, such that their positional parameter $x$ is typically less than $\frac{3}{8}$ [546]. The smaller $Zr^{4+}$ then sits at the centre of a distorted octahedron whilst the $Re^{3+}$ has a distorted cubic environment (see figure 41).

The relationship between the pyrochlore and fluorite crystal structures is analogous to that between the brownmillerite and perovskite arrangements (see figure 26 and section 3.13). This correspondence suggests that $Zr_2Re_2O_7$ compounds will adopt disordered anion-deficient cubic fluorite-structured phases at elevated temperatures. Whilst this behaviour is observed experimentally [547], many pyrochlore-structured oxides also exhibit high values of oxygen-ion conductivity at lower temperatures [548]. For example, $Zr_2Gd_2O_7$ has $\sigma_i \approx 8 \times 10^{-3}\ \Omega^{-1}\,\text{cm}^{-1}$ at 1000 K [549] but the transition to the disordered, anion-deficient fluorite-structured phase does not occur until ~1800 K [547]. X-ray diffraction studies of $Zr_2Gd_2O_7$ showed anisotropic thermal vibrations of the O1 anions towards the (empty) O3 positions, suggesting that this is the preferred diffusion route [550]. Static energy calculations [551, 552] and MD simulations [553] supported this model, though the latter found no evidence of $O^{2-}$ migration when the cation sublattice is completely ordered. Cation anti-site disorder (i.e. swapping of a small number of $Zr^{3+}$ and $Gd^{3+}$) favoured the onset of extensive anion diffusion via the formation of anion defects which comprise a pair of O1 vacancies in a $\langle 110\rangle$ direction and an interstitial close to the O3 sites but relaxed towards the vacancies [551, 554]. Static energy calculations for several pyrochlore-structured oxides have been reported, probing the anion diffusion mechanism [554], the degree of cation anti-site disorder [555], deviations from the ideal stoichiometry [556, 557] and extent of the relaxations of the O1 anions in $\langle 100\rangle$ directions [558] as a function of the radius ratio of the two cation species. Cation and anion disorder are both favoured when the sizes of the two ionic species are comparable [555], with relaxations of the anion sublattice lowering the energy differences between the two cation sites and between the three anion sites O1, O2 and O3. This tendency is illustrated by the doped system $(Zr_xTi_{1-x})_2Y_2O_7$, which shows a continuous transition from a fully ordered pyrochlore arrangement to a disordered fluorite-structured phase as $x$ increases and the (mean) radii of the two cation sites become more similar [559–561]. Particular attention has recently focused on the detailed relationship between the cation and anion disorder within such pyrochlore-related systems (see, e.g. [560, 562]), with the wider aim of developing optimum chemical doping strategies for materials to meet fuel cell applications [563].

---

[11] Within space group $Fd\bar{3}m$ the $Zr^{4+}$ and $Re^{3+}$ are located in the 16(*c*) sites at 0, 0, 0, etc and the 16(*d*) sites at $\frac{1}{2}, \frac{1}{2}, \frac{1}{2}$, etc, respectively. The oxygen positions within the equivalent fluorite-structured anion sublattice are located in the 48(*f*) sites at $x, \frac{1}{8}, \frac{1}{8}$, etc with $x = \frac{3}{8}$ (O1), the 8(*b*) sites at $\frac{3}{8}, \frac{3}{8}, \frac{3}{8}$, etc (O2) and the 8(*a*) sites at $\frac{1}{8}, \frac{1}{8}, \frac{1}{8}$, etc (O3).

### *4.9. Heavily defective fluorite: $Bi_2O_3$*

$Bi_2O_3$ is unique amongst the $M_2O_3$ sesquioxides because it undergoes a type-I superionic transition at ≈1000 K to a phase with a disordered cubic fluorite structure. However, this $\delta$-$Bi_2O_3$ phase differs from the high temperature $c$-$ZrO_2$ form (section 4.7) because it is grossly anion-deficient. The large concentration of intrinsic anion vacancies, coupled with the ability of the $Bi^{3+}$ cation to promote high anion conductivities (section 4.4), gives $\delta$-$Bi_2O_3$ an ionic conductivity between one and two orders of magnitude higher than stabilized $(Zr_{1-x}Y_x)O_{2-x/2}$ at comparable temperatures [564,565]. As a consequence, $Bi_2O_3$ and its chemical derivatives are very attractive candidates for fuel cell applications, though there are potential drawbacks due to the appearance of significant electronic conduction at low partial $O^{2-}$ pressures associated with the reduction of $Bi^{3+}$ [566].

A number of structural models to describe the distribution of anions within the superionic $\delta$-$Bi_2O_3$ phase have been proposed (see figure 42). The so-called 'Gattow' model (figure 42(*a*)) [567] assumes a completely random arrangement of $O^{2-}$ over the fluorite anion lattice sites, such that each has a mean occupancy of $\frac{3}{4}$. This model represents a time- and space-averaged picture reflecting the highly disordered nature of the anion sublattice and is clearly consistent with the exceptionally high ionic conductivity. In contrast, the 'Sillen' model (figure 42(*b*)) [568] proposed a degree of ordering within the anion sublattice, via the formation of pairs of $O^{2-}$ vacancies in $\langle 111\rangle$ directions of the type discussed for $c^*$-$(Zr_{1-x}Y_x)O_{2-x/2}$ in section 4.7. Early diffraction studies of $\delta$-$Bi_2O_3$ [569] were found to be inconsistent with both the 'Gattow' and 'Sillen' descriptions and favoured a 'Willis' model based on an average $\frac{3}{16}$ occupancy of four positions displaced from the lattice sites in $\langle 111\rangle$ directions [570][12]. However, the most recent neutron diffraction measurements indicated that the majority of anions remain on the regular fluorite lattice sites and only 43% are located on sites displaced in $\langle 111\rangle$ directions [571].

Unfortunately, theoretical calculations have reached conflicting conclusions concerning the preferred arrangement of anion vacancies within $\delta$-$Bi_2O_3$. Static simulations showed that

---

[12] These positions are close to the F3 sites illustrated in figure 6.

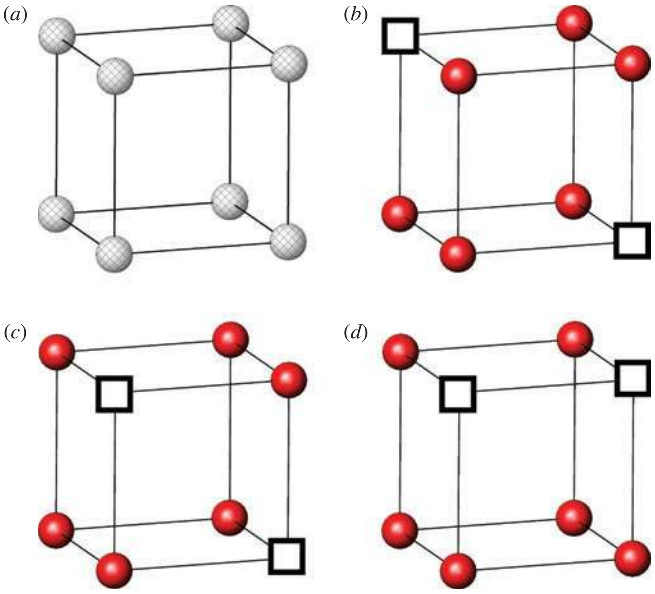

**Figure 42.** Schematic diagram of the structural models proposed to describe the oxygen sublattice of superionic $\delta$-$Bi_2O_3$. In (*a*) each lattice site has a time-averaged occupancy of $\frac{3}{4}$, whilst (*b*), (*c*) and (*d*) illustrate vacancy ordering in $\langle 111 \rangle$, $\langle 110 \rangle$ and $\langle 100 \rangle$ directions, respectively.

electrostatic considerations imply the formation of $\langle 111 \rangle$ vacancy pairs, though an additional small concentration of chains of $\langle 110 \rangle$ pairs (figure 42(*c*)) is also energetically favourable [572–575]. Within this model, charge transfer was proposed to occur via the addition and removal of $O^{2-}$ vacancies at opposite ends of a $\langle 110 \rangle$ chain. A subsequent first-principles calculation of the atomic and electronic structures of $\delta$-$Bi_2O_3$ confirmed the stability of $\langle 111 \rangle$ vacancy pairs [576], though a more recent study favoured the formation of pairs in $\langle 100 \rangle$ directions instead (figure 42(*d*)) [577]. Clearly, further work is required to determine the true structure of $\delta$-$Bi_2O_3$.

The high temperature cubic $\delta$ form of $Bi_2O_3$ can be formed under ambient conditions by the addition of various isovalent ($Y^{3+}$ and $Re^{3+}$, where $Re$ = rare-earth) and aliovalent ($Ba^{2+}$, $Nb^{5+}$) cations, in a manner analogous to the stabilized zirconias (section 4.7). However, $\sigma_i$ is significantly reduced by doping (for a recent review see [578]). In the $(Bi_{1-x}Y_x)_2O_3$ system, a study of the cubic phase with $0.25 < x < 0.42$ showed that the number of $\langle 111 \rangle$ displaced anions within the defect fluorite structure decreases with $x$ whilst the degree of short-range order between the anion vacancies increases [579]. These observations are consistent with the decrease in $\sigma_i$ with increasing $x$. The structural behaviour within systems containing other dopant cations (such as $Nb^{5+}$, $Ta^{5+}$, $Mo^{6+}$ and $W^{6+}$) is very complex, with the numerous fluorite-related phases often characterized by modulated structures (for a review of these issues, see [580]).

### *4.10. Oxide fluorites: superionicity in $UO_2$*

Whilst the cubic fluorite-structured phases of $ZrO_2$ and $Bi_2O_3$ can only be stabilized at ambient temperature by chemical doping methods, this is not the case for a number of stoichiometric binary oxides. These compounds, which include $PrO_2$, $CeO_2$, $ThO_2$, $UO_2$ and $PuO_2$, are

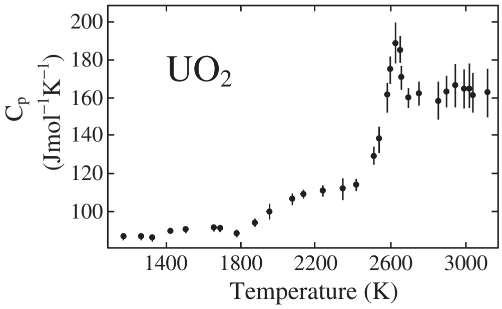

**Figure 43.** The specific heat $C_p(T)$ of UO$_2$ illustrating the anomalous peak observed at $T \approx 2610$ K (after [582]). Copyright (1985), with permission from Elsevier.

analogues of the fluorite-structured halides discussed in section 4.1, and it is natural to ask whether they also undergo type-II superionic transitions at elevated temperatures. However, the melting points of these oxides are considerably higher than their halide counterparts and, coupled with the absence of a suitable quadrivalent cation possessing a polarizability comparable to Pb$^{2+}$, implies that any superionic transition will occur at temperatures that are more difficult to access experimentally.

The presence of a high temperature superionic transition within uranium dioxide, UO$_2$, has been the subject of considerable debate within the literature, motivated by its use as a fuel for nuclear fission reactors. In the halide compounds, $T_c$ is typically $\sim 0.8T_m$ (table 3). For UO$_2$, which has $T_m = 3120$ K, a superionic transition might then be expected to occur at $T \sim 2500$ K. Although this is well in excess of normal reactor operating temperatures, a detailed knowledge of the thermophysical properties of UO$_2$ (and UO$_2$–PuO$_2$ solid solutions) is essential to optimize fuel performance [581]. Furthermore, the presence of an additional component in the heat capacity $C_p$ (due to the onset of any thermally induced Frenkel disorder) has important consequences when assessing the outcomes of possible reactor accident scenarios.

Indirect evidence for superionic behaviour within UO$_2$ was provided by measurements of its enthalpy by drop calorimetry methods and differentiation of these data with respect to temperature to obtain $C_p(T)$ [582, 583]. Despite rather large experimental uncertainties, a distinct peak was observed at $\approx$2610 K (figure 43) and shown to be consistent with the onset of anion Frenkel disorder [584, 585]. However, the band gap of UO$_2$ ($\sim$2 eV) is significantly lower than the formation energy for anion Frenkel defects ($\sim$5 eV) [586] and electronic disorder is likely to predominate, either in the form of direct semiconductor-like excitations of an electron to the conduction band or by the formation of small polarons (i.e. $2U^{4+}(5f^2) \leftrightarrow U^{5+}(5f^1) + U^{3+}(5f^3)$). These electronic effects were proposed to account for the observed maximum in $C_p(T)$, particularly if polarons involving other valence states such as U$^{2+}$ and U$^{6+}$ are also considered [587]. However, the case in favour of electronic transitions within UO$_2$ was weakened by the report of a jump in the enthalpy of the isostructural compound ThO$_2$ at $\approx$2950 K (corresponding to $T_c/T_m \approx 0.81$) [588]. Thorium has a completely empty 5$f$ shell and the relative stability of the Th$^{4+}$ valence state gives rise to a much higher formation energy for small polarons and excitations to the conduction band. Conclusive evidence for extensive lattice disorder within UO$_2$ (and ThO$_2$) was finally provided by neutron diffraction studies showing an increasing concentration of dynamic anion Frenkel defects, of the type illustrated in figure 7, at $T > \sim$2000 K [589, 590].

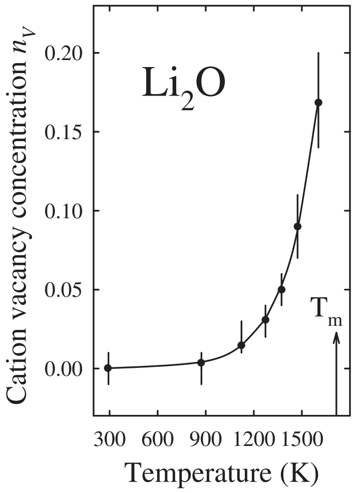

**Figure 44.** The temperature dependence of the cation vacancy concentration, $n_V$, within $Li_2O$ (after [596]). The melting temperature, $T_m$, is illustrated.

### *4.11. The effect of ionic size: anti-fluorite $Li_2O$*

The similarities between the observed superionic behaviour shown by the various fluorite-structured halides and oxides (sections 4.1 and 4.10, respectively) implies that the anion's charge plays a relatively minor role in promoting extensive lattice disorder. By studying anti-fluorite-structured oxides such as $Li_2O$, in which the positions of the anions and cations are reversed with respect to the fluorite crystal structure, it is possible to assess the influence of the mobile ion's size.

Lithium oxide, $Li_2O$, is a leading contender for use as a blanket breeding material in future nuclear fusion reactors [591, 592], its purpose being to convert energetic neutrons to usable heat, and breed the tritium necessary to sustain the D–T reaction ($^6_3\mathrm{Li} + ^1_0n \rightarrow ^4_2\mathrm{He} + ^3_1T$). The principal advantages of $Li_2O$ for this role lie in its relatively high melting temperature ($T_m = 1705$ K) and its impressive lithium density, which exceeds that of lithium metal by a factor of around two.

Experimental confirmation of a type-II superionic transition within anti-fluorite-structured $Li_2O$ analogous to that seen in the fluorite-structured compounds is made difficult by the extreme moisture sensitivity of the material, which readily absorbs water from the atmosphere to form LiOH. The measured conductivity of $Li_2O$ is rather sensitive to the LiOH content [593], though tentative evidence for the onset of a superionic transition at ≈1300 K was reported [594]. NMR and ionic conductivity measurements confirmed that $Li^+$ are the mobile species and showed that the electronic contribution to the measured conductivity is negligible [595]. Once again, single crystal neutron diffraction studies were required to characterize the nature of the thermally induced disorder and confirm the presence of a superionic transition with $T_c \approx 1200$ K [596]. The anti-fluorite crystal structure with anharmonic thermal vibrations of the $Li^+$ provided a good fit to the structure factors measured at temperatures up to ≈850 K, but an acceptable agreement could only be obtained at higher temperatures by including an increasing fraction of cation Frenkel defects of the 3 : 1 : 2 type observed within the superionic phase of the fluorite-structured compounds (figure 7(*a*)). The concentration of Frenkel defects within $Li_2O$ reaches $n = 0.17(3)$ at 1603 K (see figure 44) [596]. However, in comparison

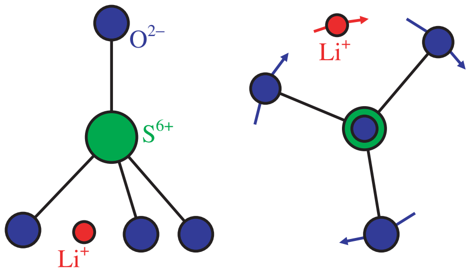

**Figure 45.** Schematic diagram illustrating the proposed 'paddle-wheel' mechanism of $Li^+$ ion migration within $\alpha$-$Li_2SO_4$ (after [607]). Copyright (1986), with permission from Elsevier.

with the fluorite-structured halides, the $Li^+$ interstitials are located much closer to the midpoint between nearest neighbour lattice cation sites, with only slight relaxations of the two nearest neighbour cations in $\langle 111\rangle$ directions [596]. This is consistent with the relative ionic sizes within the fluorite and anti-fluorite structures and the diffusion of the *smaller* of the two species within the latter.

Static energy calculations showed that cation Frenkel disorder is favoured over the formation of anion Frenkel defects or Schottky triplets within $Li_2O$ [594, 597]. However, these studies assumed that the interstitial cations occupy the empty cube centre sites (the F4 sites illustrated in figure 6). Further support for the cation Frenkel defect model was provided by the close agreement between the values of the formation energy for Frenkel clusters obtained from the neutron diffraction data for $n$ versus $T$ ($E_F = 2.1(3)$ eV [596]) and those obtained from conductivity measurements ($E_F = 2.53$ eV [594]) and computer simulations ($E_F = 2.12$ eV [594]). Subsequent MD simulations, using interionic potentials fitted to *ab initio* information describing the electron densities, successfully reproduced the key experimentally observed features, including the presence of a superionic transition (though at $T_c = 956(25)$ K), the absence of the $Li^+$ on the empty cube centre sites and the preference for $Li^+$ hops between nearest neighbour sites [598]. The latter is consistent with the analysis of incoherent quasi-elastic neutron scattering data, which showed that ~95% of $Li^+$ hops occur in $\langle 100\rangle$ directions [599].

### 4.12. *The 'paddle-wheel' and 'percolation' mechanisms in $\alpha$-$Li_2SO_4$*

At a temperature of 848 K lithium sulfate, $Li_2SO_4$, undergoes a type-I superionic transition to its $\alpha$ phase, which is characterized by extremely high values of ionic conductivity ($\sigma_i \sim 1$–$3\,\Omega^{-1}\,cm^{-1}$ [600]). The crystal structure of $\alpha$-$Li_2SO_4$ consists of isolated, rigid $SO_4^{2-}$ tetrahedra arranged as an fcc array and undergoing rapid rotation about the central $S^{6+}$. Within this sublattice the $Li^+$ predominantly (~90%) occupy the tetrahedrally co-ordinated sites [601, 602]. As a result, the time-averaged ionic arrangement is, to a good approximation, equivalent to that of anti-fluorite-structured $Li_2O$ if rotationally disordered $SO_4^{2-}$ polyanions replace the $O^{2-}$ ions. However, $Li_2SO_4$ shows a significantly higher ionic conductivity than $Li_2O$ at lower temperatures, implying that the $SO_4^{2-}$ units enhance the $Li^+$ diffusion via a 'paddle-wheel' mechanism. In this process, the rotating $SO_4^{2-}$ tetrahedron 'pushes' the $Li^+$ through the lattice in the manner illustrated in figure 45 (see [603] and references therein), which is consistent with the similarity between the experimentally determined activation energies for polyanion reorientation (0.40 eV) and cation diffusion (0.34 eV) [604]. MD studies supported the presence of correlations between the rotations of the $SO_4^{2-}$ units and diffusion of the $Li^+$ [605] and also indicated that the $Li^+$ partially occupy the octahedrally co-ordinated positions [606]. However, this 'paddle-wheel' mechanism predicts that the ionic conductivity of $Li_2SO_4$ would be reduced if it is doped with $Li_2WO_4$, because the heavier $WO_4^{2-}$ polyhedra would have a slower rotation [607]. In fact, experimental studies showed that the addition of ~10% $Li_2WO_4$ to $Li_2SO_4$ increased $\sigma_i$ by ~5× [607], leading to the development of a counter-argument based on a 'percolation model' in which the dominant factor in determining the ionic conductivity is the free volume available for $Li^+$ diffusion. Within this alternative description, the increase in $\sigma_i$ on doping results from the expansion of the lattice caused by the incorporation of the larger $WO_4^{2-}$ units [607].

The relative importance of the 'paddle-wheel' and 'percolation' models of ion transport within $\alpha$-$Li_2SO_4$ has been the subject of a vitriolic debate within the literature (see, e.g. [601, 603, 608–611] and [612–614], respectively), which has also been extended to other 'rotator' phases, including those in which the rotationally disordered polyanions form bcc and hcp sublattices (such as $LiNaSO_4$ [615] and $LiKSO_4$ [616], respectively). The high temperature $\alpha$ phase of $Na_3PO_4$ has also attracted recent attention, because the fcc sublattice of tetrahedral $PO_4^{3-}$ units are rotationally disordered about one of the $P^{5+}$–$O^{2-}$ bonds aligned along a cubic $\langle 100\rangle$ axis [617]. More importantly, the increased cation population is accommodated by filling all the *tet* and *oct* cavities with $Na^+$. This higher cation density makes the percolation model harder to visualize [618] but, nevertheless, the ionic conductivity of $\alpha$-$Na_3PO_4$ is still relatively high ($\sigma_i = 2.9 \times 10^{-2}\,\Omega^{-1}\,cm^{-1}$ at 873 K [619]). Neutron diffraction [615,620] and quasi-elastic scattering [618, 621] studies have been unable to unambiguously resolve the 'paddle-wheel' versus 'percolation model' debate, with the former study concluding that both mechanisms are probably operative [615]. Indeed, the distinction between the two effects is probably not clear-cut, since phase transitions to rotationally disordered phases are invariably accompanied by an increase in volume. Likewise, an increase in volume will favour the onset of rotational disorder [622].

### 4.13. Spinel-structured superionics: $Li_2MCl_4$ compounds

As discussed in the previous two subsections, the diffusing $Li^+$ within the anti-fluorite-structured superionic phases of $Li_2O$ and $Li_2SO_4$ predominantly occupy the *tet* sites within the fcc anion (or polyanion) sublattice, with only limited occupancy of the *oct* positions (figure 4). The cubic spinel-structured compounds considered in this subsection are also impressive $Li^+$ conductors [623, 624] ($\sigma \approx 0.3\,\Omega^{-1}\,cm^{-1}$ at ≈670 K for $Li_2CdCl_4$ [624]) but the cations are distributed over both the *oct* and *tet* positions.

There are eight formula units of stoichiometry $A_2BX_4$ within the cubic unit cell of the spinel structure (space group $Fd\bar{3}m$), so that the fcc-structured anion sublattice contains $32 \times X$ anions and generates 32 octahedrally and 64 tetrahedrally co-ordinated interstices. As illustrated in figure 46, the former comprise two 16-fold sets of sites (labelled *oct*1 and *oct*2) whilst the latter are formed by two eight-fold sets (*tet*1 and *tet*2) and a single 48-fold set (*tet*3)[13]. Filling all the *tet* positions with 64 cations would generate the anti-fluorite structure, but the stoichiometry of spinel-structured compounds provides only $16 \times A$ and $8 \times B$ cations. In a so-called 'normal' spinel, the $A$ cations reside in the *oct*2 sites and the $B$ cations are located in the *tet*1 positions,

---

[13] Within space group $Fd\bar{3}m$ the fcc sublattice of the spinel structure is formed by the 32($e$) sites at $x, x, x$, etc with $x = \frac{1}{4}$. The *oct*1 and *oct*2 positions are located in the 16($c$) sites at 0, 0, 0, etc and the 16($d$) sites at $\frac{1}{2}, \frac{1}{2}, \frac{1}{2}$, etc, respectively. The *tet*1, *tet*2 and *tet*3 positions are located in the 8($a$) sites at $\frac{1}{8}, \frac{1}{8}, \frac{1}{8}$, etc, the 8($b$) sites at $\frac{3}{8}, \frac{3}{8}, \frac{3}{8}$, etc and the 48($f$) sites at $x, \frac{1}{8}, \frac{1}{8}$, etc with $x = \frac{3}{8}$, respectively.

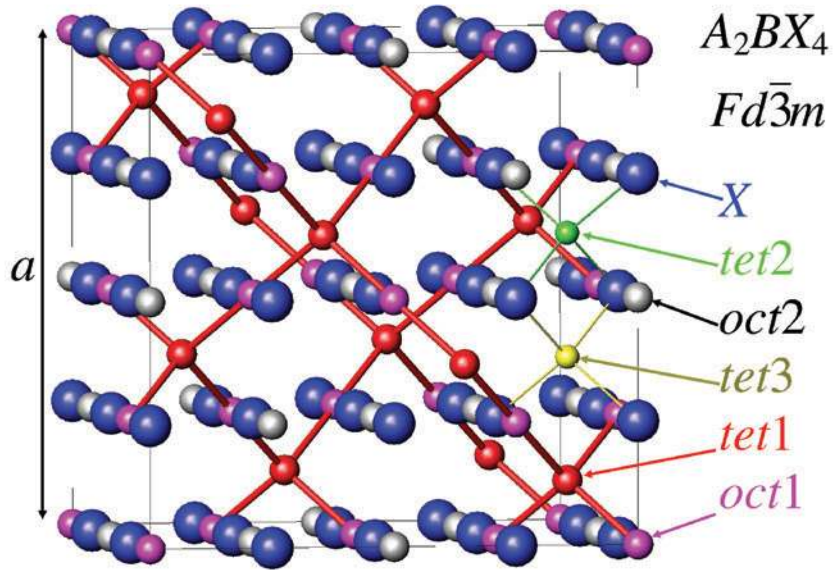

**Figure 46.** The ionic arrangement within a spinel-structured compound of stoichiometry $A_2BX_4$. In the ideal case, the $X$ ions form an fcc sublattice with the lattice parameter $a$ as illustrated. In a 'normal' spinel the $A$ and $B$ cations fill the *oct*2 and *tet*1 sites, respectively, whilst an 'inverse' spinel has half the $A$ cations filling the *tet*1 sites and the remainder, plus all the $B$ cations, filling the *oct*2 positions. In both cases the *oct*1, *tet*2 and *tet*3 sites are empty and, for clarity, only one representative example of the latter two sites are shown. The proposed *tet*1 → *oct*1 → *tet*1... conduction pathways are illustrated [626].

whilst 'inverse' spinels have half of the $16 \times A$ cations occupying the $8 \times$ *tet*1 positions, with the remaining $8 \times A$ cations and all the $B$ cations randomly distributed over the $16 \times$ *oct*2 sites. The *oct*1, *tet*2 and *tet*3 positions are empty in both 'normal' and 'inverse' spinels so that, overall, only $\frac{1}{2}$ of the octahedrally co-ordinated and $\frac{1}{8}$ of the tetrahedrally co-ordinated interstices contain cations. Clearly, the presence of so many unoccupied sites is potentially conducive to $Li^+$ diffusion.

Until relatively recently, it was believed that all the $Li_2MCl_4$ ($M$ = Mg, Mn, Ti, Cd, Cr, Co, Fe, V and Zn) compounds adopted the 'inverse' spinel structure, except for the $M$ = Zn one which is a 'normal' spinel (see [368] for references). The latter difference can be explained by the relatively small size of $Zn^{2+}$, which is more conducive to tetrahedral co-ordination than $Li^+$. The ionic conductivity of $Li_2ZnCl_4$ is relatively low (especially when compared to the other systems) with $\sigma_i \approx 2 \times 10^{-4}\ \Omega^{-1}\ \mathrm{cm}^{-1}$ at ≈550 K, probably due to the restricted conduction pathways for the octahedrally co-ordinated $Li^+$ [625]. For the 'inverse' spinels, increasing temperature favours a gradual transfer of those $Li^+$ at the *tet*1 positions to the empty *oct*1 sites, implying that the conduction pathways are *tet*1 → *oct*1 → *tet*1... as illustrated in figure 46 [626]. A recent $^6Li$ and $^7Li$ NMR investigation has supported this diffusion mechanism and suggested that the $Li^+$ on the *tet*1 sites within $Li_2MgCl_4$ are dynamically displaced in $\langle 111 \rangle$ directions (i.e. towards the *oct*1 positions) [627]. In many of the $Li_2MCl_4$ compounds, further heating favours transitions to disordered cation-deficient rocksalt-structured phases (space group $Fm\bar{3}m$ with $a \sim a_{\mathrm{spinel}}/2$) in which the $Li^+$ and $M^{2+}$ are randomly distributed over all the octahedrally co-ordinated sites, which are (on average) $\frac{3}{4}$ filled [628, 629].

Recently, the structures adopted by many of the $Li_2MCl_4$ compounds under ambient conditions have been revisited and several have been shown to possess distortions of the 'inverse' spinel structure [630]. Compounds with closely related stoichiometries have also been identified, including the ordered rocksalt-structured $Li_5CrCl_8$ [631] and the so-called 'Suzuki' phase $Li_6FeCl_8$ [632]. Despite the high values of ionic conductivity shown by many of these materials at relatively modest temperatures, their application within solid state batteries is limited by a relatively low decomposition potential of ≈1.1–1.3 V [633].

### 4.14. Lithium battery applications: $Li_xMn_2O_4$

Lightweight, high power density rechargeable batteries capable of operating at voltages greater than around 2 V are increasingly in demand for laptop computers, mobile phones and other portable electronic equipment. As a consequence, considerable research effort has been devoted to the quest for economically viable cells based on compounds that contain mobile $Li^+$ [28–30]. Of particular interest here is the spinel-structured compound $Li_xMn_2O_4$, which is a promising material owing to its wide stability range ($\approx 0 < x < \approx 2.25$) and low cost and toxicity when compared to existing compounds such as $LiCoO_2$ [634, 635]. Its use within battery applications has been described elsewhere [28, 29] and the discussion here is restricted to its structural properties.

$LiMn_2O_4$ adopts the 'normal' spinel structure (see section 4.13), with an average valence of $Mn^{3.5+}$ on the *oct*2 sites (see figure 46). The $Li^+$ are located in the *tet*1 sites and the surrounding tetrahedron of anions shares four common faces with empty *oct*1-centred octahedra [636]. Atomistic simulations [637] and $^7Li$ NMR studies [638] have confirmed that the three-dimensional network of *tet*1 → *oct*1 → *tet*1... sites forms the favoured migration route for $Li^+$, as it does in the 'inverse' spinel-structured halides discussed in the previous subsection. $Li^+$ is removed from and inserted into the cathode material during charge and discharge cycles of the battery, respectively, with a corresponding oxidation or reduction of the manganese ions. However, the $Mn_2O_4$ framework remains essentially intact during this process [636]. In the regime $0 < x < 1$, electrochemical cells based on spinel-structured $Li_xMn_2O_4$ operate at ≈4 V, with $Li^+$ gradually removed from the *tet*1 sites as the material tends towards completely delithiated $\lambda$-$MnO_2$ [639, 640]. As $x$ increases from $x = 1.0$, the cell voltage falls to ≈3 V but then remains essentially constant up to $x \approx 2.0$ [635]. In this region, $Li^+$ enters the empty *oct*1 sites and the $Li^+$ already present also tend to migrate from the *tet*1 to the *oct*1 positions [639]. This process eventually leads to the formation of a compound of composition $Li_2Mn_2O_4$ possessing an ordered rocksalt-like structure. The insertion of $Li^+$ causes an increase in the concentration of the Jahn–Teller active $Mn^{3+}$ ions, whose preference for a distorted local environment leads to a reduction in symmetry from cubic to tetragonal [636]. Over discharged $Li_xMn_2O_4$ with $x > \approx 2.2$ shows a drop in the open circuit voltage to ≈1.2 V, probably due to shearing of the fcc $O^{2-}$ sublattice towards hcp as the material tends towards the layered structure adopted by $Li_4Mn_2O_4$ ($Li_2MnO_2$) [641].

A major commercial limitation to the use of $LiMn_2O_4$-based cells is the loss of capacity after repeated charge–discharge cycles. A number of explanations for this behaviour have been proposed (for details, see [29, 642]). These include the detrimental effects of the Jahn–Teller distortions which occur when the average Mn charge approaches +3.5, because the severe tetragonal distortion ($c/a = 1.16$ [639]) damages the structural integrity of the material and degrades the contacts between neighbouring particles. Partial $Mn^{3+}/Mn^{4+}$ charge ordering also promotes a first-order structural phase transition within spinel-structured $LiMn_2O_4$ at temperatures just below ambient [643–645]. Introducing an excess of $Li^+$ (i.e. $Li_{1+x}Mn_{2-x}O_4$) reduces the transition temperature (from 282 K for $x = 0$ to 214 K for $x = 0.035$ [644]) and improves the rechargeable capacity [646]. However, there is increasing evidence that the $Li^+$ removal/insertion process involves complex microstructural changes, including ordering of the $Li^+$ [647, 648] and the formation of additional Li–Mn–O phases [649]. Such issues are increasingly being probed by *in situ* diffraction studies of electrochemical devices whilst they are charged/discharged within the x-ray [650, 651] or neutron [652] beam.

### *4.15. Superionics based on an hcp sublattice: the LISICONs*

Intuitively, the close structural similarity between the fcc and hcp lattices suggests that large families of highly conducting compounds will exist possessing hexagonal structures equivalent to the cubic fluorite, pyrochlore and spinel arrangements already discussed. However, as mentioned in section 3.3, the different stacking sequences of the two-dimensional close-packed layers generates pairs of tetrahedrally co-ordinated sites within the hcp lattice that are too close to be filled simultaneously (such as the *tet*1 and *tet*3 positions shown in figure 12). Since the occupancy of sites with tetrahedral environments is a common feature of most superionics, hcp-based ones are actually less common that their cubic analogues. Those that are observed are usually characterized by a somewhat lower concentration of mobile ions.

A large number of ternary and quarternary compounds with stoichiometries $ABO_2$, $A_3BO_4$ and $A_2BCO_4$ possess structures formed by filling the (available) tetrahedrally co-ordinated interstices within an hcp anion sublattice. The possible arrangements adopted by these so-called 'tetrahedral' structures have been reviewed elsewhere [653, 654]. The stoichiometries listed above all contain equal numbers of cations and anions and are derivatives of the binary hexagonal wurtzite structure (adopted by, e.g. $\beta$-AgI [37]). At relatively low temperatures, compounds such as $LiGaO_2$ and $Li_3PO_4$ adopt '$\beta$' phases in which the two cation species are ordered over the *tet* sites occupied within the wurtzite arrangement, such that the cation-centred tetrahedra share only corners (see figure 47). At elevated temperatures the cations typically occupy other tetrahedrally co-ordinated sites as well, so that edge-sharing (but not face-sharing) of the cation-centred tetrahedra occurs. The different tetrahedral linkages and cation ordering schemes generate numerous structure types, including the so-called $\gamma$-phases of $LiAlO_2$ and $Li_3PO_4$ [653].

The structure of $\gamma$-$Li_3PO_4$ (space group *Pnma*) contains edge-shared $LiO_4$ tetrahedra but only corner-sharing occurs between the $PO_4$ units. Together with the isostructural counterparts $Li_3VO_4$ and $Li_2ZnGeO_4$, it forms an important class of superionic material for high temperature battery applications (see [368]). The stoichiometric compounds possess relatively low ionic conductivities because the $Li^+$ are 'built' into the structure. However, aliovalent doping can dramatically enhance $\sigma_i$ to form, for example, $Li_{3+x}(P_{1-x}Si_x)O_4$, $Li_{3+x}(V_{1-x}Ge_x)O_4$ and $Li_{2+2x}Zn_{1-x}GeO_4$. These are the so-called lithium superionic conductors (LISICONs). For the reasons given above, the excess $Li^+$ cannot be accommodated on *tet* sites within the hcp anion sublattice without producing anomalously short cation–cation contacts. In the case of $Li_{2+2x}Zn_{1-x}GeO_4$, additional $Li^+$ have been proposed to occupy octahedrally co-ordinated interstitial sites [655, 656], though it has also been suggested that three $Li^+$ form a more complex defect cluster, which moves as a whole [657, 658].

### *4.16. The tetragonal-packed sublattice: $Li_4SiO_4$ and $Li_4GeO_4$*

A distortion of the hcp sublattice generates the so-called 'tetragonal-packed' (tp) array [659] and is a mechanism which allows additional cations to be accommodated on tetrahedrally co-ordinated sites. During the hcp → tp conversion the former's six-fold axis is lost but a new

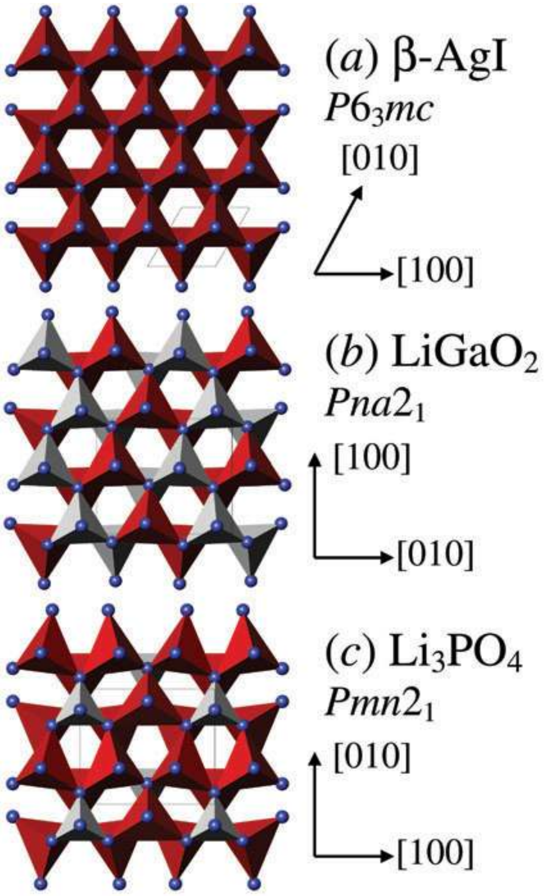

**Figure 47.** Comparison of the crystal structures of (*a*) $\beta$-AgI, (*b*) $LiGaO_2$ and (*c*) $Li_3PO_4$. The former comprises a network of corner-sharing $AgI_4$ tetrahedra. The structures of the latter two '$\beta$' phases are derived from the wurtzite structure by ordering of the $GaO_4$ ($PO_4$) tetrahedra and the $LiO_4$ tetrahedra. Their respective unit cells are shown as narrow lines.

four-fold axis is created, leading to a corrugated layer structure (see figure 48) with 11-fold rather than 12-fold co-ordination[14]. Half of the *tet* and *oct* sites within the hcp sublattice remain undistorted but the remainder are replaced by a larger number of sites with irregular octahedrally and tetrahedrally co-ordinated environments [660]. For each ion forming the tp sublattice it is possible to accommodate $\frac{5}{4}$ counterions on tetrahedrally co-ordinated sites without face-sharing of the tetrahedra, rather than the one possible within an hcp array. This process is illustrated by the crystal structures of $Li_4SiO_4$ and $Li_4GeO_4$ [660] in which the anion array approximates to tp. Whilst the tp array is not particularly 'open' (its highest packing density of 71.9% is only slightly less than the ideal hcp value of 74.1%), it does contain relatively large channels comprising sites with four-fold and six-fold co-ordination which are favourable for high cation mobility. This is especially advantageous for $Li^+$ which, owing to its small size, can be readily accommodated in the distorted tetrahedrally and octahedrally co-ordinated

---

[14] The ideal 11-fold co-ordinated tp structure has a tetragonal unit cell, with space group $P4_2/mnm$ and $c/a = 2/(2+\sqrt{2}) = 0.5858$. The lattice is formed by filling the 4(*f*) sites at $x, x, 0$, etc with $x = 1 - \sqrt{2}/2 = 0.2929$ [659]. The locations of the various interstices are given elsewhere [660].

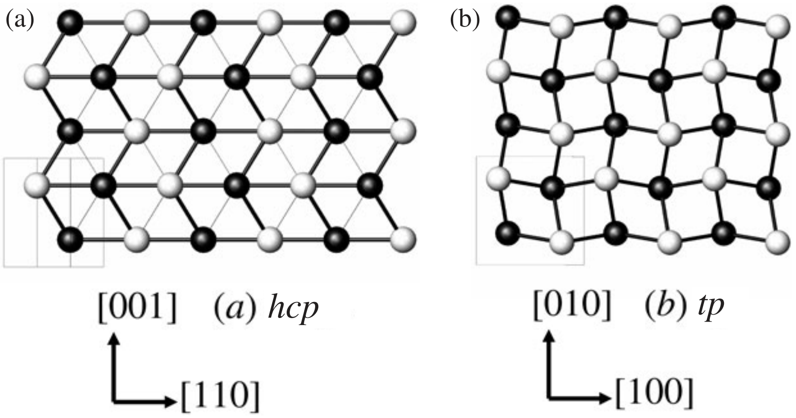

**Figure 48.** Schematic diagram showing the relationship between the arrangements of ions within (*a*) hexagonal close packed (hcp) and (*b*) tetragonal packed (tp) sublattices. The light and dark spheres represent ions at different heights and the unit cells are illustrated by the narrow lines (after [660]). Copyright (1982) the International Union of Crystallography.

environments. In the case of $Li_4SiO_4$, its modest room temperature ionic conductivity can be dramatically enhanced by aliovalent doping to generate $Li^+$ interstitials (i.e. $Li_{4+x}Si_{1-x}Al_xO_4$) or $Li^+$ vacancies (i.e. $Li_{4-3x}Ga_xSiO_4$) [661]. In the latter case, the highly complex nature of the $Li^+$ distribution has been determined by neutron diffraction methods [662].

## 5. Summary and conclusions

In his 1978 review [26], W Hayes described the status of the field of superionics as follows:

> '. . .it appears that attempts at generalization at the present time are stimulating rather than immediately useful and that progress requires very detailed study of individual systems.'

As illustrated in the previous sections, the intervening period has seen considerable advances in our knowledge of the structural and diffusional behaviour of many individual superionic compounds. Numerous theoretical and experimental techniques have contributed to this progress[15], but many of the key insights have been provided by neutron diffraction studies and MD simulations.

The neutron diffraction technique possesses a number of inherent advantages over its x-ray counterpart for studies of highly disordered systems [111]. Coupled with the construction of powerful new neutron sources and high count-rate diffractometers, high quality data can now be obtained relatively routinely from these notoriously difficult materials, even under extremes of pressure and/or temperature. In the past few years, major advances in the development of complementary data analysis procedures devoted to the study of disordered systems have been made, including the use of diffuse (or total) scattering data to probe the short-range correlations between disordered ions (with modelling techniques such as the RMC approach [50, 51]) and the application of maximum entropy methods to construct Fourier difference maps of the time-averaged density of mobile ions [161, 193, 674].

[15] A number of reviews describing the contributions made by various techniques to the study of superionic conductors have been published, including x-ray and neutron diffraction [50, 51, 663], quasi-elastic neutron scattering [112, 664], Brillouin scattering [665], light scattering [666, 667], NMR [668], ionic conductivity measurements [669, 670], EXAFS studies [671] and computer simulation methods [672, 673].

The increased availability of high power computer hardware has facilitated the growing use of MD simulations to probe the diffusion processes at the ionic level. However, their success is critically dependent on the development of reliable potentials to describe the interionic interactions. Whilst empirically determined potentials have proved very successful for studies of the superionic behaviour within many compounds (such as the RVP formalism used to investigate cation motion within many $Ag^+$ and $Cu^+$ conductors and described in sections 2.1 and 3.2), they tend to be specific to the particular phase being considered and not easily transferable to different phases of the same material or its chemical derivatives. Progress in this area clearly requires the development of *ab initio* interionic potentials incorporating many-body effects and based on electronic structure calculations [415, 675]. Significant progress has recently made, particularly in revealing the role of ionic polarizability in promoting extensive ionic disorder within compounds containing cations such as $Pb^{2+}$, $Sn^{2+}$ and $Bi^{3+}$ [80, 82, 109, 416, 462, 676]).

Taking a broader view of the field of superionic conductors, some progress has been made by both experimental [100,102,149] and computational [89,149] methods to reconcile the different superionic transition mechanisms within the $Ag^+$/$Cu^+$ conductors and the fluorite-structured compounds (see section 2). A number of experimental observations continue to be discussed with reference to the molten state, including anomalous features in the radial distribution functions of CuI [142] and observations of low frequency modes in $\beta$-$PbF_2$ [677]. However, the earliest structural description of superionics as ‘a liquid electrolyte poured into a crystalline cage’ has now largely been superseded by a model of mobile ions performing hops between discrete crystallographic sites. This approach is inherently oversimplistic, but has the advantage of providing an accessible description of the structural properties of most superionic compounds. Its value in describing the relationships between different systems has, hopefully, been demonstrated within the previous sections of this review. Nevertheless, it is clear that a consistent picture to describe the disordered structure of all superionic compounds is yet to emerge. There remains, for example, a need to rationalize the picture of the superionic state of the fluorite-structured compounds in terms of dynamic Frenkel clusters (section 2.3) with the correlated hopping mechanism used to describe the $Ag^+$ motion within $\alpha$-AgI (section 2.1).

The increasing demands for cheap, efficient and environmentally benign power sources for applications ranging from portable electronic devices to the new generation of ‘green’ electric vehicles will continue to provide a major incentive for the development of new materials with high ionic conductivities. Investigations of the behaviour of these compounds at the ionic level by both experimental and theoretical means will, of course, remain key to their understanding. The use of computational techniques to *predict* routes to new high conductivity phases remains a challenging goal and, for now, the quest for new materials to meet the expanding technological demands lies principally in the hands of solid state synthetic chemists.

## Acknowledgments

The author is extremely grateful to W Hayes and M T Hutchings for introducing him to the study of superionics during his post-doctoral research position at the Clarendon and Harwell Laboratories. It is also a pleasure to thank all those who have collaborated in various aspects of his work in this field, particularly P Berastegui, S G Eriksson, T W D Farley, J P Goff, M Hofmann, D A Keen, P A Madden and M Wilson, and to acknowledge the financial support provided by the UK Engineering and Physical Sciences Research Council (grants P:AK:113 C2 and GR/M38711). The author also thanks M T Hutchings, G J Hyland, D A Keen, R L McGreevy, S Miyatani, E A Secco, G Szabó and A R West for their kind permission to reproduce figures from their work in this review.

## References

[1] Hooton I E and Jacobs P W M 1988 *Can. J. Chem.* **66** 830–5
[2] Mohandas K S, Sanil N and Rodriguez P 2000 *Bull. Electrochem.* **16** 1–4
[3] Faraday M 1838 *Phil. Trans. R. Soc.* 90
[4] Derrington C E and O'Keeffe M 1973 *Nature Phys. Sci.* **246** 44–6
[5] Benz R 1975 *Z. Phys. Chem.* **95** 25–32
[6] Carr V M, Chadwick A V and Saghafian R 1978 *J. Phys. C: Solid State Phys.* **11** L637–41
[7] Tubandt C and Lorenz E 1914 *Z. Phys. Chem.* **87** 513–42
[8] Bernasconi J, Beyeler H U, Strässler S and Alexander S 1979 *Phys. Rev. Lett.* **42** 819–22
[9] Michiue Y and Watanabe M 1999 *Phys. Rev.* B **59** 11298–302
[10] Collin G, Boilot J P, Colomban P and Comes R 1986 *Phys. Rev.* B **34** 5838–49
[11] Collin G, Boilot J P and Comes R 1986 *Phys. Rev.* B **34** 5850–61
[12] Sata N, Eberman K, Eberl K and Maier J 2000 *Nature* **408** 946–9
[13] Liang J-J and Kung P W-C 2002 *J. Mater. Res.* **17** 1686–91
[14] Tuller H L 2000 *Solid State Ion.* **131** 143–57
[15] Schoonman J 2000 *Solid State Ion.* **135** 5–19
[16] Hayes W 1985 *Contemp. Phys.* **26** 421–41
[17] Bruce P G, Gray F M, Shi J and Vincent C A 1991 *Phil. Mag.* A **64** 1091–9
[18] Chandrasekhar V 1998 *Adv. Polym. Sci.* **135** 139–205
[19] Meyer W H 1998 *Adv. Mater.* **10** 439–48
[20] Ingram M D 1997 *Current Opinion Solid State Mater. Sci.* **2** 399–404
[21] Bunde A, Funke K and Ingram M D 1998 *Solid State Ion.* **105** 1–13
[22] Boolchand P and Bresser W J 2001 *Nature* **410** 1070–3
[23] Goodenough J B 1984 *Proc. R. Soc. Lond.* A **393** 215–36
[24] Boyce J B and Huberman B A 1979 *Phys. Rep.* **51** 189–265
[25] Chandra S 1981 *Superionic Solids: Principles and Applications* (Amsterdam: North-Holland)
[26] Hayes W 1978 *Contemp. Phys.* **19** 469–86
[27] Salomon M and Scrosati B 1996 *Gazetta Chim. Ital.* **126** 415–27
[28] Bruce P G 1996 *Phil. Trans. R. Soc. Lond.* A **354** 1577–94
[29] Bruce P G 1997 *Chem. Comm.* 1817–24
[30] Tarascon J-M and Armand M 2001 *Nature* **414** 359–67
[31] Minh N Q 1993 *J. Am. Ceram. Soc.* **76** 563–88
[32] Bonanos N, Knight K S and Ellis B 1995 *Solid State Ion.* **79** 161–70
[33] Kawada T and Yokohawa H 1997 *Key Eng. Mater.* **125–126** 187–248
[34] Carette L, Friedrich K A and Stimming U 2000 *Chem. Phys. Chem.* **1** 162–93
[35] Fergus J W 1997 *Sensors Actuators* B **42** 119–30
[36] Imanaka N and Adachi G 1997 *J. Alloys Compounds* **250** 492–500
[37] Burley G 1963 *J. Chem. Phys.* **38** 2807–12
[38] Wilsey R B 1921 *Phil. Mag.* **42** 262–3
[39] Jost W and Weiss K 1954 *Z. Phys. Chem. Neue Folge* **2** 112–14
[40] Strock L W 1934 *Z. Phys. Chem.* B **25** 441–59
[41] Strock L W 1936 *Z. Phys. Chem.* B **31** 132–6
[42] O'Keeffe M and Hyde B G 1976 *Phil. Mag.* **33** 219–24
[43] Hoshino S 1954 *J. Phys. Soc. Japan* **9** 295
[44] Bührer W and Hälg W 1974 *Helv. Phys. Acta* **47** 27–9
[45] Hoshino S, Sakuma T and Fujii Y 1977 *Solid State Commun.* **22** 763–5
[46] Wright A F and Fender B E F 1977 *J. Phys. C: Solid State Phys.* **10** 2261–7
[47] Cooper M J and Sakata M 1979 *Acta Crystallogr.* **A35** 989–91
[48] Tsuchiya Y, Tamaki S and Waseda Y 1979 *J. Phys. C: Solid State Phys.* **12** 5361–9
[49] Cava R J, Reidinger F and Wuensch B J 1977 *Solid State Commun.* **24** 411–16
[50] Nield V M and Keen D A 2000 *Diffuse Neutron Scattering from Crystalline Materials* (Oxford: Oxford University Press)
[51] McGreevy R L 2001 *J. Phys.: Condens. Matter* **13** R877–913
[52] Nield V M, Keen D A, Hayes W and McGreevy R L 1993 *Solid State Ion.* **66** 247–58
[53] Cava R J, Fleming R M and Rietman E A 1983 *Solid State Ion.* **9–10** 1347–52
[54] Keen D A, Nield V M and McGreevy R L 1994 *J. Appl. Cryst.* **27** 393–8
[55] Boyce J B, Hayes T M, Stutius W and Mikkelsen J C Jr 1977 *Phys. Rev. Lett.* **38** 1362–5

[56] Hayes T M, Boyce J B and Beeby J L 1978 *J. Phys. C: Solid State Phys.* **11** 2931–7

[57] Boyce J B, Hayes T M and Mikkelsen J C Jr 1981 *Phys. Rev.* B **23** 2876–96

[58] Schommers W 1977 *Phys. Rev. Lett.* **38** 1536–9

[59] Vashishta P and Rahman A 1978 *Phys. Rev. Lett.* **40** 1337–40

[60] Parrinello M, Rahman A and Vashishta P 1983 *Phys. Rev. Lett.* **50** 1073–6

[61] Nield V M and Hayes W 1995 *Defect Diffus. Forum* **125–126** 37–64

[62] Aniya M 1994 *Solid State Ion.* **70–71** 673–7

[63] Rakitin A and Kobayashi M 1996 *Phys. Rev.* B **53** 3088–94

[64] Kowada Y, Yamada Y, Tatsumisago M, Minami T and Adachi H 2000 *Solid State Ion.* **136–137** 393–7

[65] Réau J-M and Grannec J 1985 *Inorganic Solid Fluorides: Chemistry and Physics* ed P Hagenmuller (London: Academic) 423–67

[66] Shannon R D 1976 *Acta Crystallogr.* A **32** 751–67

[67] Derrington C E, Lindner A and O'Keeffe M 1975 *J. Solid State Chem.* **15** 171–4

[68] Catlow C R A and Norgett M J 1973 *J. Phys. C: Solid State Phys.* **6** 1325–39

[69] Hodby J W 1974 *Crystals with the Fluorite Structure* ed W Hayes (Oxford: Clarendon) pp 1–42

[70] Schröter W and Nölting J 1980 *J. Phys. Coll. C6* **41** 20–3

[71] Catlow C R A, Comins J D, Germano F A, Harley R T and Hayes W 1978 *J. Phys. C: Solid State Phys.* **11** 3197–212

[72] Dickens M H, Hayes W, Hutchings M T and Kleppmann W G 1979 *J. Phys. C: Solid State Phys.* **12** 17–25

[73] Chadwick A V 1983 *Solid State Ion.* **8** 209–20

[74] Shapiro S M and Reidinger F 1979 Physics of superionic conductors *Topics in Current Physics* vol 15, ed M B Salamon (Berlin: Springer) pp 45–75

[75] Koto K, Schulz H and Huggins R A 1980 *Solid State Ion.* **1** 355–65

[76] Dickens M H, Hayes W, Hutchings M T and Smith C 1982 *J. Phys. C: Solid State Phys.* **15** 4043–60

[77] Hutchings M T, Clausen K, Dickens M H, Hayes W, Kjems J K, Schnabel P G and Smith C 1984 *J. Phys. C: Solid State Phys.* **17** 3903–40

[78] Goff J P, Hayes W, Hull S and Hutchings M T 1991 *J. Phys.: Condens. Matter* **3** 3677–87

[79] Walker A B, Dixon M and Gillan M J 1982 *J. Phys. C: Solid State Phys.* **15** 4061–73

[80] Castiglione M J, Wilson M and Madden P A 1999 *J. Phys.: Condens. Matter* **11** 9009–24

[81] Zimmer F, Ballone P, Parrinello M and Maier J 2000 *Solid State Ion.* **127** 277–84

[82] Castiglione M J and Madden P A 2001 *J. Phys.: Condens. Matter* **13** 9963–83

[83] Wyckoff R W G 1982 *Crystal Structures* vol 1 (Malabar, Fl: Krieger)

[84] Lidiard A B 1974 *Crystals with the Fluorite Structure* ed W Hayes (Oxford: Clarendon) pp 101–84

[85] Gillan M J and Richardson D D 1979 *J. Phys. C: Solid State Phys.* **12** L61–5

[86] Catlow C R A and Hayes W 1982 *J. Phys. C: Solid State Phys.* **15** L9–13

[87] Roberts R B and White G K 1986 *J. Phys. C: Solid State Phys.* **19** 7167–72

[88] Dickman R 2001 *Phys. Rev.* E **64** 016124

[89] Hainovsky N and Maier J 1995 *Phys. Rev.* B **51** 15789–97

[90] Ishii T and Kamishima O 2001 *J. Phys. Soc. Japan* **70** 159–66

[91] Zimmer F, Ballone P, Maier J and Parrinello M 1997 *Ber. Bunsenges. Phys. Chem.* **101** 1333–8

[92] Zimmer F, Ballone P, Maier J and Parrinello M 2000 *J. Chem. Phys.* **112** 6416–23

[93] Mellander B E, Bowling J E and Baranowski B 1980 *Phys. Scr.* **22** 541–4

[94] Keen D A and Hull S 1993 *J. Phys.: Condens. Matter* **5** 23–32

[95] Wilson M and Madden P A 2002 *J. Phys.: Condens. Matter* **14** 4629–43

[96] Wilson M, Hutchinson F and Madden P A 2002 *Phys. Rev.* B **65** 094109

[97] Mellander B-E 1982 *Phys. Rev.* B **26** 5886–96

[98] Tallon J L 1988 *Phys. Rev.* B **38** 9069–79

[99] Rains C A, Ray J R and Vashishta P 1991 *Phys. Rev.* B **44** 9228–39

[100] Keen D A, Hull S, Hayes W and Gardner N J G 1996 *Phys. Rev. Lett.* **77** 4914–17

[101] Portella K F, Rattmann K R, de Souza G P, Garcia C M, Cantão M P and Muccillo R 2000 *J. Mater. Sci.* **35** 3263–8

[102] Hull S and Keen D A 1998 *Phys. Rev.* B **58** 14837–44

[103] Samara G A 1979 *J. Phys. Chem. Solids* **40** 509–22

[104] Klement W Jr 1976 *J. Phys. C: Solid State Phys.* **9** L333–5

[105] Klement W Jr and Cohen L H 1979 *J. Electrochem. Soc.* **126** 1403–5

[106] Melo F E A, Garrett K W, Mendes-Filho J and Moreira J E 1979 *Solid State Commun.* **31** 29–33

[107] Wang F and Grey C P 1995 *J. Am. Chem. Soc.* **117** 6637–8

[108] Wang F and Grey C P 1998 *J. Am. Chem. Soc.* **120** 970–80

[109] Castiglione M J, Wilson M, Madden P A and Grey C P 2001 *J. Phys.: Condens. Matter* **13** 51–66

[110] Schulz H 1982 *Ann. Rev. Mater. Sci.* **12** 351–76

[111] Wuensch B J 1993 *Mater. Sci. Eng.* B **18** 186–200

[112] Funke K 1991 *Phil. Mag.* A **64** 1025–103

[113] Funke K 1995 *Z. Phys. Chem.* **188** 243–57

[114] Funke K, Banhatti R D, Bruckner S, Cramer C, Krieger C, Mandanici A, Martiny C and Ross I 2002 *Phys. Chem. Chem. Phys.* **4** 3155–67

[115] Cava R J, Reidinger F and Wuensch B J 1981 *Solid State Ion.* **5** 501–4

[116] Oliveria M, McMullen R K and Wuensch B J 1988 *Solid State Ion.* **28–30** 1332–7

[117] Yamamoto K and Kashida S 1991 *Solid State Ion.* **48** 241–8

[118] Bougnot J, Guastavino F, Luquet H and Sodini D 1970 *Mater. Res. Bull.* **5** 763–8

[119] Asadov Y G, Rustamova L V, Gasimov G B, Jafarov K M and Babajev A G 1992 *Phase Transit.* **38** 247–59

[120] Yakshibaev R A, Mukhamadeeva N N and Almukhametov R F 1988 *Phys. Status Solidi* a **108** 135–41

[121] Vouroutzis N and Manolikas C 1989 *Phys. Status Solidi* a **111** 491–7

[122] Funke K, Lauxtermann T, Wilmer D and Bennington S M 1995 *Z. Naturf.* A **50** 509–20

[123] Nield V M, Keen D A, Hayes W and McGreevy R L 1992 *J. Phys.: Condens. Matter* **4** 6703–14

[124] Andreoni W and Tosi M P 1983 *Solid State Ion.* **11** 49–55

[125] Cain L S and Hu G 2001 *Phys. Rev.* B **64** 104104

[126] Altorfer F, Graneli B, Fischer P and Bührer W 1994 *J. Phys.: Condens. Matter* **6** 9949–62

[127] Keen D A and Hull S 1995 *J. Phys.: Condens. Matter* **7** 5793–804

[128] Chahid A and McGreevy R L 1998 *J. Phys.: Condens. Matter* **10** 2597–609

[129] Graneli B, Dahlborg U and Fischer P 1988 *Solid State Ion.* **28–30** 284–93

[130] Bührer W and Hälg W 1977 *Electrochem. Acta* **22** 701–4

[131] Nield V M, McGreevy R L, Keen D A and Hayes W 1994 *Physica* B **202** 159–66

[132] Phillips J C 1970 *Rev. Mod. Phys.* **42** 317–56

[133] Kikuchi H, Iyetome H and Hasegawa A 1998 *J. Phys.: Condens. Matter* **10** 11439–48

[134] Miyake S, Hoshino S and Takenaka T 1952 *J. Phys. Soc. Japan* **7** 19–24

[135] Keen D A and Hull S 1994 *J. Phys.: Condens. Matter* **6** 1637–44

[136] Krug J and Sieg L 1952 *Z. Naturf.* A **7** 369–71

[137] Zheng-Johansson J X M, Ebbsjö I and McGreevy R L 1995 *Solid State Ion.* **82** 115–22

[138] Zheng-Johansson J X M and McGreevy R L 1996 *Solid State Ion.* **83** 35–48

[139] McGreevy R L, Zheng-Johansson J X M and Ebbsjö I 1996 *Physica* B **226** 107–12

[140] McGreevy R L and Zheng-Johansson J X M 1997 *Solid State Ion.* **95** 215–20

[141] Ihata K and Okazaki H 1997 *J. Phys.: Condens. Matter* **9** 1477–92

[142] Trapananti A, di Cicco A and Minicucci M 2002 *Phys. Rev.* B **66** 014202

[143] Wagner J B and Wagner C J 1957 *J. Chem. Phys.* **26** 1597–601

[144] Boyce J B and Huberman B A 1977 *Solid State Commun.* **21** 31–5

[145] Burns G, Dacol F H and Shafer M W 1977 *Solid State Commun.* **24** 753–7

[146] Vashishta P and Rahman A 1979 *Fast Ion Transport in Solids* ed P Vashishta *et al* (New York: Elsevier/North-Holland) pp 527–33

[147] Salamon M B 1979 Physics of superionic conductors *Topics in Current Physics* vol 15, ed M B Salamon (Berlin: Springer) pp 175–99

[148] Hull S, Keen D A, Hayes W and Gardner N J G 1998 *J. Phys.: Condens. Matter* **10** 10941–54

[149] Keen D A, Hull S, Berastegui P, Barnes A C, Crichton W A, Madden P A, Tucker M G and Wilson M 2003 *Phys. Rev.* B **68** 014117

[150] Aniya M 1992 *Solid State Ion.* **50** 125–9

[151] Rapoport E and Pistorius C W F T 1968 *Phys. Rev.* **172** 838–47

[152] Hull S and Keen D A 1996 *J. Phys.: Condens. Matter* **8** 6191–8

[153] Sadanaga R and Sueno S 1967 *Miner. J. Japan* **5** 124–43

[154] Wiegers G A 1971 *Am. Miner.* **56** 1882–8

[155] van der Lee A and de Boer J L 1993 *Acta Crystallogr.* **C49** 1444–6

[156] Cava R J, Reidinger F and Wuensch B J 1980 *J. Solid State Chem.* **31** 69–80

[157] Cava R J and McWhan D B 1980 *Phys. Rev. Lett.* **45** 2046–50

[158] Grier B H, Shapiro S M and Cava R J 1984 *Phys. Rev.* B **29** 3810–14

[159] Schneider J and Schulz H 1993 *Z. Kristallogr.* **203** 1–15

[160] Keen D A and Hull S 1998 *J. Phys.: Condens. Matter* **10** 8217–34

[161] Hull S, Keen D A, Sivia D S, Madden P A and Wilson M 2002 *J. Phys.: Condens. Matter* **14** L9–17

[162] Vashishta P, Ebbsjö I, Dejus R and Sköld K 1985 *J. Phys. C: Solid State Phys.* **18** L291–6

[163] Ebbsjö I, Vashishta P, Dejus R and Sköld K 1987 *J. Phys. C: Solid State Phys.* **20** L441–7

[164] Rino J P, Hornos Y M M, Antonio G A, Ebbsjö I, Kalia R K and Vashishta P 1988 *J. Chem. Phys.* **89** 7542–55

[165] Tachibana F, Kobayashi M and Okazaki H 1988 *Solid State Ion.* **28–30** 41–5

[166] Rino J P, Hornos Y M M, Antonio G A, Ebbsjö I, Kalia R K and Vashishta P 1989 *Solid State Ion.* **32–33** 968–73

[167] Shimojo F and Okazaki H 1991 *J. Phys. Soc. Japan* **60** 3745–53

[168] Shimojo F and Okazaki H 1992 *J. Phys. Soc. Japan* **61** 4465–73

[169] Shimojo F and Okazaki H 1993 *J. Phys.: Condens. Matter* **5** 3405–16

[170] Kobayashi M 1990 *Solid State Ion.* **39** 121–49

[171] Miyatani S 1981 *J. Phys. Soc. Japan* **50** 3415–18

[172] Burley G 1967 *Acta Crystallogr.* **23** 1–5

[173] Szabó G 1986 *J. Phys. C: Solid State Phys.* **19** 3775–87

[174] Szabó G and Kertész J 1986 *J. Phys. C: Solid State Phys.* **19** L273–7

[175] O'Sullivan K, Chiarotti G and Madden P A 1991 *Phys. Rev.* B **43** 13536–48

[176] Madden P A, O'Sullivan K F and Chiarotti G 1992 *Phys. Rev.* B **45** 10206–12

[177] Seok C and Oxtoby D W 1997 *Phys. Rev.* B **56** 11485–92

[178] Seok C and Oxtoby D W 1998 *Phys. Rev.* B **58** 5146–8

[179] Tatsumisago M, Shinkuma Y and Minami T 1991 *Nature* **354** 217–18

[180] Saito T, Torata N, Tatsumisago M and Minami T 1995 *J. Phys. Chem.* **99** 10691–93

[181] Minami T, Saito T and Tatsumisago M 1996 *Solid State Ion.* **86–88** 415–20

[182] Hanaya M, Nakayama M, Oguni M, Tatsumisago M, Saito T and Minami T 1993 *Solid State Commun.* **87** 585–8

[183] Kusakabe M, Shirakawa Y, Tamaki S and Ito Y 1995 *J. Phys. Soc. Japan* **64** 170–6

[184] Shahi K and Wagner J B Jr 1981 *Phys. Rev.* B **23** 6417–21

[185] Bradley J N and Greene P D 1966 *Trans. Faraday Soc.* **62** 2069–75

[186] Bradley J N and Greene P D 1967 *Trans. Faraday Soc.* **63** 424–30

[187] Kanno R, Takeda K, Masuyama Y, Yamamoto O and Takahashi T 1983 *Solid State Ion.* **11** 221–6

[188] Yamamoto O 1993 *Fast-Ion Transport in Solids* (*NATO ASI Series* E) vol 250, ed B Scrosati *et al* (Dordrecht: Kluwer) pp 203–11

[189] Bradley J N and Greene P D 1967 *Trans. Faraday Soc.* **63** 2516–21

[190] Geller S 1967 *Science* **157** 310–12

[191] Kuhs W F 1983 *Acta Crystallogr.* A **39** 148–58

[192] Wilmer D, Funke K, Kloidt T and Carlile C J 1991 *Ber. Bunsenges. Phys. Chem.* **95** 1137–9

[193] Hull S, Keen D A, Sivia D S and Berastegui P 2002 *J. Solid State Chem.* **165** 363–71

[194] Owens B B, Patel B K, Skarstad P M and Warburton D L 1983 *Solid State Ion.* **9–10** 1241–6

[195] Owens B B and Bottelberghe J R 1993 *Solid State Ion.* **62** 243–9

[196] Geller S, Akridge J R and Wilber S A 1979 *Phys. Rev.* B **19** 5396–402

[197] Kanno R, Ohno K, Kawamoto Y, Takeda Y, Yamamoto O, Kamiyama T, Asano H, Izumi F and Kondo S 1993 *J. Solid State Chem.* **102** 79–92

[198] Andreoni W 1983 *Il Nuovo Cimento* **2D** 1664–1673

[199] Brightwell J W, Buckley C N, Miller L S and Ray B 1983 *Phys. Status Solidi* a **76** 391–8

[200] Brightwell J W, Buckley C N, Hollyoak R C and Ray B 1984 *J. Mater. Sci. Lett.* **3** 443–6

[201] Otsubo Y, Nitta A, Iwata Y and Ueki A 1966 *J. Chem. Soc. Japan: Indust. Chem.* **69** 1716–21

[202] Blachnik R and Stöter U 1989 *Thermochim. Acta* **145** 93–9

[203] Blachnik R and Stöter U 1987 *Thermochim. Acta* **112** 47–50

[204] Brightwell J W, Buckley C N and Ray B 1985 *Solid State Ion.* **15** 61–3

[205] Blachnik R and Stöter U 1989 *Thermochim. Acta* **141** 293–6

[206] Hull S, Keen D A and Berastegui P 2002 *J. Phys.: Condens. Matter* **14** 13579–96

[207] Hull S and Keen D A 2000 *J. Phys.: Condens. Matter* **12** 3751–65

[208] Hull S and Keen D A 2001 *J. Phys.: Condens. Matter* **13** 5597–610

[209] Hull S, Keen D A and Berastegui P 2002 *Solid State Ion.* **147** 97–106

[210] Armstrong R D, Bulmer R S and Dickinson T 1973 *J. Solid State Chem.* **8** 219–28

[211] Blachnik R and Dreisbach H A 1985 *J. Solid State Chem.* **60** 115–22

[212] Reuter B and Hardel K 1965 *Z. Anorg. Allg. Chem.* **340** 158–67

[213] Reuter B and Hardel K 1965 *Z. Anorg. Allg. Chem.* **340** 168–80

[214] Reuter B and Hardel K 1966 Ber. Bunsenges. **70** 82–6

[215] Perenthaler E and Schulz H 1981 *Solid State Ion.* **2** 43–6

[216] Didisheim J-J, McMullan R K and Wuensch B J 1986 *Solid State Ion.* **18–19** 1150–62

[217] Cho N, Kikkawa S, Kanamaru F and Yoshiasa A 1994 *Solid State Ion.* **68** 57–63

[218] Hull S, Keen D A, Gardner N J G and Hayes W 2001 *J. Phys.: Condens. Matter* **13** 2295–316

[219] Hoshino S, Sakuma T and Fujii Y 1979 *J. Phys. Soc. Japan* **47** 1252–9

[220] Matsunaga S 2003 *J. Phys. Soc. Japan* **72** 1396–402

[221] Hoshino S, Shapiro S M, Fujishita H and Sakuma T 1988 *J. Phys. Soc. Japan* **57** 4199–205

[222] Chiodelli G, Magistris A and Schiraldi A 1979 *Z. Phys. Chem. Neue Folge* **118** 177–86

[223] Mitchell R H 2002 *Perovskites. Modern and Ancient* (Ontario: Almaz)

[224] Hull S, Berastegui P, Eriksson S-G and Gardner N J G 1998 *J. Phys.: Condens. Matter* **10** 8429–46

[225] Liang C C and Joshi A V 1975 *J. Electrochem. Soc.* **122** 466–70

[226] Kennedy J H and Miles R C 1976 *J. Electrochem. Soc.* **123** 47–51

[227] Hull S and Berastegui P 1999 *J. Phys.: Condens. Matter* **11** 5257–72

[228] Hyde B G and Andersson S 1989 *Inorganic Crystal Structures* (New York: Wiley)

[229] Goldschmidt V M 1926 *Naturwissenschaften* **14** 477–85

[230] Woodward P M 1997 *Acta Crystallogr.* B **53** 44–66

[231] Woodward P M 1997 *Acta Crystallogr.* B **53** 32–43

[232] Berastegui P, Hull S and Eriksson S-G 2001 *J. Phys.: Condens. Matter* **13** 5077–88

[233] Keen D A and Hull S 2001 *J. Phys.: Condens. Matter* **13** L343–47

[234] Glazer A M 1972 *Acta Crystallogr.* B **28** 3384–92

[235] Howard C J and Stokes H T 1998 *Acta Crystallogr.* B **54** 782–9

[236] Wood I G, Knight K S, Price G D and Stuart J A 2002 *J. Appl. Cryst.* **35** 291–5

[237] Street J N, Wood I G, Knight K S and Price G D 1997 *J. Phys.: Condens. Matter* **9** L647–55

[238] Thomas N W 1996 *Acta Crystallogr.* B **52** 16–31

[239] O'Keeffe M and Bovin J-O 1979 *Science* **206** 599–600

[240] Cheeseman P A and Angell C A 1981 *Solid State Ion.* **5** 597–600

[241] Andersen N H, Kjems J K and Hayes W 1985 *Solid State Ion.* **17** 143–5

[242] Chadwick A V, Strange J H, Ranieri G A and Terenzi M 1983 *Solid State Ion.* **9–10** 555–8

[243] Zhou L X, Hardy J R and Cao H Z 1997 *Geophys. Res. Lett.* **24** 747–50

[244] Watson G W, Parker S C and Wall A 1992 *J. Phys.: Condens. Matter* **4** 2097–108

[245] Watson G W, Wall A and Parker S C 1995 *Phys. Earth Planet. Inter.* **89** 137–44

[246] Boyett R E, Ford M G and Cox P A 1995 *Solid State Ion.* **81** 61–8

[247] Poirier J P, Peyronneau J, Gesland J Y and Brebec G 1983 *Phys. Earth Planet. Inter.* **32** 273–87

[248] Ridou C, Rousseau M, Pernot B and Bouillot J 1986 *J. Phys. C: Solid State Phys.* **19** 4847–53

[249] Liu L-G and Bassett W A 1986 *Elements, Oxides and Silicates. High Pressure Phases with Implications for the Earth's Interior* (Oxford: Oxford University Press)

[250] Yagi T, Mao H-K and Bell P M 1978 *Phys. Chem. Miner.* **3** 97–110

[251] Cahn R W 1984 *Nature* **308** 493–4

[252] Achache J, le Mouel J L and Courtillot V 1981 *Geophys. J. R. Astron. Soc.* **65** 579–601

[253] Parkinson W D 1988 *Surv. Geophys.* **9** 235–43

[254] Li X and Jeanloz R 1991 *Nature* **350** 332–4

[255] Li X and Jeanloz R 1990 *J. Geophys. Res.* **95** 5067–78

[256] Matsui M and Price G D 1991 *Nature* **351** 735–7

[257] Kapusta B and Guillope M 1988 *Phil. Mag.* A **58** 809–16

[258] Wall A and Price G D 1989 *Phys. Earth Planet. Inter.* **58** 192–204

[259] Chaplot S L, Choudhury N and Rao K R 1998 *Am. Miner.* **83** 937–41

[260] Wentzcovitch R M, Martins J L and Price G D 1993 *Phys. Rev. Lett.* **70** 3947–50

[261] Fiquet G, Dewaele A, Andrault D, Kunz M and le Bihan T 2000 *Geophys. Res. Lett.* **27** 21–4

[262] Shim S-H, Duffy T S and Shen G 2001 *Science* **293** 2437–40

[263] Kilner J A and Brook R J 1982 *Solid State Ion.* **6** 237–52

[264] Shlichta P J 1988 *Solid State Ion.* **28–30** 480–7

[265] Cook R L and Sammells A F 1991 *Solid State Ion.* **45** 311–21

[266] Sammells A F, Cook R L, White J H, Osborne J J and MacDuff R C 1992 *Solid State Ion.* **52** 111–23

[267] Nomura K and Tanase S 1997 *Solid State Ion.* **98** 229–36

[268] Hayashi H, Inaba H, Matsuyama M, Lan N G, Dokiya M and Tagawa H 1999 *Solid State Ion.* **122** 1–15

[269] Boivin J-C 2001 *Int. J. Inorg. Mater.* **3** 1261–1266

[270] Kilner J A 1981 *Phil. Mag.* A **43** 1473–82

[271] Cherry M, Islam M S and Catlow C R A 1995 *J. Solid State Chem.* **118** 125–32

[272] Islam M S 2002 *Solid State Ion.* **154–155** 75–85
[273] Ishihara T, Matsuda H and Takita Y 1994 *J. Am. Chem. Soc.* **116** 3801–3
[274] Iwahara H, Yajima T and Ushida H 1994 *Solid State Ion.* **70–71** 267–71
[275] Iwahara H 1992 *Solid State Ion.* **52** 99–104
[276] Bonanos N 2001 *Solid State Ion.* **145** 265–74
[277] Nowick A S and Du Y 1995 *Solid State Ion.* **77** 137–46
[278] Iwahara H 1996 *Solid State Ion.* **86–88** 9–15
[279] Kreuer K D 1996 *Chem. Mater.* **8** 610–41
[280] Marti W, Fischer P, Altorfer F, Scheel H J and Tadin M 1994 *J. Phys.: Condens. Matter* **6** 127–35
[281] Sanjuán M L, Orera V M, Merino R I and Blasco J 1998 *J. Phys.: Condens. Matter* **10** 11687–702
[282] Slater P R, Irvine J T S, Ishihara T and Takita Y 1998 *J. Solid State Chem.* **139** 135–43
[283] Howard C J and Kennedy B J 1999 *J. Phys.: Condens. Matter* **11** 3229–36
[284] Lerch M, Boysen H and Hansen T 2001 *J. Phys. Chem. Solids* **62** 445–55
[285] Boysen H, Lerch M, Gilles R, Krimmer B and Többens D M 2002 *Appl. Phys.* A **74** (Suppl.) S966–8
[286] Knight K S 1994 *Solid State Ion.* **74** 109–17
[287] Genet F, Loridant S, Ritter C and Lucazeau G 1999 *J. Phys. Chem. Solids* **60** 2009–21
[288] Knight K S 2001 *Solid State Ion.* **145** 273–94
[289] Bonanos N, Ellis B, Knight K S and Mahmood M N 1989 *Solid State Ion.* **35** 179–88
[290] Knight K S, Soar M and Bonanos N 1992 *J. Mater. Chem.* **2** 709–12
[291] Scherban T, Villeneuve R, Abello L and Lucazeau G 1993 *J. Raman Spectrosc.* **24** 805–14
[292] Knight K S and Bonanos N 1995 *Solid State Ion.* **77** 189–94
[293] Huang K, Tichy R S and Goodenough J B 1998 *J. Am. Ceram. Soc.* **81** 2565–75
[294] Huang K, Tichy R S and Goodenough J B 1998 *J. Am. Ceram. Soc.* **81** 2576–80
[295] Huang K, Tichy R S and Goodenough J B 1998 *J. Am. Ceram. Soc.* **81** 2581–5
[296] Lybye D, Poulsen F W and Mogensen M 2000 *Solid State Ion.* **128** 91–103
[297] Khan M S, Islam M S and Bates D R 1998 *J. Phys. Chem.* B **102** 3099–104
[298] de Souza R A and Maier J 2003 *Phys. Chem. Chem. Phys.* **5** 740–8
[299] Goodenough J B 1997 *Solid State Ion.* **94** 17–25
[300] Koruda K, Hashimoto I, Adachi K, Akikusa J, Tamou Y, Komada N, Ishihara T and Takita Y 2000 *Solid State Ion.* **132** 199–208
[301] Anderson M T, Vaughey J T and Poeppelmeier K R 1993 *Chem. Mater.* **5** 151–65
[302] Greaves C, Jacobson A J, Tofield B C and Fender B E F 1975 *Acta Crystallogr.* B **31** 641–6
[303] Goodenough J B, Ruiz-Diaz J E and Zhen Y S 1990 *Solid State Ion.* **44** 21–31
[304] Berastegui P, Hull S, García-García F J and Eriksson S-G 2002 *J. Solid State Chem.* **164** 119–30
[305] Gregory D H and Weller M T 1993 *J. Solid State Chem.* **107** 134–48
[306] Adler S B, Reimer J A, Baltisberger J and Werner U 1994 *J. Am. Ceram. Soc.* **116** 675–81
[307] Speakman S A, Richardson J W, Mitchell B J and Misture S T 2002 *Solid State Ion.* **149** 247–59
[308] Hashimoto T, Ueda Y, Yoshinaga M, Komazaki K, Asaoka K and Wang S R 2002 *J. Electrochem. Soc.* **149** A1381–4
[309] Istomin S Y, Koutcenko V A, Antipov E V, Svensson G and Attfield J P 2002 *J. Mater. Chem.* **12** 2352–5
[310] Adler S, Russek S, Reimer J, Fendorf M, Stacy A, Huang Q, Santoro A, Lynn J, Baltisberger J and Werner U 1994 *Solid State Ion.* **68** 193–211
[311] Graia T, Conflant P, Boivin J C and Thomas D 1986 *Solid State Ion.* **18–19** 751–5
[312] Graia T, Conflant P, Nowogrocki G, Boivin J C and Thomas D 1986 *J. Solid State Chem.* **63** 160–5
[313] Michel C, Pelloquin D, Hervieu M, Raveau B, Abbattista F and Vallino M 1994 *J. Solid State Chem.* **109** 122–6
[314] Esmaeilzadeh S, Berastegui P, Grins J and Rundlof H 2000 *J. Solid State Chem.* **152** 435–40
[315] Nikolaichik V I, Amelinckx S, Klinkova L A, Barkovskii N V, Lebedev O I and van Tendeloo G 2002 *J. Solid State Chem.* **163** 44–64
[316] Ruddlesden S N and Popper P 1957 *Acta Crystallogr.* **10** 538–9
[317] Ruddlesden S N and Popper P 1958 *Acta Crystallogr.* **11** 54–5
[318] Aurivillius B 1949 *Ark. Kemi.* **1** 463–80
[319] Aurivillius B 1949 *Ark. Kemi.* **1** 499–512
[320] Aurivillius B 1950 *Ark. Kemi.* **2** 519–27
[321] Pirovano C, Islam M S, Vannier R N, Nowogrocki G and Mairesse G 2001 *Solid State Ion.* **140** 115–23
[322] Knight K S 1992 *Miner. Mag.* **56** 399–409
[323] Abraham F, Debreuille-Gresse M F, Mairesse G and Nowogrocki G 1988 *Solid State Ion.* **28–30** 529–32
[324] Vannier R N, Pernot B, Anne M, Isnard O, Nowogrocki G and Mairesse G 2003 *Solid State Ion.* **157** 147–53

[325] Vannier R N, Mairesse G, Abraham F, Nowogrocki G, Pernot E, Anne M, Bacmann M, Strobel P and Fouletier J 1995 *Solid State Ion.* **78** 183–9

[326] Joubert O, Jouanneaux A and Ganne M 1994 *Mater. Res. Bull.* **29** 175–84

[327] Touboul M, Lokaj J, Tessier L, Kettman V and Vrabel V 1992 *Acta Crystallogr.* C **48** 1176–9

[328] Sooryanarayana K, Guru T N Row and Varma K B R 1997 *Mater. Res. Bull.* **32** 1651–6

[329] Abraham F, Boivin J C, Mairesse G and Nowogrocki G 1990 *Solid State Ion.* **40–41** 934–7

[330] Kendall K R, Navas C, Thomas J K and zur Loye H-C 1996 *Chem. Mater.* **8** 642–9

[331] Abrahams I, Krok F and Nelstrop J A G 1996 *Solid State Ion.* **90** 57–65

[332] Abrahams I, Nelstrop J A G, Krok F and Bogusz W 1998 *Solid State Ion.* **110** 95–101

[333] Abrahams I and Krok F 2002 *J. Mater. Chem.* **12** 3351–62

[334] Kim N and Grey C P 2002 *Science* **297** 1317–20

[335] Pernot E, Anne M, Bacmann M, Strobel P, Fouletier J, Vannier R N, Mairesse G, Abraham F and Nowogrocki G 1994 *Solid State Ion.* **70–71** 259–63

[336] Krok F, Abrahams I, Bangobango D G, Bogusz W and Nelstrop J A G 1996 *Solid State Ion.* **86–88** 261–6

[337] Lazure S, Vernochet C, Vannier R N, Nowogrocki G and Mairesse G 1996 *Solid State Ion.* **90** 117–23

[338] Watanabe A and Das K 2002 *J. Solid State Chem.* **163** 224–30

[339] Huvé M, Vannier R-N, Nowogrocki G, Mairesse G and van Tendeloo G 1996 *J. Mater. Chem.* **6** 1339–45

[340] O'Keeffe M and Hyde B G 1977 *Acta Crystallogr.* B **33** 3802–13

[341] Thoma R E and Brunton G D 1966 *Inorg. Chem.* **5** 1937–9

[342] Sobolev B P, Garashina L S, Federov P P, Tkachenko N L and Seiranyan K B 1974 *Sov. Phys.—Crystallogr.* **18** 473–6

[343] Lyon W G, Osborne D W, Flotow H E, Grandjean F, Hubbard W N and Johnson G K 1978 *J. Chem. Phys.* **69** 167–73

[344] Cheetham A K and Norman N 1974 *Acta Chim. Scand.* A **28** 55–60

[345] Rotereau K, Daniel P, Desert A and Gesland J Y 1998 *J. Phys.: Condens. Matter* **10** 1431–46

[346] Sobolev B P and Federov P P 1973 *Sov. Phys.—Crystallogr.* **18** 392

[347] O'Keeffe M 1973 *Science* **180** 1276–7

[348] Trnovcová V, Garashina L S, Škubla A, Federov P P, Cicka A, Krivandina E A and Sobolev B P 2003 *Solid State Ion.* **157** 195–201

[349] Schlyter K 1952 *Ark. Kemi.* **5** 73–82

[350] Goldman M and Shen L 1966 *Phys. Rev.* **144** 321–31

[351] Cheetham A K, Fender B E F, Fuess H and Wright A F 1976 *Acta Crystallogr.* B **32** 94–7

[352] Brach I and Schulz H 1985 *Solid State Ion.* **15** 135–8

[353] Belzner A, Schulz H and Heger G 1994 *Z. Kristallogr.* **209** 239–48

[354] Muller-Bunz H and Schleid T 1999 *Z. Anorg. Allg. Chem.* **625** 1377–83

[355] Jordan W M and Catlow C R A 1987 *Cryst. Latt. Def. Amorph. Mater.* **15** 81–7

[356] Rhandour A, Reau J-M, Matar S F, Tian S B and Hagenmuller P 1985 *Mater. Res. Bull.* **20** 1309–27

[357] Privalov A F, Vieth H-M and Murin I V 1989 *J. Phys. Chem. Solids* **50** 395–8

[358] Wang F and Grey C P 1997 *Chem. Mater.* **9** 1068–70

[359] Schoonman J, Oversluizen G and Wapenaar K E D 1980 *Solid State Ion.* **1** 211–21

[360] Abe M and Uchino K 1974 *Mater. Res. Bull.* **9** 147–56

[361] Nadiri A, le Flem G and Dalmas C 1988 *J. Solid State Chem.* **73** 338–47

[362] Howard C J, Luca V and Knight K S 2002 *J. Phys.: Condens. Matter* **14** 377–87

[363] Inaguma Y, Liquan C, Itoh M, Makamura T, Uchida T, Ikuta M and Wakihara M 1993 *Solid State Commun.* **86** 689–93

[364] Kawai H and Kuwano J 1994 *J. Electrochem. Soc.* **141** L78–9

[365] Robertson A D, Garcia-Martin S, Coats A and West A R 1995 *J. Mater. Chem.* **5** 1405–12

[366] Bohnke O, Bohnke C and Fourquet J L 1996 *Solid State Ion.* **91** 21–31

[367] Harada Y, Ishigaki T, Kawai H and Kuwano J 1998 *Solid State Ion.* **108** 407–13

[368] Robertson A D, West A R and Richie A G 1997 *Solid State Ion.* **104** 1–11

[369] Itoh M, Inaguma Y, Jung W-H, Chen L and Nakamura T 1994 *Solid State Ion.* **70–71** 203–7

[370] Fourquet J L, Duroy H and Crosnier-Lopez M P 1996 *J. Solid State Chem.* **127** 283–94

[371] Harada Y, Hirakoso Y, Kawai H and Kuwano J 1999 *Solid State Ion.* **121** 245–51

[372] Bohnke O, Duroy H, Fourquet J-L, Ronchetti S and Mazza D 2002 *Solid State Ion.* **149** 217–26

[373] Paris M A, Sanz J, León C, Santamaria J, Ibarra J and Várez A 2000 *Chem. Mater.* **12** 1694–701

[374] Sanz J, Alonso J A, Varez A and Fernández-Diaz M T 2002 *J. Chem. Soc.: Dalton Trans.* 1406–8

[375] Ruiz A I, Lopez M L, Veiga M L and Pico C 1999 *J. Solid State Chem.* **148** 329–32

[376] Emery J, Bohnké O, Fourquet J L, Buzaré J Y, Florian P and Massiot D 2002 *J. Phys.: Condens. Matter* **14** 523–39

[377] Brown I D 2002 *The Chemical Bond in Inorganic Chemistry. The Bond Valence Method* (Oxford: Oxford University Press)

[378] Mazza D, Ronchetti S, Bohnké O, Duroy H and Fourquet J L 2002 *Solid State Ion.* **149** 81–8

[379] Inaguma Y, Yu J, Katsumata T and Itoh M 1997 *J. Ceram. Soc. Japan* **105** 548–50

[380] Belous A G 1996 *Solid State Ion.* **90** 193–6

[381] Garciá-Martín S, Rojo J M, Tsukamoto H, Morán E and Alario-Franco M A 1999 *Solid State Ion.* **116** 11–18

[382] Torii Y, Sekiya T and Yamamoto T 1982 *Mater. Res. Bull.* **17** 727–32

[383] Latie L, Villeneuve G, Conte D and le Flem G 1984 *J. Solid State Chem.* **51** 293–9

[384] Kawakami Y, Ikuta H and Wakihara M 1998 *J. Solid State Electrochem.* **2** 206–10

[385] Garciá-Martín S and Alario-Franco M Á 1999 *J. Solid State Chem.* **148** 93–9

[386] Salje E K H, Rehmann S, Pobell F, Morris D, Knight K S, Herrmannsdörfer T and Dove M T 1997 *J. Phys.: Condens. Matter* **9** 6563–77

[387] Locherer K R, Swainson I P and Salje E K H 1999 *J. Phys.: Condens. Matter* **11** 4143–56

[388] Locherer K R, Swainson I P and Salje E K H 1999 *J. Phys.: Condens. Matter* **11** 6737–56

[389] Vogt T, Woodward P M and Hunter B A 1999 *J. Solid State Chem.* **144** 209–15

[390] Granqvist C G 1999 *Electrochem. Acta* **44** 3005–15

[391] Zhong Q, Dahn J R and Colbow K 1992 *Phys. Rev.* B **46** 2554–60

[392] Wiseman P J and Dickens P G 1976 *J. Solid State Chem.* **17** 91–100

[393] Flerov I N, Gorev M V, Aleksandrov K S, Tressaud A, Grannec J and Couzi M 1998 *Mater. Sci. Eng.* R **24** 81–151

[394] Bock O and Müller U 2002 *Acta Crystallogr.* B **58** 594–606

[395] Flerov I N, Gorev M V, Grannec J and Tressaud A 2002 *J. Fluorine Chem.* **116** 9–14

[396] Yang H, Ghose S and Hatch D M 1993 *Phys. Chem. Miner.* **19** 528–44

[397] Steward E G and Rooksby H P 1953 *Acta Crystallogr.* **6** 49–52

[398] Holm J L 1965 *Acta Chim. Scand.* **19** 261–3

[399] Landon G J and Ubbelohde A R 1957 *Proc. R. Soc. Lond.* A **240** 160–72

[400] Spearing D R, Stebbins J F and Farnan I 1994 *Phys. Chem. Miner.* **21** 373–86

[401] Castiglione M J 2000 *PhD Thesis* University of Oxford

[402] Jacoboni C, Leble A and Rousseau J J 1981 *J. Solid State Chem.* **36** 297–304

[403] van Hove 1954 L *Phys. Rev.* **95** 249–62

[404] Chudley C T and Elliott R J 1961 *Proc. R. Soc.* **77** 353–61

[405] Wolf D 1977 *Solid State Commun.* **23** 853–8

[406] Dickens M H, Hayes W, Schnabel P, Hutchings M T, Lechner R E and Renker B 1983 *J. Phys. C: Solid State Phys.* **16** L1–6

[407] Gillan M J 1986 *J. Phys. C: Solid State Phys.* **19** 3391–411

[408] Gillan M J 1986 *J. Phys. C: Solid State Phys.* **19** 3517–33

[409] Lindan P J D and Gillan M J 1993 *J. Phys.: Condens. Matter* **5** 1019–30

[410] Gillan M J and Dixon M 1980 *J. Phys. C: Solid State Phys.* **13** 1901–17

[411] Dixon M and Gillan M J 1980 *J. Phys. C: Solid State Phys.* **13** 1919–29

[412] Gillan M J and Dixon M 1980 *J. Phys. C: Solid State Phys.* **13** L835–9

[413] Gillan M J 1985 *Physica* B **131** 157–74

[414] Catlow C R A and Mackrodt W C (ed) 1982 *Computer Simulation of Solids* (Berlin: Springer)

[415] Madden P A and Wilson M 1996 *Chem. Soc. Rev.* **25** 339–50

[416] Wilson N T, Wilson M, Madden P A and Pyper N C 1996 *J. Chem. Phys.* **105** 11209–19

[417] Réau J-M, Lucat C, Portier J, Hagenmuller P, Cot L and Vilminot S 1978 *Mater. Res. Bull.* **13** 877–82

[418] Wakagi A, Kuwano J, Kato M and Hanamoto H 1994 *Solid State Ion.* **70** 601–5

[419] Wakagi A and Kuwano J 1994 *J. Mater. Chem.* **4** 973–5

[420] Pérez G, Vilminot S, Granier W and Cot L 1980 *Mater. Res. Bull.* **15** 587–93

[421] Collin A, Dénès G, le Roux D, Madamba M C, Parris J M and Salaün A 1999 *Int. J. Inorg. Mater.* **1** 289–301

[422] Vilminot S, Perez G, Granier W and Cot L 1981 *Solid State Ion.* **2** 87–90

[423] Vilminot S, Perez G, Granier W and Cot L 1981 *Solid State Ion.* **2** 91–4

[424] Chernov S V, Moskvin A L and Murin I V 1991 *Solid State Ion.* **47** 71–3

[425] Denes G, Yu Y H, Tyliszczak T and Hitchcock A P 1991 *J. Solid State Chem.* **91** 1–15

[426] Denes G, Yu Y H, Tyliszczak T and Hitchcock A P 1993 *J. Solid State Chem.* **104** 239–52

[427] Kanno R, Ohno K, Izumi H, Kawamoto Y, Kamiyama T, Asano H and Izumi F 1994 *Solid State Ion.* **70–71** 253–8

[428] Ito Y, Mukoyama T, Funatomi H, Yoshikado S and Tanaka T 1994 *Solid State Ion.* **67** 301–5

[429] Ito Y, Mukoyama T and Yoshikado S 1995 *Solid State Ion.* **80** 317–20

[430] Castiglione M, Madden P A, Berastegui P and Hull S in preparation

[431] Durand-Le Floch M, Pannetier J and Denes G 1986 *Phys. Rev.* B **33** 632–4

[432] Chaudhuri S, Wang F and Grey C P 2002 *J. Am. Chem. Soc.* **124** 11746–57

[433] Lacorre P, Goutenoire F, Bohnke O, Retoux R and Laligant Y 2000 *Nature* **404** 856–8

[434] Lacorre P 2000 *Solid State Sci.* **2** 755–8

[435] Lucat C, Sorbe P, Portier J, Réau J-M and Hagenmuller P 1977 *Mater. Res. Bull.* **12** 145–50

[436] Matar S, Réau J-M, Lucat C, Grannec J and Hagenmuller P 1980 *Mater. Res. Bull.* **15** 1295–301

[437] Matar S, Reau J-M, Grannec J and Rabardel L 1983 *J. Solid State Chem.* **50** 1–6

[438] Matar S F, Reau J-M, Rabardel L, Grannec J and Hagenmuller P 1983 *Mater. Res. Bull.* **18** 1485–92

[439] Soubeyroux J L, Reau J-M, Matar S, Villeneuve G and Hagenmuller P 1982 *Solid State Ion.* **6** 103–111

[440] Laborde P, Villeneuve G, Reau J-M and Hagenmuller P 1986 *Z. Anorg. Allg. Chem.* **537** 40–52

[441] Cox P A, Catlow C R A and Chadwick A V 1994 *J. Mater. Sci.* **29** 2725–33

[442] Matar S F, Reau J-M, Hagenmuller P and Catlow C R A 1984 *J. Solid State Chem.* **52** 114–23

[443] Matar S F, Reau J-M, Laborde P and Rhandour A 1988 *J. Phys. Chem. Solids* **49** 285–8

[444] Pierce J W and Hong H Y-P 1973 *Proc. 10th Rare Earth Research Conf. (Carefree, Arizona)* pp 527–37

[445] Lucat C, Campet G, Claverie J, Portier J, Reau J-M and Hagenmuller P 1976 *Mater. Res. Bull.* **11** 167–72

[446] Lucat C, Portier J, Reau J-M, Hagenmuller P and Soubeyroux J-L 1980 *J. Solid State Chem.* **32** 279–87

[447] Ito Y, Koto K, Yoshikado S and Ohachi T 1986 *Solid State Ion.* **18–19** 1202–7

[448] Reau J-M, el Omari M, Senegas J and Hagenmuller P 1989 *Mater. Res. Bull.* **24** 1441–52

[449] Réau J M, Rederov P P, Rabardel L, Matar S F and Hagenmuller P 1983 *Mater. Res. Bull.* **18** 1235–46

[450] Joshi A V and Liang C C 1977 *J. Electrochem. Soc.* **124** 1253–7

[451] el Omari M, Senegas J and Reau J-M 1997 *Solid State Ion.* **100** 233–40

[452] el Omari M, Senegas J and Reau J-M 1997 *Solid State Ion.* **100** 241–6

[453] Soubeyroux J L, Reau J-M, Matar S, Hagenmuller P and Lucat C 1981 *Solid State Ion.* **2** 215–29

[454] Reau J-M, Jun X Y, Senegas J and Hagenmuller P 1995 *Solid State Ion.* **78** 315–31

[455] Laval J P, Depierrefixe C, Frit B and Roult G 1984 *J. Solid State Chem.* **54** 260–76

[456] Senegas J, Laval J P and Frit B 1986 *J. Fluorine Chem.* **32** 197–211

[457] Reau J-M, Senegas J, el Omari M and Soubeyroux J L 1990 *J. Fluorine Chem.* **49** 87–98

[458] Rhandour A, Reau J-M and Hagenmuller P 1986 *J. Solid State Chem.* **61** 197–202

[459] Ivanov-Shits A K, Sorokin N I, Federov P P and Sobolev B P 1990 *Solid State Ion.* **37** 125–37

[460] Reau J-M and Hagenmuller P 1995 *Bull. Electrochem.* **11** 34–46

[461] Corish J, Catlow C R A, Jacobs P W M and Ong S H 1982 *Phys. Rev.* B **25** 6425–38

[462] Jiang H, Costales A, Blanco M A, Gu M, Pandey R and Gale J D 2000 *Phys. Rev.* B **62** 803–9

[463] Hull S and Wilson C C 1992 *J. Solid State Chem.* **100** 101–14

[464] Cheetham A K, Fender B E F, Steele D, Taylor R I and Willis B T M 1970 *Solid State Commun.* **8** 171–3

[465] Cheetham A K, Fender B E F and Cooper M J 1971 *J. Phys. C: Solid State Phys.* **4** 3107–21

[466] Steele D, Childs P E and Fender B E F 1972 *J. Phys. C: Solid State Phys.* **5** 2677–88

[467] Laval J P and Frit B 1983 *J. Solid State Chem.* **49** 237–46

[468] Otroshchenko L P, Aleksandrov V B, Bydanov N N, Simonov V I and Sobolev B P 1988 *Sov. Phys.—Crystallogr.* **33** 449–51

[469] Muradyan L A, Maksimov B A, Aleksandrov V B, Otroshchenko L P, Bydanov N N, Sirota M I and Simonov V I 1986 *Sov. Phys.—Crystallogr.* **31** 390–2

[470] Bendall P J, Catlow C R A and Fender B E F 1984 *J. Phys. C: Solid State Phys.* **17** 797–814

[471] Laval J P, Mikou A, Frit B and Roult G 1988 *Solid State Ion.* **28–30** 1300–4

[472] Goff J P, Hutchings M T, Hull S, Fak B and Hayes W 1992 *J. Phys.: Condens. Matter* **4** 1433–46

[473] Catlow C R A, Chadwick A V, Greaves G N and Moroney L M 1984 *Nature* **312** 601–4

[474] Catlow C R A, Chadwick A V, Corish J, Moroney L M and O'Reilly A N 1989 *Phys. Rev.* B **39** 1897–907

[475] Laval J P, Abaouz A, Frit B and le Bail A 1990 *J. Solid State Chem.* **85** 133–43

[476] Bendall P J, Catlow C R A, Corish J and Jacobs P W M 1984 *J. Solid State Chem.* **51** 159–69

[477] Wang F and Grey C P 1998 *Chem. Mater.* **10** 3081–91

[478] Bevan D J M, Greis O and Strähle J 1980 *Acta Crystallogr.* A **36** 889–90

[479] Bevan D J M and Lawton S E 1986 *Acta Crystallogr.* B **42** 55–8

[480] Golubev A M and Simonov V I 1986 *Sov. Phys.—Crystallogr.* **31** 281–7

[481] Bevan D J M, Strähle J and Greis O 1982 *J. Solid State Chem.* **44** 75–81

[482] Gettmann W and Greis O 1978 *J. Solid State Chem.* **26** 255–63

[483] Federov P P, Turkina T M, Sobolev B P, Mariani E and Svantner M 1982 *Solid State Ion.* **6** 331–5

[484] Catlow C R A, Comins J D, Germano F A, Harley R T, Hayes W and Owen I B 1981 *J. Phys. C: Solid State Phys.* **14** 329–35
[485] Archer J A, Chadwick A V, Jack I R and Zeqiri B 1983 *Solid State Ion.* **9–10** 505–10
[486] Hofmann M, Hull S, McIntyre G J and Wilson C C 1997 *J. Phys.: Condens. Matter* **9** 845–57
[487] Scott H G 1975 *J. Mater. Sci.* **10** 1527–35
[488] Stubican V S, Hink R C and Ray S P 1978 *J. Am. Ceram. Soc.* **61** 17–21
[489] Teufer G 1962 *Acta Crystallogr.* **15** 1187
[490] Howard C J, Hill R J and Reichert B E 1988 *Acta Crystallogr.* B **44** 116–20
[491] Etsell T H, Spyridon N and Flengas S N 1970 *Chem. Rev.* **70** 339–76
[492] Birkby I and Stevens R 1996 *Key Eng. Mater.* **122–124** 527–52
[493] Solier J D, Cachadiña I and Dominguez-Rodriguez A 1993 *Phys. Rev.* B **48** 3704–12
[494] León C, Lucía M L and Santamaría J 1997 *Phys. Rev.* B **55** 882–7
[495] Perry C H and Feinberg A 1980 *Solid State Commun.* **36** 519–22
[496] Subbarao E C and Ramakrishnan T V 1979 *Fast Ion Transport in Solids* ed P Vashishta *et al* (New York: Elsevier/North-Holland) 653–6
[497] Nakamura A and Wagner J B Jr 1986 *J. Electrochem. Soc.* **133** 1542–8
[498] Arachi Y, Sakai H, Yamamoto O, Takeda Y and Imanishai N 1999 *Solid State Ion.* **121** 133–9
[499] Khanna R, Welberry T R and Withers R L 1993 *J. Phys.: Condens. Matter* **5** 4251–62
[500] Meyer M and Nicoloso N 1997 *Ber. Bunsenges. Phys. Chem.* **101** 1393–8
[501] Meyer M, Nicoloso N and Jaenisch V 1997 *Phys. Rev.* B **56** 5961–6
[502] Shimojo F, Okabe T, Tachibana F, Kobayashi M and Okazaki H 1992 *J. Phys. Soc. Japan* **61** 2848–57
[503] Shimojo F and Okazaki H 1992 *J. Phys. Soc. Japan* **61** 4106–18
[504] Brinkman H W, Briels W J and Verweij H 1995 *Chem. Phys. Lett.* **247** 386–90
[505] Li X and Hafskjold B 1995 *J. Phys.: Condens. Matter* **7** 1255–71
[506] Sawaguchi N and Ogawa H 2000 *Solid State Ion.* **128** 183–9
[507] Catlow C R A 1984 *Solid State Ion.* **12** 67–73
[508] Mackrodt W C and Woodrow P M 1986 *J. Am. Ceram. Soc.* **69** 277–80
[509] Stefanovich E V, Shluger A L and Catlow C R A 1994 *Phys. Rev.* B **49** 11560–71
[510] Khan M S, Islam M S and Bates D R 1998 *J. Mater. Chem.* **8** 2299–307
[511] Stapper G, Bernasconi M, Nicoloso N and Parrinello M 1999 *Phys. Rev.* B **59** 797–810
[512] Zacate M O, Minervini L, Bradfield D J, Grimes R W and Sickafus K E 2000 *Solid State Ion.* **128** 243–54
[513] Bogicevic A, Wolverton C, Crosbie G M and Stechel E B 2001 *Phys. Rev.* B **64** 014106
[514] Hohnke D K 1981 *Solid State Ion.* **5** 531–4
[515] Schoenlein L H, Hobbs L W and Heuer A H 1980 *J. Appl. Cryst.* **13** 375–9
[516] Suzuki S, Tanaka M and Ishigame M 1985 *Japan. J. Appl. Phys.* **24** 401–10
[517] Suzuki S, Tanaka M and Ishigame M 1987 *J. Phys. C: Solid State Phys.* **20** 2963–72
[518] Suzuki S, Tanaka M and Ishigame M 1987 *Japan. J. Appl. Phys.* **26** 1983–7
[519] McClellan K, Xiao J S-Q, Lagerlof K P D and Heuer A H 1994 *Phil. Mag.* A **70** 185–200
[520] Dai Z R, Wang Z L, Chen Y R, Wu H Z and Liu W X 1996 *Phil. Mag.* A **73** 415–30
[521] Dai Z R, Wang Z L and Liu W X 1996 *Phil. Mag.* A **73** 1685–98
[522] Gallardo-López A, Martínez-Fernández J, Domínguez-Rodríguez A and Ernst F 2001 *Phil. Mag.* A **81** 1675–89
[523] Morinaga M, Cohen J B and Faber J Jr 1979 *Acta Crystallogr.* A **35** 789–95
[524] Morinaga M, Cohen J B and Faber J Jr 1980 *Acta Crystallogr.* A **36** 520–30
[525] Welberry T R, Withers R L, Thompson J G and Butler B D 1992 *J. Solid State Chem.* **100** 71–89
[526] Welberry T R, Butler B D, Thompson J G and Withers R L 1993 *J. Solid State Chem.* **106** 461–75
[527] Welberry T R, Withers R L and Mayo S C 1995 *J. Solid State Chem.* **115** 43–54
[528] Ishizawa N, Matsushima Y, Hayashi M and Ueki M 1999 *Acta Crystallogr.* **B55** 726–35
[529] Steele D and Fender B E F 1974 *J. Phys. C: Solid State Phys.* **7** 1–11
[530] Faber J Jr, Mueller M H and Cooper B R 1978 *Phys. Rev.* B **17** 4884–8
[531] Horiuchi H, Schultz A J, Leung P C W and Williams J M 1984 *Acta Crystallogr.* B **40** 367–72
[532] Hull S, Farley T W D, Hackett M A, Hayes W, Osborn R, Andersen N H, Clausen K, Hutchings M T and Stirling W G 1988 *Solid State Ion.* **28–30** 488–92
[533] Argyriou D N 1994 *J. Appl. Cryst.* **27** 155–8
[534] Kahlert H, Frey F, Boysen H and Lassak K 1995 *J. Appl. Crystallogr.* **28** 812–19
[535] Argyriou D M, Elcombe M M and Larson A C 1996 *J. Phys. Chem. Solids* **57** 183–93
[536] Goff J P, Hayes W, Hull S, Hutchings M T and Clausen K N 1999 *Phys. Rev.* B **59** 14202–19
[537] Suemoto T and Ishigame M 1986 *Solid State Ion.* **21** 225–9
[538] Scott H G 1977 *Acta Crystallogr.* B **33** 281–2

[539] Ray S P, Stubican V S and Cox D E 1980 *Mater. Res. Bull.* **15** 1419–23

[540] Catlow C R A, Chadwick A V, Greaves G N and Moroney L M 1986 *J. Am. Ceram. Soc.* **69** 272–7

[541] Li P, Chen I-W and Penner-Hahn J E 1993 *Phys. Rev.* B **48** 10074–81

[542] Tuilier M H, Dexpert-Ghys J, Dexpert H and Lagarde P 1987 *J. Solid State Chem.* **69** 153–61

[543] Rossell H J 1976 *J. Solid State Chem.* **19** 103–11

[544] Subramanian M A, Aravamudan G and Subba Rao G V 1983 *Prog. Solid State Chem.* **15** 55–143

[545] Withers R L, Thompson J G and Barlow P J 1991 *J. Solid State Chem.* **94** 89–105

[546] Chakoumakos B 1984 *J. Solid State Chem.* **53** 120–9

[547] Michel D, Perez y Jorba M and Collongues R 1974 *Mater. Res. Bull.* **9** 1457–68

[548] Yamamura H, Nishino H, Kakinuma K and Nomura K 2003 *Solid State Ion.* **158** 359–65

[549] van Dijk M P, de Vries K J and Burggraaf A J 1983 *Solid State Ion.* **9–10** 913–20

[550] Moriga T, Yoshiasa A, Kanamaru F, Koto K, Yoshimura M and Somiya S 1989 *Solid State Ion.* **31** 319–28

[551] van Dijk M P, Burggraaf A J, Cormack A N and Catlow C R A 1985 *Solid State Ion.* **17** 159–67

[552] Wilde P J and Catlow C R A 1998 *Solid State Ion.* **112** 173–83

[553] Wilde P J and Catlow C R A 1998 *Solid State Ion.* **112** 185–95

[554] Pirzada M, Grimes R W, Minervini L, Maguire J F and Sickafus K E 2001 *Solid State Ion.* **140** 201–8

[555] Minervini L, Grimes R W and Sickafus K E 2000 *J. Am. Ceram. Soc.* **83** 1873–8

[556] Stanek C R, Minervini L and Grimes R W 2002 *J. Am. Ceram. Soc.* **85** 2792–8

[557] Pirzada M, Grimes R W and Maguire J F 2003 *Solid State Ion.* **161** 81–91

[558] Minervini L, Grimes R W, Tabira Y, Withers R L and Sickafus K E 2002 *Phil. Mag.* A **82** 123–35

[559] Heremans C, Wuensch B J, Stalick J K and Prince E 1995 *J. Solid State Chem.* **117** 108–21

[560] Wuensch B J, Eberman K W, Heremans C, Ku E M, Onnerud P, Yeo E M E, Haile S M, Stalick J K and Jorgensen J D 2000 *Solid State Ion.* **129** 111–33

[561] Glerup M, Nielsen O F and Poulsen F W 2001 *J. Solid State Chem.* **160** 25–32

[562] Thomson J B, Armstrong A R and Bruce P G 1999 *J. Solid State Chem.* **148** 56–62

[563] Norby T 2001 *J. Mater. Chem.* **11** 11–18

[564] Harwig H A and Gerards A G 1978 *J. Solid State Chem.* **26** 265–74

[565] Takahashi T and Iwahara H 1978 *Mater. Res. Bull.* **13** 1447–53

[566] Shuk P, Wienhöfer H-D, Guth U, Göpel W and Greenblatt M 1996 *Solid State Ion.* **89** 179–96

[567] Gattow G and Schroder H 1962 *Z. Anorg. Allg. Chem.* **318** 176–89

[568] Sillen L G 1937 *Ark. Kemi. Mineral. Geol.* A **12** 1–15

[569] Harwig H A 1978 *Z. Anorg. Allg. Chem.* **444** 151–66

[570] Willis B T M 1965 *Acta Crystallogr.* **18** 75–6

[571] Battle P D, Catlow C R A, Drennan J and Murray A D 1983 *J. Phys. C: Solid State Phys.* **16** L561–6

[572] Jacobs P W M and Mac Dónaill D A 1986 *Solid State Ion.* **18–19** 209–13

[573] Jacobs P W M and Mac Dónaill D A 1987 *Solid State Ion.* **23** 279–93

[574] Jacobs P W M and Mac Dónaill D A 1987 *Solid State Ion.* **23** 295–305

[575] Jacobs P W M and Mac Dónaill D A 1987 *Solid State Ion.* **23** 307–18

[576] Medvedeva N I, Zhukov V P, Gubanov V A, Novikov D L and Klein B M 1996 *J. Phys. Chem. Solids* **57** 1243–50

[577] Carlsson J M, Hellsing B, Domingos H S and Bristowe P D 2002 *Phys. Rev.* B **65** 205122

[578] Sammes N M, Tompsett G A, Näfe H and Aldinger F 1999 *J. Eur. Ceram. Soc.* **19** 1801–26

[579] Battle P D, Catlow C R A, Heap J W and Moroney L M 1986 *J. Solid State Chem.* **63** 8–15

[580] Ling C D, Withers R L, Schimd S and Thompson J G 1998 *J. Solid State Chem.* **137** 42–61

[581] Carbajo J J, Yoder G L, Popov S G and Ivanov V K 2001 *J. Nucl. Mater.* **299** 181–98

[582] Ralph J and Hyland G J 1985 *J. Nucl. Mater.* **132** 76–9

[583] Ralph J 1987 *Nucl. Energy* **26** 259–63

[584] Browning P, Hyland G J and Ralph J 1983 *High Temp.—High Press.* **15** 169–78

[585] Hyland G J and Ralph J 1983 *High Temp.—High Press.* **15** 179–90

[586] MacInnes D A 1978 *J. Nucl. Mater.* **78** 225–7

[587] Winter P W and MacInnes D A 1986 *J. Nucl. Mater.* **137** 161–6

[588] Fischer D F, Fink J L and Liebowitz L 1981 *J. Nucl. Mater.* **102** 220–2

[589] Clausen K, Hayes W, Macdonald J E, Osborn R and Hutchings M T 1984 *Phys. Rev. Lett.* **52** 1238–41

[590] Hutchings M T 1987 *J. Chem. Soc.: Faraday Trans.* II **83** 1083–103

[591] Donato A 1998 *Fusion Eng. Des.* **38** 369–92

[592] van der Laan J G, Kawamura H, Roux N and Yamaki D 2000 *J. Nucl. Mater.* **283–287** 99–109

[593] Ohno H, Konishi S, Noda K, Takeshita H, Yoshida H, Watanabe H and Matsuo T 1983 *J. Nucl. Mater.* **118** 242–7

[594] Chadwick A V, Flack F W, Strange J H and Harding J 1988 *Solid State Ion.* **28–30** 185–8

[595] Strange J H, Rageb S M, Chadwick A V, Flack K W and Harding J H 1990 *J. Chem. Soc.: Faraday Trans.* **86** 1239–41

[596] Farley T W D, Hayes W, Hull S, Hutchings M T and Vrtis M 1991 *J. Phys.: Condens. Matter* **3** 4761–81

[597] de Vita A, Manassidis I, Lin J S and Gillan M J 1992 *Europhys. Lett.* **19** 605–10

[598] Fracchia R M, Barrera G D, Allan N L, Barron T H K and Mackrodt W C 1998 *J. Phys. Chem. Solids* **59** 435–45

[599] Farley T W D, Hayes W, Hull S, Hutchings M T, Alba M and Vrtis M 1989 *Physica* B **156** 99–102

[600] Kvist A and Lundén A 1965 *Z. Naturf.* A **20** 235–8

[601] Andersen N H, Bandaranayake P W S K, Careem M A, Dissanayake M A K L, Wijayasekera C N, Kaber R, Lundén A, Mellander B-E, Nilsson L and Thomas J O 1992 *Solid State Ion.* **57** 203–9

[602] Kaber R, Nilsson L, Andersen N H, Lundén A and Thomas J O 1992 *J. Phys.: Condens. Matter* **4** 1925–33

[603] Lundén A 1995 *Z. Naturf.* A **50** 1067–76

[604] Börjesson L and Torell L M 1985 *Phys. Rev.* B **32** 2471–7

[605] Ferrario M, Klein M L and McDonald I R 1995 *Mol. Phys.* **86** 923–38

[606] Impey R W, Klein M L and McDonald I R 1984 *J. Phys. C: Solid State Phys.* **17** 3941–4

[607] Gundusharma U M, MacLean C and Secco E A 1986 *Solid State Commun.* **57** 479–81

[608] Lundén A 1988 *Solid State Commun.* **65** 1237–40

[609] Lundén A 1988 *Solid State Ion.* **28–30** 163–7

[610] Dissanayake M A K L, Careem M A, Bandaranayake P W S K and Wijayasekera C N 1991 *Solid State Ion.* **48** 277–81

[611] Lundén A 1994 *Solid State Ion.* **68** 77–80

[612] Babu C S and Tembe B L 1992 *Chem. Phys. Lett.* **194** 351–4

[613] Secco E A 1993 *Solid State Ion.* **60** 233–5

[614] Secco E A 1992 *J. Solid State Chem.* **96** 366–75

[615] Karlsson L and McGreevy R L 1995 *Solid State Ion.* **76** 301–8

[616] Pimenta M A, Echegut P, Gervais F and Abélard P 1988 *Solid State Ion.* **28–30** 224–7

[617] Wiench D M and Jansen M 1980 *Z. Anorg. Allg. Chem.* **461** 101–8

[618] Wilmer D, Funke K, Witschas M, Banhatti R D, Jansen M, Korus G, Fitter J and Lechner R E 1999 *Physica* B **266** 60–8

[619] Zhu B, Mellander B-E and Chen J 1993 *Mater. Res. Bull.* **28** 321–8

[620] Zetterström P, McGreevy R L, Mellergård A and Eriksen J 2002 *Appl. Phys.* A **74** (Suppl.) S995–7

[621] Wilmer D, Feldmann H, Combet J and Lechner R E 2001 *Physica* B **301** 99–104

[622] Jansen M 1991 *Angew. Chem. Int. Edn Engl.* **30** 1547–58

[623] Lutz H D, Schmidt W and Haeuseler H 1981 *J. Phys. Chem. Solids*, **42** 287–9

[624] Kanno R, Takeda Y and Yamamoto O 1981 *Mater. Res. Bull.* **16** 999–1005

[625] Kanno R, Takeda Y, Mori M and Yamamoto O 1989 *Chem. Lett.* 223–6

[626] Soubeyroux J L, Cros C, Gang W, Kanno R and Pouchard M 1985 *Solid State Ion.* **15** 293–300

[627] Nagel R, Groß T W, Günther H and Lutz H D 2002 *J. Solid State Chem.* **165** 303–11

[628] Kanno R, Takeda Y and Yamamoto O 1988 *Solid State Ion.* **28–30** 1276–81

[629] Steiner H J and Lutz H D 1992 *J. Solid State Chem.* **99** 1–11

[630] Lutz H D, Partik M, Schneider M and Wickel C 1997 *Z. Kristallogr.* **212** 418–22

[631] Aghapoor K, Kuske P, Steiner H-J and Lutz H D 1993 *Mater. Res. Bull.* **28** 347–52

[632] Riedel E, Prick D, Pfitzner A and Lutz H D 1993 *Z. Anorg. Allg. Chem.* **619** 901–4

[633] Kanno R, Takeda Y, Takeda K and Yamamoto O 1984 *J. Electrochem. Soc.* **131** 469–74

[634] Thackeray M M 1995 *J. Electrochem. Soc.* **142** 2558–63

[635] Thackeray M M 1997 *Prog. Solid State Chem.* **25** 1–71

[636] Goodenough J B, Thackeray M M, David W I F and Bruce P G 1984 *Rev. Chim. Minér.* **21** 435–55

[637] Ammundsen B, Rozière J and Islam M S 1997 *J. Phys. Chem.* B **101** 8156–63

[638] Verhoeven V W J, de Schepper I M, Nachtegaal G, Kentgens A P M, Kelder E M, Shoonman J and Mulder F M 2001 *Phys. Rev. Lett.* **86** 4314–7

[639] David W I F, Thackeray M M, de Picciotto L A and Goodenough J B 1987 *J. Solid State Chem.* **67** 316–23

[640] Fong C, Kennedy B J and Elcombe M M 1994 *Z. Kristallogr.* **209** 941–5

[641] David W I F, Goodenough J B, Thackeray M M and Thomas M G S R 1983 *Rev. Chim. Minér.* **20** 636–42

[642] Thackeray M M 1999 *J. Am. Ceram. Soc.* **82** 3347–54

[643] Yamada A and Tanaka M 1995 *Mater. Res. Bull.* **30** 715–21

[644] Yamada A 1996 *J. Solid State Chem.* **122** 160–5

[645] Rodríguez-Carvajal J, Rousse G, Masquelier C and Hervieu M 1998 *Phys. Rev. Lett.* **81** 4660–3

[646] Gummow R J, de Kock A and Thackeray M M 1994 *Solid State Ion.* **69** 59–67

[647] Ammundsen B, Burns G R, Islam M S, Kanoh H and Rozière J 1999 *J. Phys. Chem.* B **103** 5175–80

[648] Björk H, Gustafsson T, Thomas J O, Lidin S and Petricek V 2003 *J. Mater. Chem.* **13** 585–89

[649] Dupont L, Hervieu M, Rousse G, Masquelier C, Palacín M R, Chabre Y and Tarascon J M 2000 *J. Solid State Chem.* **155** 394–408

[650] Lee Y J, Wang F, Mukerjee S, McBreen J and Grey C P 2000 *J. Electrochem. Soc.* **147** 803–12

[651] Sun X, Yang X Q, Balasubramanian M, McBreen J, Xia Y and Sakai T 2002 *J. Electrochem. Soc.* **149** A842–8

[652] Berg H, Rundlöv H and Thomas J O 2001 *Solid State Ion.* **144** 65–9

[653] West A R 1975 *Z. Kristallogr.* **141** 422–36

[654] O'Keeffe M and Hyde B G 1978 *Acta Crystallogr.* B **34** 3519–28

[655] Abrahams I, Bruce P G, West A R and David W I F 1988 *J. Solid State Chem.* **75** 390–6

[656] Abrahams I, Bruce P G, David W I F and West A R 1989 *Acta Crystallogr.* B **45** 457–62

[657] Bruce P G, Abrahams I and West A R 1990 *Solid State Ion.* **40–41** 293–9

[658] Abrahams I and Bruce P G 1991 *Phil. Mag.* A **64** 1113–18

[659] Baur W H 1981 *Mater. Res. Bull.* **16** 339–45

[660] West A R and Bruce P G 1982 *Acta Crystallogr.* B **38** 1891–6

[661] West A R 1995 *Solid State Electrochemistry* ed P G Bruce (Cambridge: Cambridge University Press) pp 7–42

[662] Smith R I and West A R 1991 *J. Mater. Chem.* **1** 91–6

[663] Schulz H and Zucker U H 1981 *Solid State Ion.* **5** 41–6

[664] Lechner R E 1993 *Solid State Ion.* **61** 3–11

[665] Comins J D, Ngoepe P E and Catlow C R A 1990 *J. Chem. Soc.: Faraday Trans.* **86** 1183–92

[666] Hayes W 1982 *Topics Appl. Phys.* **51** 93–120

[667] Ishigame M, Shin S and Suemoto T 1991 *Solid State Ion.* **47** 1–34

[668] Brinkmann D 1992 *Prog. NMR Spectrosc.* **24** 527–52

[669] Chadwick A V 1991 *Phil. Mag.* A **64** 983–98

[670] Jiang S P, Love J G and Badwal S P S 1997 *Key Eng. Mater.* **125–126** 81–132

[671] Dalba G, Fornasini P, Gotter R, Grazioli M and Rocca F 1995 *Phil. Mag.* B **71** 751–60

[672] Catlow C R A 1992 *Solid State Ion.* **53–56** 955–63

[673] Catlow C R A, Bell R G and Gale J D 1994 *J. Mater. Chem.* **4** 781–92

[674] Sivia D S and David W I F 2001 *J. Phys. Chem. Solids* **62** 2119–27

[675] Wilson M and Madden P A 1993 *J. Phys.: Condens. Matter* **5** 2687–706

[676] Wilson M, Madden P A and Costa Cabral B J 1996 *J. Phys. Chem.* **100** 1227–37

[677] Radulescu A, Padureanu I, Rapeanu S N, Beldiman A, Ion M, Kozlov Z A and Semenov V A 1999 *Phys. Rev.* B **59** 3270–3

[678] Delaney M J and Ushioda S 1979 Physics of superionic conductors *Topics in Current Physics* vol 15, ed M B Salamon (Berlin: Springer) pp 111–39